High-Speed Measurements of Mixing Due to the Richtmyer-Meshkov Instability in a Twice-Shocked Gas Interface

By

Christopher D. Noble

A Dissertation submitted in partial fulfillment of

the requirements for the degree of

Doctor of Philosophy

(Engineering Mechanics)

at the

UNIVERSITY OF WISCONSIN – MADISON

2022

Date of final oral examination: 08/03/2022

The dissertation is approved by the following members of the Final Oral Committee:

Riccardo Bonazza, Engineering Physics
David Rothamer, Mechanical Engineering
Jennifer Franck, Engineering Physics
Mario Trujillo, Mechanical Engineering
Jaal Ghandhi, Mechanical Engineering
Jason Oakley, Mechanical Engineering

Abstract

The Richtmyer-Meshkov instability (RMI) of a twice-shocked gas interface is studied in the Wisconsin Shock Tube Lab's 9 m tall, vertical, downward-firing shock tube.

Three sets of experiments were conducted, all investigating the same initial condition: a shear layer with broadband diffuse perturbations at an interface between a helium-acetone mixture and argon. The first set of experiments (SS) build off work by previous graduate students in the lab who explored the evolution of the singly-shocked RMI. These first experiments are single-shot simultaneous measurements of velocity and concentration at 4 distinct times after reshock. The second set of experiments (HS) are novel high-speed measurements purely of concentration, implementing the use of a pulse-burst laser system that allowed planar laser induced fluorescence (PLIF) measurements at 20 kHz. The conditions upon reshock, as opposed to singly-shocked, allowed an extended period over which the evolving interface is in the field of view of the high-speed camera, meaning around 90 frames could be captured with each run as opposed to a single measurement for each run as was previously the case. The third set of experiments (HSS) are high-speed simultaneous measurements of velocity and concentration. These combine the experience of performing the single shot experiments with the abilities that the pulse-burst laser system affords, which allows for the use of both 532 nm and 266 nm wavelengths to engage in both PLIF and particle image velocimetry (PIV) measurements at 20 kHz.

In all three studies, the shear layer is accelerated by a shock of nominal strength M=1.8 and then accelerated again once the shock has reflected off the bottom wall of the tube.

Previous experiments have mostly focused on analyzing the evolution of integral measures

of the RM instability as these are the most pertinent to immediate applications of inertial confinement fusion (ICF), supernovae explosion evolution, and scramjet fuel injection. These measures are also the most readily explored with past experimental techniques and the associated limits of time and space resolutions.

Advances in laser and imaging technologies now allow for close-to-full-field time-resolved imaging of velocity and density fields which enable the exploration of the mechanisms behind the growth of these integral measures. Instead of answering "how do these evolve?", one can now begin the long task of answering "why do they evolve as they do?".

Here the combined data of all three experiments will be used to explore those integral measures: the mixing thickness and mixedness; then to explore the transport of energy from scale to scale, focusing on individual terms in the transport equations for the scalar concentration and the streamwise kinetic energy. This scale to scale transport will be explored in three distinct domains: in Fourier space, in scale space via structure functions and using filter-based methods as encouraged by the prominent use of large eddy simulations (LES) to study the RMI.

Acknowledgements

First and foremost I am extremely grateful to my supervisor, Professor Riccardo Bonazza, whose guidance, encouragement and friendship were fundamental to the work in this thesis.

I would like to thank Dr Jason Oakley, especially those first few years, for being an invaluable treasure trove of information and assistance, and for always making time to let me sit down and talk through problems.

I can't thank Professor David Rothamer enough for being a great source of technical expertise, for facilitating the high-speed experiments we performed by allowing the use of his brilliant laser system, the Deathstar, and for putting up with my unique figure style.

Dan Reeses, Alex Ames and Raymond McConnell have been amazing colleagues and friends who made the long hours of data telling me "No!" not just bearable but enjoyable.

Joshua Herzog's input and friendship was vital to the completion of this work. Moving to a new experiment regime brought new challenges that his mastery of was key to navigating. The numerous philosophical discussions were much needed and enjoyed.

I must thank Ben Chapel, Gunnar Eichenlaub, Jimmy Sumpter, Tim Vaughan, Sam Szotkowski, Gunnar Thompson and Mitch Corcoran. Each of you were awesome help and essential to the completion of the experiments discussed here. You are all also great and fun people whom I am honoured to have worked with.

Bob and Joanne Lenburg were the first people I ever met in Madison, you made me feel at home and helped me get settled. Your continued friendship has been a wonderful highlight of my time in Madison.

Mum and Dad, Thank you so much for everything. This would not have been possible without you!

Nicole ♥

This work was supported by US DOE grant DE-NA0003932.

Contents

List of Tables

List of Figures

Nomenclature

Abbreviations

FAV	Fast-acting valve
FFT	Fast Fourier transform
IC	Initial condition time/location
ICF	Inertial confinement fusion
LANL	Los Alamos National Laboratory
LES	Large-eddy simulation
LLNL	Lawrence Livermore National Laboratory
PDF	Probability density function
PIV	Particle image velocimetry
PLIF	Planar laser-induced fluorescence
SS	Single-shot simultaneous experiments
HS	High-speed experiments
HSS	High-speed simultaneous experiments
PS1	First post-shock time/location
PS2	Second post-shock time/location

PS3	Third post-shock time/location
PS4	Fourth post-shock time/location
RS1	First post-reshock time/location
RS2	Second post-reshock time/location
RS3	Third post-reshock time/location
RS4	Fourth post-reshock time/location
RMI	Richtmyer-Meshkov instability
RMS	Root mean square
RTI	Rayleigh-Taylor instability
WiSTL	Wisconsin shock tube laboratory

English Symbols

A	Atwood number across the interface
$\mathcal{D}$	Mass Diffusivity [m^2/s]
D	Time integrated diffusion [-]
E	Power spectra [-]
$\mathcal{F}_{x^+}[\ ]$	Fourier transform in the variable x^+
G	Filter [-]

$\mathcal{G}$	Energy transfer diffusivity gradient term [-]
$\mathcal{H}$	Energy transfer Pressure diffusion term [-]
k	Wavenumber [1/m]
L	Integral scale [m]
m_{ij}	Mixed-moments
M_{ij}	Normalised mixed-moments
M_s	Mach number of incident shock wave
p	Pressure [Pa]
Re	Reynolds number
Re_λ	Taylor Reynolds number
S_f	Fluorescence signal [counts]
S_p	structure function of order p
t_s	Time after shock traverses the interface [s]
T	Temperature [K]
$\mathcal{T}$	Transport term [-]
$\boldsymbol{u}$	Velocity vector [m/s]
$\boldsymbol{u}'$	Velocity-flucuation vector [m/s]
u	x-component of velocity [m/s]

u'	x-component of velocity-flucuation [m/s]
v	y-component of velocity [m/s]
v'	y-component of velocity-flucuation [m/s]
$\boldsymbol{v}_i$	i-component of density weighted velocity [$\mathrm{kg}^{1/2}/\mathrm{m}^{3/2}$ m/s]
V_0	Post-shock 1D interface velocity [m/s]
w	z-component of velocity [m/s]
w'	z-component of velocity-flucuation [m/s]
W	Shock-tube width [m]
$\boldsymbol{x}$	Position vector [m]
x	x-component of position [m]
X	Time integrated dissipation [-]
y	y-component of position [m]
z	z-component of position [m]
Z_p	integrated structure function of order p

Greek Symbols

λ_T	Taylor microscale [m]
Λ	integrated power spectra

μ	Dynamic viscosity [Pa-s]
ν	Kinematic viscosity [m^2/s]
ξ	Mole fraction
ρ	Density [kg/m^3]
ρ_1	Light gas density [kg/m^3]
ρ_2	Heavy gas density [kg/m^3]
$\boldsymbol{\omega}$	Vorticity vector [1/s]
Φ	Fluorescence quantum yield [-]
π	Energy flux [-]
Π	Integrated energy flux [-]
σ	Absorption cross-section [m^2]
τ	Normalised time [-]
$\overline{\sigma}^l_j$	Sub-filter scale scalar stress [-]
χ	Dissipation [-]
ζ	exponent [-]

Hebrew Symbols

$\beth[F, G]$ The shorthand for terms in the power spectra transport equations.

Subscripts

ξ Referring to scalar field

w Referring to stream-wise velocity field

S, p Referring to term in structure function evolution equation of order p

0 Referring to an initial value of a variable after reshock

x Referring to a span-wise related value

z Referring to a stream-wise related value

Superscripts

$+$ Normalised variable

$*$ Complex conjugate

Chapter 1

Introduction

The Rayleigh-Taylor instability (RTI) [34] is an acceleration-driven instability at an interface between a heavy and a light fluid. Growth of the RTI occurs when the direction of the acceleration is such that the heavy gas is accelerated in the direction of the light gas. The Richtmyer-Meshkov instability (RMI) [39] is a limiting case of the RTI when the fluid layers are impulsively accelerated in a direction normal to the interfaces between the layers. In the RTI case, stable configurations are possible. In the RMI however, stable conditions do not occur, thus upon impulsive acceleration, perturbations away from a planar interface will always begin to grow.

The RMI is seen as a primary cause of inefficiency in attempts to produce energy via inertial confinement fusion (ICF) [20]. The capsule and fuel form a material interface, and the process of compression with intense x-rays causes the propagation of a shock across this boundary. This interaction leads to the mixing of the fuel and capsule material and reduction of yield. The instability has also been proposed as an important mechanism to increase efficiency of mixing of fuel and oxidant in hypersonic aero-engines [21]. A deeper understanding of shock-driven mixing is therefore the main objective of investigations of the RMI. The experimental study of the RMI often involves the use of a shock wave in a shock tube. This is the setting originally used by Meshkov [24] to experimentally confirm Richtmyer′s theory [38]. Previous studies of the RMI have used various initial conditions that can be summarised as the following: 1) nitro-cellulose membranes [51] that provide a repeatable interface geometry and allow

for gravitationally unstable configurations to be investigated; 2) membrane-free interfaces including vertical gas curtains [31]; 3) gravitationally stable horizontal interfaces perturbed using oscillations of the entire shock tube [16], pistons [58], loudspeakers [19]; 4) transverse gas injection [56]; and 5) precisely orientable shock tubes that can be rotated to a desired angle from vertical [22].

Previous studies have used a variety of different diagnostics for quantifying the RMI development, including schlieren [51], particle image velocimetry (PIV) [33], correlation image velocimetry (CIV) [36], and planar laser-induced fluorescence (PLIF) [5]. Recent investigations have combined multiple techniques with high-speed imaging [25, 3, 28]. A comprehensive review of the state of the art is presented by Zhou [60, 61].

Numerical experiments have explored some of the terms in the transport of kinetic energy in wavenumber space such as in Cook and Zhou [6] for the RTI case and in Thornber and Zhou [46] for the RMI case, while a similar study of the combined scalar and kinetic fields has not been performed to date. The integrated kinetic energy spectrum and density fluctuation spectrum in the RMI were studied by Schilling *et al*. [43] and Tritschler *et al*. [49] using data from numerical simulations.

The scalar energy spectrum is explored in a number of experimental studies. Weber *et al*. [57] and Reese *et al*. [36] looked at the evolution of the scalar spectrum for the current initial condition (IC) after a single shock and found a small but growing wavenumber range with a $-\frac{5}{3}$ Kolmogorov scaling. Without access to time-resolved data, a connection to IC structure could not be made.

Structure functions of the density field of a gas curtain after shock are studied by Tomkins *et al*. [48] who found exponents greater than expected by Kolmogorov-Obukhov-Corrsin (KOC) scaling.

Data from the high-speed experiments discussed here have been used to analyze the evolution of moments of the light gas mole fraction field by Noble *et al*. [28] and the evolution of the scalar power spectrum and structure functions by Noble *et al*. [29] and have been used as an experimental example of an iterative fluorescence correction scheme to extract estimates of the light gas mole fraction by Herzog *et al*. [13].

This work begins in chapter 2 with an exploration of the equations of motion that describe the evolution of the mixing layer, delving into transforming them into forms relevant to the extraction of insights into different mechanisms. Chapter 3 describes the experimental setup used for the three sets of experiments and the process of arriving at the setups that were used. Results derived from the data collected and the analysis described are presented in chapter 4.

The purpose of this work is to push the envelope of knowledge of the RM instability. It is making an effort to continue to push the description of these flows beyond the traditional "thickness growth rate" metric that was dictated (for many years) by the limits of diagnostic techniques. The aim is to first explain why a widely used dimensionless measure of time evolution is reasonable for interface mixing problems in general, and RM and RT problems specifically and provide a sound basis for its use. Once the coordinate system is created, methods that have evolved to analyze canonical turbulence problems are transformed into this coordinate system so they can be brought to bear on the inhomogeneous anisotropic flow that results due to the RMI. Mature experimental techniques are combined with new technology in a novel way to acquire previously unattainable, time-resolved measurements of mixing due to the RMI . These measurements allow for the evaluation of metrics commonly used in the study of homogeneous isotropic turbulence (like structure functions, power spectra of the scalar

and velocity fields, individual terms in the power spectra time-evolution equations) and the comparison to their HIT counterparts, as well as comparison to computational studies that have been able to access these metrics for quite a while now. The ultimate objective is to identify new scalings that apply to these shock-driven flows to aid in the development of models and to provide benchmarking data for the validation of hydrocodes.

Chapter 2

Background

2.1 Governing Equations and Normalisation

As a shock wave interacts with a gas interface, it deposits vorticity fluctuations and therefore velocity fluctuations onto the interface. Starting from the full 3D Navier-Stokes equations with a convective equation for scalar transport, a set of normalised equations for the time evolution of moments of the fluctuations is presented. After the shock has passed, the resulting flow is treated as incompressible as the resulting convective Mach number is small, and so compressibility effects can be shown to be higher order corrections to the transport equations [8]. The equations for mass, momentum and light gas mole fraction are:

$$\frac{\partial \rho}{\partial t} + \boldsymbol{\nabla} \cdot (\rho \boldsymbol{u}) = 0 \tag{1}$$

$$\frac{\partial (\rho \boldsymbol{u})}{\partial t} + \boldsymbol{\nabla} \cdot \rho \boldsymbol{u}\boldsymbol{u} = -\boldsymbol{\nabla} p + \boldsymbol{\nabla} \cdot (\mu \boldsymbol{\nabla} \boldsymbol{u}) \tag{2}$$

$$\frac{\partial (\rho \xi)}{\partial t} + \boldsymbol{\nabla} \cdot \rho \boldsymbol{u} \xi = \rho \mathcal{D} \boldsymbol{\nabla}^2 \xi \tag{3}$$

where ρ is the mass density, $\boldsymbol{u}$ is the velocity, p is the pressure, μ the viscosity, $\mathcal{D}$ is the mass diffusivity and ξ is the mole fraction of the light gas. x, y, z are the spanwise, normal and

streamwise directions, respectively.

In preparation for the analysis of the concentration and velocity fields that are measured in the experiments, we specialise to 2D and introduce the following non-dimensionalisations:

$$x = x^+ W,\ t = \tau \frac{\dot{h}_0}{h_0},\ z = z^+ h + z_0,\ p = p^+ p_0,\ \rho = \rho^+ \rho_0,\ \boldsymbol{u} = \boldsymbol{V_0} + \boldsymbol{u}^+ \dot{h} \tag{4}$$

where W is a representative spanwise lengthscale (here the width of the shock tube), $h = 4\int_{-\infty}^{\infty} \overline{\xi}(1-\overline{\xi})\mathrm{d}z$ is the mixing width, h_0 is the minimum mixing width after reshock, $\dot{h}$ is the growth rate, $\dot{h}_0$ is the growth rate immediately after reshock, p_0 is the post-reshock pressure, ρ_0 is the light gas post-reshock bulk density, z_0 is the mole-fraction weighted centroid of the mixing layer, $\boldsymbol{V}_0$ is the bulk interface velocity and $\boldsymbol{u}^+ = [u^+, v^+, w^+]^T$ is the normalised fluctuating velocity. Then equations (1) - (3) rewrite as:

$$\frac{1}{C_h}\frac{\partial \rho^+}{\partial \tau} - z^+\frac{\partial \rho^+}{\partial z^+} + \frac{\partial \rho^+ u^+}{\partial x^+}\frac{h}{W} + \frac{\partial \rho^+ w^+}{\partial z^+} = 0 \tag{5}$$

$$\begin{aligned}\frac{1}{C_h}\frac{\partial w^+}{\partial \tau} - z^+\frac{\partial w^+}{\partial z^+} + \frac{\partial u^+ w^+}{\partial x^+}\frac{h}{W} + \frac{\partial w^{+2}}{\partial z^+} = -\frac{1}{\gamma M_h^2}\frac{1}{\rho^+}\frac{\partial p^+}{\partial z^+} + \\ \frac{1}{Re_h}\frac{1}{\rho^+}\left[\frac{\partial \mu^+}{\partial x}\frac{\partial w^+}{\partial x}\left(\frac{h}{W}\right)^2 + \frac{\partial \mu^+}{\partial z}\frac{\partial w^+}{\partial z}\right] + \frac{1}{Re_h}\frac{1}{\rho^+}\left[\frac{\partial^2 w^+}{\partial x^{+2}}\left(\frac{h}{W}\right)^2 + \frac{\partial^2 w^+}{\partial z^{+2}}\right] \\ -\frac{\dot{V}_0 h}{\dot{h}^2} - w^+\frac{\ddot{h}h}{\dot{h}^2}\end{aligned} \tag{6}$$

$$\frac{1}{C_h}\frac{\partial \xi}{\partial \tau} - z^+\frac{\partial \xi}{\partial z^+} + \frac{\partial u^+ \xi}{\partial x^+}\frac{h}{W} + \frac{\partial w^+ \xi}{\partial z^+} = \frac{1}{Re_h Sc}\left[\frac{\partial^2 \xi}{\partial x^{+2}}\left(\frac{h}{W}\right)^2 + \frac{\partial^2 \xi}{\partial z^{+2}}\right] \tag{7}$$

where $C_h = \dfrac{\dot{h}}{\dot{h}_0}\dfrac{h_0}{h}$ is the dimensionless growth parameter, $M_h = \dfrac{\dot{h}}{c}$ is the interface Mach number with c being the speed of sound in the light gas, $Re_h = \dfrac{h\dot{h}}{\nu}$ is the interface Reynolds

number and $Sc = \dfrac{\nu}{D}$ is the interface Schmidt number.

This normalisation transforms the NS equations into the frame of reference moving with the center of the interface and also scales the equations by the instantaneous mixing width and the instantaneous growth rate of the interface.

By performing a change of variables using the time varying growth rate parameter,

$$\frac{1}{C_h}\frac{\partial \xi}{\partial \tau} = h^+ \frac{\partial \tau}{\partial h^+}\frac{\partial \xi}{\partial \tau} = h^+ \frac{\partial \xi}{\partial h^+} = \frac{\partial \xi}{\partial \ln h^+} \tag{8}$$

$\ln h^+$ becomes a measure of time in this system [27], where $h^+ = \dfrac{h}{h_0}$ is the normalised mixing width. This allows Eqns. (6-7) to be rewritten as:

$$\begin{aligned} \frac{\partial w^+}{\partial \ln h^+} - z^+\frac{\partial w^+}{\partial z^+} + \frac{\partial u^+ w^+}{\partial x^+}\frac{h}{W} + \frac{\partial w^{+2}}{\partial z^+} = -\frac{1}{\gamma M_h^2}\frac{1}{\rho^+}\frac{\partial p^+}{\partial z^+} + \\ \frac{1}{Re_h}\frac{1}{\rho^+}\left[\frac{\partial \mu^+}{\partial x}\frac{\partial w^+}{\partial x}(\frac{h}{W})^2 + \frac{\partial \mu^+}{\partial z}\frac{\partial w^+}{\partial z}\right] + \frac{\mu^+}{Re_h}\frac{1}{\rho^+}\left[\frac{\partial^2 w^+}{\partial x^{+2}}\left(\frac{h}{W}\right)^2 + \frac{\partial^2 w^+}{\partial z^{+2}}\right] - \\ \frac{\dot{V}_0 h}{\dot{h}^2} - w^+\frac{\ddot{h}h}{\dot{h}^2} \end{aligned} \tag{9}$$

$$\frac{\partial \xi}{\partial \ln h^+} - z^+\frac{\partial \xi}{\partial z^+} + \frac{\partial u^+ \xi}{\partial x^+}\frac{h}{W} + \frac{\partial w^+ \xi}{\partial z^+} = \frac{1}{Re_h Sc}\left[\frac{\partial^2 \xi}{\partial x^{+2}}\left(\frac{h}{W}\right)^2 + \frac{\partial^2 \xi}{\partial z^{+2}}\right] \tag{10}$$

2.2 Spanwise Averaged Moments

The normalised governing equations can be averaged across the width of the shock tube in the spanwise, or x-direction. This leads to a series of ascending order moment equations for w^+, u^+ and ξ. The first-order equations for $\overline{\xi}$ and $\overline{p^+}$ and the second-order equations for $\overline{\xi'^2}$, $\overline{w^{+2}}$,

and $\overline{u^{+2}}$ are shown here (Eqs.(12)-(16)). We define the spanwise average of any quantity f as

$$\overline{f} = \frac{1}{W}\int_0^W f \, \mathrm{d}x \tag{11}$$

such that $\xi = \overline{\xi} + \xi'$.

$$\frac{\partial \overline{\xi}}{\partial \ln h^+} - z^+\frac{\partial \overline{\xi}}{\partial z^+} + \frac{\partial \overline{w^+\xi'}}{\partial z^+} = \frac{1}{Re_h S\, c}\frac{\partial^2 \overline{\xi}}{\partial z^{+2}} \tag{12}$$

$$\frac{\partial \overline{p^+}}{\partial z^+} = -\gamma M_h^2\, \overline{\rho^+}\, \frac{\partial \overline{w^{+2}}}{\partial z^+} - \overline{\rho^+}\, G_{z_0} \tag{13}$$

$$\frac{\partial \overline{\xi'^2}}{\partial \ln h^+} - z^+\frac{\partial \overline{\xi'^2}}{\partial z^+} + \overline{w^+\xi'}\frac{\partial \overline{\xi}}{\partial z^+} + \frac{\partial \overline{w^+\xi'^2}}{\partial z^+} = \frac{1}{Re_h S\, c}\frac{\partial^2 \overline{\xi'^2}}{\partial z^{+2}} - C_\chi \tag{14}$$

$$\frac{\partial \overline{w^{+2}}}{\partial \ln h^+} - z^+\frac{\partial \overline{w^{+2}}}{\partial z^+} + \frac{2}{3}\frac{\partial \overline{w^{+3}}}{\partial z^+} = -\frac{1}{\gamma M_h^2}\frac{\overline{w^+}\,\overline{\partial p^+}}{\overline{\rho^+}} + \frac{1}{Re_h}\frac{1}{\overline{\rho^+}}\frac{\partial^2 \overline{w^{+2}}}{\partial z^{+2}} - \frac{C_{\epsilon,w}}{\overline{\rho^+}} - \overline{w^{+2}}G_h - 2\frac{\overline{w^+\rho'}}{\overline{\rho^+}}G_{z_0} \tag{15}$$

$$\frac{\partial \overline{u^{+2}}}{\partial \ln h^+} - z^+\frac{\partial \overline{u^{+2}}}{\partial z^+} + \frac{2}{3}\frac{\partial \overline{u^{+2}w^+}}{\partial z^+} = \frac{1}{Re_h}\frac{1}{\overline{\rho^+}}\frac{\partial^2 \overline{u^{+2}}}{\partial z^{+2}} - \frac{C_{\epsilon,u}}{\overline{\rho^+}} \tag{16}$$

where $G_{z_0} = \dfrac{\dot{V}_0 h}{\dot{h}^2}$ is the bulk interface forcing, $G_h = \dfrac{\ddot{h}h}{\dot{h}^2}$ is the "fictitious" growth rate forcing, $C_\chi = \dfrac{2}{Re_h S\, c}\dfrac{\overline{\xi'^2}}{\lambda_\xi^{+2}}$ is the normalised scalar dissipation, $C_{\epsilon,u} = \dfrac{2}{Re_h}\dfrac{\overline{u^{+2}}}{\lambda_u^{+2}}$ is the normalised spanwise dissipation and $C_{\epsilon,w} = \dfrac{2}{Re_h}\dfrac{\overline{w^{+2}}}{\lambda_w^{+2}}$ is the normalised streamwise dissipation. $\lambda_\xi,\ \lambda_u$ *and* λ_w are the Taylor scales for the scalar, u and w fields respectively.

In the post-reshock linear growth regime, these extra forcing terms, G_{z_0} and G_h, which are

due to the choice of coordinate system, go to zero.

2.2.1 Higher Order Normalised Moments

Equations (12 - 16) describe the evolution of the first and second order moments of the scalar and velocity fields, however they include derivatives of higher-order mixed moments. The skewness S_ξ and kurtosis K_ξ of the light-gas mole fraction spanwise distributions are defined as

$$S_\xi = M_{03} = \frac{m_{03}}{m_{02}^{3/2}} \tag{17}$$

$$K_\xi = M_{04} = \frac{m_{04}}{m_{02}^{2}} \tag{18}$$

$$m_{ij} = \frac{1}{W}\int_0^W w^{*i}\xi'^{j}\,\mathrm{d}x \tag{19}$$

The skewness describes the asymmetry about the mean of a distribution. The kurtosis characterizes how prominent outliers or tails of the distribution are.

Schopflocher and Sullivan [44] explored a two parameter PDF-based model to describe the appearance of a relationship between the skewness and kurtosis of the scalar field in grid-generated turbulent plume data. They derived expressions for the skewness, S_ξ, and kurtosis, K_ξ in terms of the mean concentration, $\overline{\xi}$.

$$S_\xi = \frac{\overline{\xi}(a_3 - 3a_2\overline{\xi} + 2\overline{\xi}^2)}{(\overline{\xi}(a_2 - \overline{\xi}))^{\frac{3}{2}}} \tag{20}$$

$$K_{\xi} = \frac{\overline{\xi}(a_4 - 4a_3\overline{\xi} + 6a_2\overline{\xi}^2 - 3\overline{\xi}^3)}{(\overline{\xi}(a_2 - \overline{\xi}))^2} \tag{21}$$

where a_i are fitting parameters. This leads to a parabolic relationship of the form

$$K_{\xi} = AS_{\xi}^2 + B \tag{22}$$

with the coefficients in general being time dependent. These concepts can be extended to higher orders leading to a normalised mixed moment tensor

$$M_{ij} = \frac{m_{ij}}{\sqrt{\overline{w^2}^i \, \overline{\xi^2}^j}}. \tag{23}$$

2.3 Integral Measures

2.3.1 Interface thickness

Reshock Growth Rate Estimate

Here, an extension of previous work by Weber [55] will be considered to allow an estimate of the post-reshock growth rate $\dot{h}_{0^+}$ using the pre-reshock growth rate $\dot{h}_{0^-}$ and the reshock IC concentration field. This is to provide an alternative to models that require fitting parameters that vary based on the type of IC. Starting with the inviscid momentum equation

$$\frac{\partial \rho w}{\partial t} = -\frac{\partial p}{\partial z}, \tag{24}$$

and the vorticity transport equation with only the baroclinic term

$$\frac{\partial \omega}{\partial t} = -\frac{1}{\rho^2}\frac{\partial p}{\partial z}\frac{\partial \rho}{\partial x} \tag{25}$$

leads to

$$\frac{\partial \omega}{\partial t} = \frac{1}{\rho^2}\frac{\partial \rho w}{\partial t}\frac{\partial \rho}{\partial x}. \tag{26}$$

Second order terms here constitute about a 5% difference in the resulting estimate. Integrating over the interaction time leads to

$$\omega = \frac{\Delta V_0}{\rho}\frac{\partial \rho}{\partial x} \tag{27}$$

where ΔV_0 is the change in interface translational velocity due to the interaction of the shock wave with the interface. Equation 27 expands into

$$\frac{\partial w'}{\partial x} - \frac{\partial u'}{\partial z} = -\frac{\Delta V_0}{\rho}\frac{\partial \rho}{\partial x}. \tag{28}$$

Combining with the compressibility condition then an equation for the Laplacian of w' can be constructed:

$$\frac{\vec{\nabla}^2 w'}{\Delta V_0} = \frac{\partial^2 \ln\left(\rho/\rho_0\right)'}{\partial x^2}. \tag{29}$$

Then assuming spanwise fluctuations are of a high enough frequency and that the interface is diffuse such that spanwise gradients dominate this can be approximated as:

$$\frac{w'}{\Delta V_0} = -(\ln \rho/\rho_0)' \tag{30}$$

which leads to an estimate of the initial growth rate immediately after wave interaction of

$$\frac{\dot{h}_{0^+}}{\Delta V_0} = 8 \int_{-\infty}^{\infty} \overline{(\ln \rho/\rho_0)' \xi'} \frac{\partial \bar{\xi}}{\partial z} \mathrm{d}z - \frac{\dot{\mathrm{h}}_{0^-}}{\Delta \mathrm{V}_0}. \tag{31}$$

All the quantities in Eq.(31) were be measured experimentally and this model is compared to experimental data in Chapter 4.

2.4 Spectral Analysis

2.4.1 Power Spectra

The power spectrum of a given quantity describes how the energy of that quantity is distributed in wavenumber space, *i.e*. how much energy is contained in structures of a given scale. Here, the transport equations for the scalar energy and kinetic energy spectra are derived and each term described and its underlying physical mechanism elucidated. The distribution of energy in scale space is of interest in and of itself, however understanding the physical mechanisms that develop this distribution is also of interest, especially how these mechanisms may be affected by changes in IC structure and parameters such as Mach number and Atwood number. Following Thornber and Zhou[46] by introducing $\boldsymbol{v}_i = \sqrt{\rho^+}\boldsymbol{u}_i^+$ and taking the Fourier transform $\left(\widehat{f}(k_x^+, z^+, \ln h^+) = \mathcal{F}_{x^+}[f(x^+, z^+, \ln h^+)]\right)$ of Eqs.(9 and 10), and multiplying by the complex conjugate of the Fourier transform of each variable, an evolution equation for the scalar and

velocity power spectra ($E_\xi = \widehat{\xi}\widehat{\xi}^*$ and $E_w = \widehat{\boldsymbol{v}_3^+}\widehat{\boldsymbol{v}_3^+}^*$) can be found

$$\frac{\partial E_\xi}{\partial \ln h^+} - z^+\frac{\partial E_\xi}{\partial z^+} + \mathcal{P} + \mathcal{T}_{x\xi} + \mathcal{T}_{z\xi} = \mathcal{D}_{x\xi} + \mathcal{D}_{z\xi} - \chi_\xi \tag{32a}$$

$$\frac{\partial E_w}{\partial \ln h^+} - z^+\frac{\partial E_w}{\partial z^+} + \mathcal{T}_{xw} + \mathcal{T}_{zw} = -\mathcal{H}_w + \mathcal{G}_x + \mathcal{G}_z + \mathcal{D}_{xw} + \mathcal{D}_{zw} \tag{32b}$$

with each term defined in Table 1. The transport terms can be represented as gradients of flux such that the inhomogeneous flux π_z is defined implicitly as

$$\frac{\partial \pi_z}{\partial z^+} = \mathcal{T}_z \tag{33}$$

and the homogeneous flux π_x may be defined implicitly as

$$\frac{\partial \pi_x}{\partial k_x^+} = \mathcal{T}_x \tag{34}$$

Following Schilling *et al*. [42], to find a representative scalar power spectrum and kinetic energy spectrum, the spatially varying spectra are integrated in the inhomogeneous streamwise direction as described by

$$\Lambda_\xi(k_x^+, h^+) = \int_{-\infty}^{\infty} E_\xi \, \mathrm{d}z^+ \tag{35}$$

$$\Lambda_w(k_x^+, h^+) = \int_{-\infty}^{\infty} E_w \, \mathrm{d}z^+ \tag{36}$$

where the limits are $\pm\infty$ rather than the bubble and spike heights that were used by Schilling *et al*.

The terms defined in Table 1, for both E_ξ and E_w can be described as follows:

	E_ξ	E_w
Production $\mathcal{P}$	$\beth[w^+, \xi]\frac{\partial \bar{\xi}}{\partial z^+}$	N/A
Transport $\mathcal{T}_x$	$\frac{h}{W}\beth\left[\frac{\partial u^+\xi}{\partial x^+}, \xi\right]$	$\frac{1}{2}\frac{h}{W}\beth\left[\frac{1}{\sqrt{\rho^+}}\frac{\partial v_1 v_3}{\partial x^+}, v_3\right]$
Transport $\mathcal{T}_z$	$\beth\left[\frac{\partial w^+\xi}{\partial z^+}, \xi\right]$	$\frac{1}{2}\beth\left[\frac{1}{\sqrt{\rho^+}}\frac{\partial v_3 v_3}{\partial z^+}, v_3\right]$
Pressure $\mathcal{H}_w$	N/A	$\frac{1}{\gamma M_h^2}\beth\left[\frac{1}{\sqrt{\rho^+}}\frac{\partial p^+}{\partial z^+}, v_3\right]$
Momentum Diffusivity Gradient $\mathcal{G}_x$	N/A	$\left(\frac{h}{W}\right)^2\frac{1}{Re_h}\beth\left[\frac{1}{\sqrt{\rho^+}}\frac{\partial \mu^+}{\partial x^+}\frac{\partial w^+}{\partial x^+}, v_3\right]$
Momentum Diffusivity Gradient $\mathcal{G}_z$	N/A	$\frac{1}{Re_h}\beth\left[\frac{1}{\sqrt{\rho^+}}\frac{\partial \mu^+}{\partial z^+}\frac{\partial w^+}{\partial z^+}, v_3\right]$
Diffusion $\mathcal{D}_x$	$\frac{-2k^{+2}}{Re_h Sc}\left(\frac{h}{W}\right)^2 E_\xi$	$\left(\frac{h}{W}\right)^2\frac{1}{Re_h}\beth\left[\frac{1}{\sqrt{\rho^+}}\mu\frac{\partial^2 w^+}{\partial x^{+2}}, v_3\right]$
Diffusion $\mathcal{D}_z$	$\frac{1}{Re_h Sc}\left[\frac{\partial^2 E_\xi}{\partial z^{+2}}\right]$	$\frac{1}{Re_h}\beth\left[\frac{1}{\sqrt{\rho^+}}\mu\frac{\partial^2 w^+}{\partial z^{+2}}, v_3\right]$
Dissipation χ	$\frac{1}{Re_h Sc}\left[\frac{\partial \widehat{\xi}}{\partial z^+}\frac{\partial \widehat{\xi^*}}{\partial z^+}\right]$	N/A

Table 1: Terms in scalar and kinetic energy spectra transport, where $\beth[F, G] = \hat{F}^*\hat{G} + \hat{F}\hat{G}^*$

1. Production $\mathcal{P}$ - Fluctuations of the scalar field feed off the mean scalar gradient producing fluctuating "scalar energy".

2. Fictitious transport - This term is the second term in Eqs.(32a and 32b) and is an artifact of the choice of coordinate system. This term accounts for the transport of fluctuations due to the growth of the thickness of the mixing layer.

3. Homogeneous transport $\mathcal{T}_x$ - This is transport of fluctuating energy in wavenumber space, it transports energy from large scale structures to smaller scales and vice-versa.

4. Homogeneous transport $\mathcal{T}_x$ - This is transport of fluctuating energy in wavenumber space, it transports energy from large scale structures to smaller scales and vice-versa.

5. Inhomogeneous transport $\mathcal{T}_z$ - Transport of energy in the vertical direction due to non-linear interaction of fluctuations.

6. Pressure transport $\mathcal{H}_w$ - Pressure is not measured in this work, so this term cannot be calculated. This term represents the effect of pressure fluctuations on the kinetic power spectrum and is one of the components that drives a return to isotropy of incompressible flows [4].

7. Diffusivity gradient $\mathcal{G}_x + \mathcal{G}_z$ - A dissipation-like term, though not positive definite, the interplay between gradients of diffusivity and the velocity field allow destruction of kinetic energy or addition of energy through interaction with the scalar field depending on the orientation of the gradients of the two fields.

8. Homogeneous diffusion $\mathcal{D}_x$ - Transport in wavenumber space due to molecular diffusion.

9. Inhomogeneous diffusion $\mathcal{D}_z$ - Diffusion of energy due to molecular processes in the streamwise direction due to gradients in the inhomogeneous direction.

10. Dissipation χ - Diffusive destruction of energy due to interaction of gradients of fluctuations.

The spectral slopes are defined as

$$\zeta_\xi = \frac{\partial \ln E_\xi}{\partial \ln k}|_{k=k_{\lambda_\xi}} \tag{37a}$$

$$\zeta_w = \frac{\partial \ln E_w}{\partial \ln k}|_{k=k_{\lambda_w}} \tag{37b}$$

where the derivatives are evaluated within the inertial range at the Taylor microscale wavenumber.

2.4.2 Energy Partition: concentration only

To analyse the total change in energy over a given time, each term in the transport equation is integrated over dimensionless time ($\ln h^+$) to the latest time available in all HS experiments, $h^+ = 8$, resulting in Eqs. (38)-(40). These allow an analysis of the different contributions to the total change in the energy spectra.

$$T_\xi(z^+, k_x^+) = \int_0^{\ln 8} z^+ \frac{\partial E_\xi}{\partial z^+} \, \mathrm{d} \ln h^+ \tag{38}$$

$$\Pi_\xi(z^+, k_x^+) = \int_0^{\ln 8} (\mathcal{T}_{x\xi} \; + \; \mathcal{T}_{z\xi} \; + \; \mathcal{P}) \, \mathrm{d} \ln h^+ \tag{39}$$

$$D_\xi(z^+, k_x^+) = \int_0^{\ln 8} \mathcal{D}_{x\xi} \; + \; \mathcal{D}_{z\xi} \, \mathrm{d} \ln h^+ \tag{40}$$

$$X_\xi(z^+, k_x^+) = \int_0^{\ln 8} \chi_\xi \, \mathrm{d} \ln h^+ \tag{41}$$

This leads to a form of the scalar power spectrum transport equation that has been integrated over dimensionless time. Each of these terms can be considered separately to identify its contribution to the total change in energy:

$$\Delta E_\xi = E_\xi|_{h^+=8} - E_\xi|_{h^+=0} = T_\xi - \frac{1}{2}\frac{\partial \Pi_\xi}{\partial k_x^+} + D_\xi - X_\xi \tag{42}$$

2.4.3 Energy Partition: velocity and concentration

For HSS experiments, if both velocity and mole fraction can be measured, then more terms in the transport equations may be directly analyzed. Then, to analyse the total change in energy over a given time, each term in the equations for velocity and scalar transport is integrated over dimensionless time ($\ln h^+$) to the latest time available in all experiments, $h^+ = 5$, resulting in Eqs. (43)-(49). These allow an analysis of the different contributions to the total change in the energy spectra.

$$P_\xi(z^+, k_x^+) = \int_0^{\ln 5} -\mathcal{P} \, \mathrm{d} \ln h^+ \tag{43}$$

$$\begin{aligned} T_{x\xi}(z^+, k_x^+) &= \int_0^{\ln 5} \mathcal{T}_{x,\xi} \, \mathrm{d} \ln h^+ \\ T_{xw}(z^+, k_x^+) &= \int_0^{\ln 5} \mathcal{T}_{x,w} \, \mathrm{d} \ln h^+ \end{aligned} \tag{44}$$

$$\begin{aligned} \Pi_{z\xi}(z^+, k_x^+) &= \int_{-\infty}^{z^+} \int_0^{\ln 5} \mathcal{T}_{z,\xi} \, \mathrm{d} \ln h^+ \, \mathrm{d}z^+ \\ T_{zw}(z^+, k_x^+) &= \int_0^{\ln 5} \mathcal{T}_{z,w} \, \mathrm{d} \ln h^+ \end{aligned} \tag{45}$$

$$G_w(z^+, k_x^+) = \int_0^{\ln 5} (\mathcal{G}_x + \mathcal{G}_z)\, \mathrm{d}\ln h^+ \tag{46}$$

$$\begin{aligned} D_{x\xi}(z^+, k_x^+) &= \int_0^{\ln 5} \mathcal{D}_{k,\xi}\, \mathrm{d}\ln h^+ \\ D_{xw}(z^+, k_x^+) &= \int_0^{\ln 5} \mathcal{D}_{k,w}\, \mathrm{d}\ln h^+ \end{aligned} \tag{47}$$

$$\begin{aligned} D_{z\xi}(z^+, k_x^+) &= \int_0^{\ln 5} \mathcal{D}_{z,\xi}\, \mathrm{d}\ln h^+ \\ D_{zw}(z^+, k_x^+) &= \int_0^{\ln 5} \mathcal{D}_{z,w}\, \mathrm{d}\ln h^+ \end{aligned} \tag{48}$$

$$X_\xi(z^+, k_x^+) = \int_0^{\ln 5} \chi_\xi\, \mathrm{d}\ln h^+ \tag{49}$$

This leads to a form of the scalar and kinetic power spectra transport equations that have been integrated over dimensionless time. Each of these terms can be considered separately to identify its contribution to the total change in energy:

$$\Delta E_\xi = P_\xi - T_{x\xi} - \frac{\partial \Pi_{z\xi}}{\partial z^+} + D_{x\xi} + D_{z\xi} - X_\xi \tag{50a}$$

$$\Delta E_w = -T_{xw} - T_{zw} - H_w + G_w + D_{xw} + D_{zw} \tag{50b}$$

2.4.4 Structure Functions and Exponents

A different, but related, measure of the distribution of energy in scale space is the analysis of the structure function. Defining the p^{th}-order structure function as

$$S_{\xi,p}(z^+, r^+, h^+) = \overline{\delta\xi^p} = \overline{(\xi_2 - \xi_1)^p} = \overline{(\xi(x^+ + r_x^+) - \xi(x^+))^p} = \overline{(\xi(X^+ + r_x^+/2) - \xi(X^+ - r_x^+/2))^p}, \tag{51}$$

and using Eq. (10), a Karman-Howarth-Monin type transport equation can be derived following the example of Hill [14] and Gauding *et al.* [10]. Here $r_x^+ = \dfrac{r_x}{W}$ is the two-point separation in the spanwise direction; the subscripts 1 and 2 refer to point one and point two where point one is at the x^+ location while point 2 is offset by the separation r^+ and X^+ is the average location between point one and point two. The result is

$$\frac{\partial S_{\xi,p}}{\partial \ln h^+} - z^+ \frac{\partial S_{\xi,p}}{\partial z^+} + \mathcal{T}_{S,p} + \mathcal{P}_{S,p} = \mathcal{D}_{S,p} - \chi_{S,p} + \chi_{Xp} \tag{52}$$

with the terms defined in Table 2 and Eq.(53)

$$\chi_{S,p} = \frac{1}{Re_h Sc}\left[p(p-1)\overline{\delta\xi^{p-2}\left(\frac{\partial\,\delta\xi}{\partial z^+}\right)^2} + p(p-1)\overline{\delta\xi^{p-2}\left(\frac{\partial\,\delta\xi}{\partial r^+}\right)^2 + \delta\xi^{p-2}\left(\frac{\partial\,\delta\xi}{\partial X^+}\right)^2}\left(\frac{h}{W}\right)^2\right] \tag{53}$$

where the Yaglom equation derived in [10] is extended to allow inhomogeneity in the streamwise direction. A Yaglom equation is the scalar equivalent of a Karman-Howarth-Monin equation for the transport of the p^{th}-order structure function.

Following the same idea as with the power spectra, the structure function is integrated in

the streamwise direction such that

$$Z_{\xi,p} = \int_{-\infty}^{\infty} S_{\xi,p}\, \mathrm{d}z^{+} \tag{54}$$

	$S_{\xi,p}$
Production $\mathcal{P}$	$p\,\overline{\delta\xi^{p-1}\,\delta w^{+}}\dfrac{\partial\overline{\xi}}{\partial z^{+}}$
Transport $\mathcal{T}$	$\dfrac{\partial}{\partial r^{+}}\left[p\overline{[(u^{+}\xi')_2 + (u^{+}\xi')_1]\,\delta\xi^{p-1}}\right]$ + $\dfrac{\partial}{\partial z^{+}}\left[p\overline{\delta(w^{+}\xi')\,\delta\xi^{p-1}}\right]$
Diffusion $\mathcal{D}$	$\dfrac{1}{Re_h Sc}\left[\dfrac{\partial^2 S_{\xi,p}}{\partial r^{+2}}\left(\dfrac{h}{W}\right)^2 + \dfrac{\partial^2 S_{\xi,p}}{\partial z^{+2}}\right]$
Dissipation χ	Eq.(53)
Dissipation χ_X	$\dfrac{-1}{Re_h Sc}\overline{p\delta\xi^{p-1}\left(\dfrac{\partial\,(\xi_2+\xi_1)}{\partial r^{+}\partial X^{+}}\right)}$

Table 2: Terms in structure function transport

The power law behaviour of the integrated structure function is described by

$$\zeta_{\xi,p} = \frac{\partial \ln Z_{\xi,p}}{\partial \ln r_x^{+}}\Big|_{r_x^{+}=\lambda^{+}} \tag{55}$$

which takes a constant value at intermediate separations over a large range of p. Obukhov-Corrisin scaling of the light gas mole-fraction field implies that $\zeta_{\xi,p} = \dfrac{p}{3}$. Kraichnan proposed to use a model for the diffusion of scalars which led to a scaling of $\zeta_{\xi,p} \propto \sqrt{p}$ for large p.

2.5 Filter based analysis

2.5.1 Mechanisms of scale-to-scale transport

An alternative approach to exploring scale-to-scale interactions employs a filter-based analysis. Here, the treatment provided by Johnson [15] to the velocity field is extended to the scalar field. A filter, G_l, is convolved with the scalar field.

$$\overline{\xi}^l = G_l * \xi \tag{56}$$

Here a Gaussian filter is used, defined as:

$$G = \mathcal{N} * \exp\left(-(x^{+2} + z^{+2})/(2l^+)^2\right) \tag{57}$$

where $\mathcal{N} = (2\pi l^{+2})^{-3/2}$ is the normalization parameter. Applying Eq. (56) to Eq. (10) leads to an evolution equation for the filter scale scalar energy ($E^l_\xi = \frac{1}{2}\overline{\xi}^l\overline{\xi}^l$)

$$\frac{\partial E^l_\xi}{\partial \ln h^+} - z^+\frac{\partial E^l_\xi}{\partial z^+} + \frac{\partial T^l_{\xi,i}}{\partial x^+_i} = -\Pi^l - \mathcal{E}^l \tag{58}$$

with $\Pi^l = -\overline{\sigma}^l_j\overline{\xi}^l_{,j}$ and $\overline{\sigma}^l_j = \overline{u_j\xi}^l - \overline{u}^l_j\overline{\xi}^l$. The scale space transport flux $T^l_{\xi,i}$ and scale space diffusion term $\mathcal{E}^l$ describe resolved interactions at the filter scale. To analyse the subscale contributions, and following [15], if G_l is a Gaussian filter then $\overline{\sigma}^l_j$ can be written as the solution of a forced diffusion equation,

$$\frac{\partial^2\overline{\sigma}^l_j}{\partial l^2} = \frac{1}{2}\nabla^2\overline{\sigma}^l_j + \overline{A}^l_{jk}\overline{\xi}^l_{,k} \tag{59}$$

with $A_{jk} = \dfrac{\partial u_j}{\partial x_k}$ being the velocity gradient tensor.

Using the decomposition of the velocity gradient tensor $A_{jk} = S_{jk} + \Omega_{jk}$, where S_{jk} is the strain rate tensor and Ω_{jk} is the rotation tensor, the following contributions to the scale-to-scale transport term can be identified:

$$\Pi^l_{ls} = -l^2 \overline{S}^l_{ik} \overline{\xi}^l_{,i} \overline{\xi}^l_{,k} \tag{60a}$$

$$\Pi^l_{nls} = -\overline{\xi}^l_{,i} \int_0^{l^2} \overline{\overline{S}_{ik}^{\sqrt{\theta}} \overline{\xi}_{,k}^{\sqrt{\theta}}}^{\sqrt{\phi}} - \overline{\overline{S}_{ik}^{\sqrt{\theta}}}^{\sqrt{\phi}} \overline{\overline{\xi}_{,k}^{\sqrt{\theta}}}^{\sqrt{\phi}} \, \mathrm{d}\theta \tag{60b}$$

$$\Pi^l_{nl\Omega} = -\overline{\xi}^l_{,i} \int_0^{l^2} \overline{\overline{\Omega}_{ik}^{\sqrt{\theta}} \overline{\xi}_{,k}^{\sqrt{\theta}}}^{\sqrt{\phi}} - \overline{\overline{\Omega}_{ik}^{\sqrt{\theta}}}^{\sqrt{\phi}} \overline{\overline{\xi}_{,k}^{\sqrt{\theta}}}^{\sqrt{\phi}} \, \mathrm{d}\theta \tag{60c}$$

such that $\Pi^l = \Pi^l_{ls} + \Pi^l_{nls} + \Pi^l_{nl\Omega}$ with Π^l_{ls} being the scale-local strain contribution, Π^l_{nls} being the non-local strain contribution which is the contribution of strain from scales below the filter scale, and $\Pi^l_{nl\Omega}$ being the contribution to transfer due to subfilter vorticity. In Eq. (60a) $\overline{\xi}^l_{,k}$ is the derivative of the filtered scalar field in the x_k direction, $\phi = 1 - \theta$, and θ is a dummy variable for the filter length scale.

2.6 Length Scales

Length scales in the context of power spectra are considered: both the integral scale L and the Taylor microscale λ of a given spectrum are defined via functions of the spectrum such that

$$L = \frac{\int \frac{E}{k}\,\mathrm{dk}}{\int E\,\mathrm{dk}} \tag{61a}$$

$$\lambda^2 = \frac{\int E\,\mathrm{dk}}{\int k^2 E\,\mathrm{dk}} \tag{61b}$$

Then the bandwidth of both the scalar spectra and the density-weighted kinetic spectra can be defined to provide a coarse measure of how energy is distributed between scales:

$$Re_\tau Sc_\tau = \left(\frac{L}{\lambda}\right)_\xi^2 = \frac{\left(\int \frac{E_\xi}{k}\mathrm{dk}\right)^2\left(\int \mathrm{E}_\xi \mathrm{k}^2\mathrm{dk}\right)}{\left(\int E_\xi \mathrm{dk}\right)^3} \tag{62a}$$

$$Re_\tau = \left(\frac{L}{\lambda}\right)_w^2 = \frac{\left(\int \frac{E_w}{k}\mathrm{dk}\right)^2\left(\int \mathrm{E}_\mathrm{w} \mathrm{k}^2\mathrm{dk}\right)}{\left(\int E_w \mathrm{dk}\right)^3} \tag{62b}$$

Here Re_τ is an effective ”turbulence” Reynolds number and Sc_τ is an effective "turbulence" Schmidt number.

$$Sc_\tau = \left(\frac{L}{\lambda}\right)_\xi^2 \left(\frac{\lambda}{L}\right)_w^2. \tag{63}$$

The definitions of Re_τ and $Re_\tau Sc_\tau$ here come from homogeneous isotropic turbulence (HIT) and describe the bandwidth of the respective spectra. This is a measure of the breadth of wavenumber space accessed. Sc_τ here becomes a measure of the difference in bandwidth between the scalar spectrum and the kinetic spectrum. In HIT, where a statistical equilibrium

is reached, the material Schmidt number would determine the behaviour of the scalar spectrum compared with the kinetic energy spectrum. In the present case, the system cannot be said to be at statistical equilibrium, thus the material Schmidt number does not necessarily prescribe how the scalar spectrum behaves. Therefore the instantaneous effective turbulent Schmidt number Sc_τ is used here in place of the material Schmidt number.

2.7 Previous Results

Wong *et al*. [59] performed an analysis of second order moments and their budget equations after shock and reshock from a simulation of a $M_s = 1.45$ shock in air and SF_6 with an Atwood number of $At = 0.68$. Their focus was on the application of LES simulations on development and validation of RANS models.

Ristorcelli and Clark [40] derived self-similar transport equations of the form of Eqs.(5-7) but did not perform the change of variables to show that $\ln h^+$ becomes a measure of time in self-similar coordinates. In their work, they laid out the time evolution of centerline values for a number of spanwise averaged fields, such as the variance, skewness and kurtosis and Taylor scales as well as deriving predictions of self-similar evolutions of length scales. The prediction of inverse bandwidth, here defined as $\frac{\lambda}{L}$, was shown to scale as $h^{+-\frac{3}{4}}$. Skewness and kurtosis of both the scalar field and the streamwise velocity field were shown to collapse to a function of the scaled streamwise coordinate. This collapse of higher order moments in mixing flows was investigated by Schopflocher and Sullivan [44] who proposed a probability density function (PDF)-based model to account for this behaviour and the observed quadratic relationship between the skewness and kurtosis of the scalar field.

Schilling *et al*. [42] performed simulations of reshock of a two-dimensional single mode interface and investigated the resulting power spectrum evolution. Regions of $-\frac{5}{3}$ scaling at

small wavenumbers and -3 scaling at larger wavenumbers were identified in the kinetic energy spectrum, with only a small region of $-\frac{5}{3}$ scaling identified for the density spectrum at smaller wavenumbers and no scaling highlighted for larger wavenumbers.

Reese *et al*. [36] and Weber *et al*. [57] performed measurements of the RMI post-shock and observed similar small regions of $-\frac{5}{3}$ scaling for the scalar power spectrum.

Vorbieff *et al*. [52, 53] explored the evolution of the second order structure functions for a shock-gas cylinder interaction and a shock-gas curtain interaction respectively. The late time velocity structure function for the cylinder case shows a $\frac{2}{3}$ slope indicative of Kolmogorov scaling pointing toward the existence of an inertial subrange. For the second order scalar structure function for the gas curtain case, the time evolution of the second order exponent is shown to trend toward KOC scaling but level out at a value above the KOC scaling of $\frac{2}{3}$.

Ranjan's group at the Georgia Institute of Technology have performed high spatial resolution, low time resolution, simultaneous PIV and PLIF measurements of the RMI after reshock [25, 26] as well as high speed simultaneous PIV and PLIF measurements [3]. Single-shot experiments were analysed with a range of integral measures such as mixing width, mixedness and mixed mass, with the commonly found behaviours of linear growth of thickness after reshock and of the tending to a constant of the mixedness. Also presented were the evolution of some spectral quantities such as the kinetic energy spectrum which showed regions of Kolmogorov scaling, whereas no such region in the density power spectrum was evident. The second order structure function for streamwise velocity was also presented and shown to have a $\frac{2}{3}$ scaling while the second order density structure function did not have a KOC scaling region. The high-speed study was able to show qualitative agreement between the extracted velocity data and the evolution of the scalar field with vortical structures aligning well with bulk structure evolution and was one of the first such studies to show the viability of such

measurements.

Chapter 3

Experiment

3.1 The Shock Tube

Experiments are conducted in a 9.2 m long vertical, downward-firing shock tube with a square internal cross-section (25.4 cm sides) described by Anderson *et al*. [1]. To prepare for a run, the driver section is filled with nitrogen to ~80% of the rupture pressure of a 16 gauge steel diaphragm. This diaphragm sits on a set of steel blades in the shape of a cross that cause the rupture to occur along the edges of the blades. When the rupture occurs, the diaphragm is split into four petals that are bent down against the sides of the diaphragm section at high velocity. In preparation for a run, the driven section is pumped down to a vacuum pressure of 6.9 kPa, then a stagnation plane is formed by flowing a helium-acetone mixture downward from just below the diaphragm (point A in Fig. 1) and flowing argon upward from just above the end wall of the shock tube (point B in Fig. 1). While the stagnation plane is being formed, the vacuum system is closed to allow the tube to approach the desired pressure as quickly as possible to minimise contamination by air leaking into the system.

Once the stagnation plane is formed and the pressure in the tube is at about 7 kPa above atmospheric pressure, the vacuum system is turned on and a shear layer is created by flowing gas through the assembly shown in Fig. 2. A planar jet of argon is injected slightly above the stagnation plane, and a planar jet of the helium-acetone mixture is injected slightly below the stagnation plane. The resulting gravitationally unstable shear flow develops Kelvin-Helmholtz

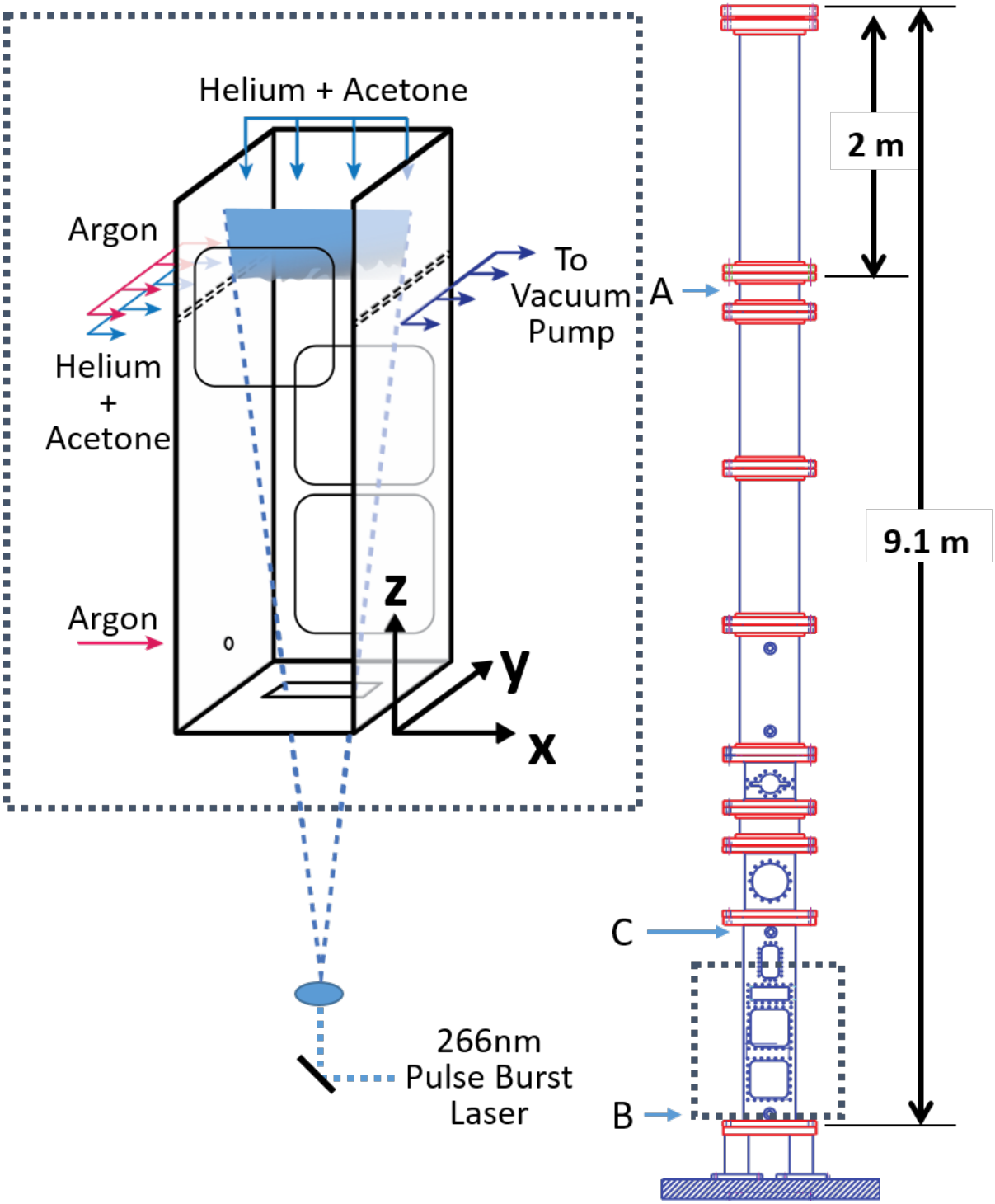

Figure 1: Diagram of the Wisconsin shock tube and an enlarged view of the test section.

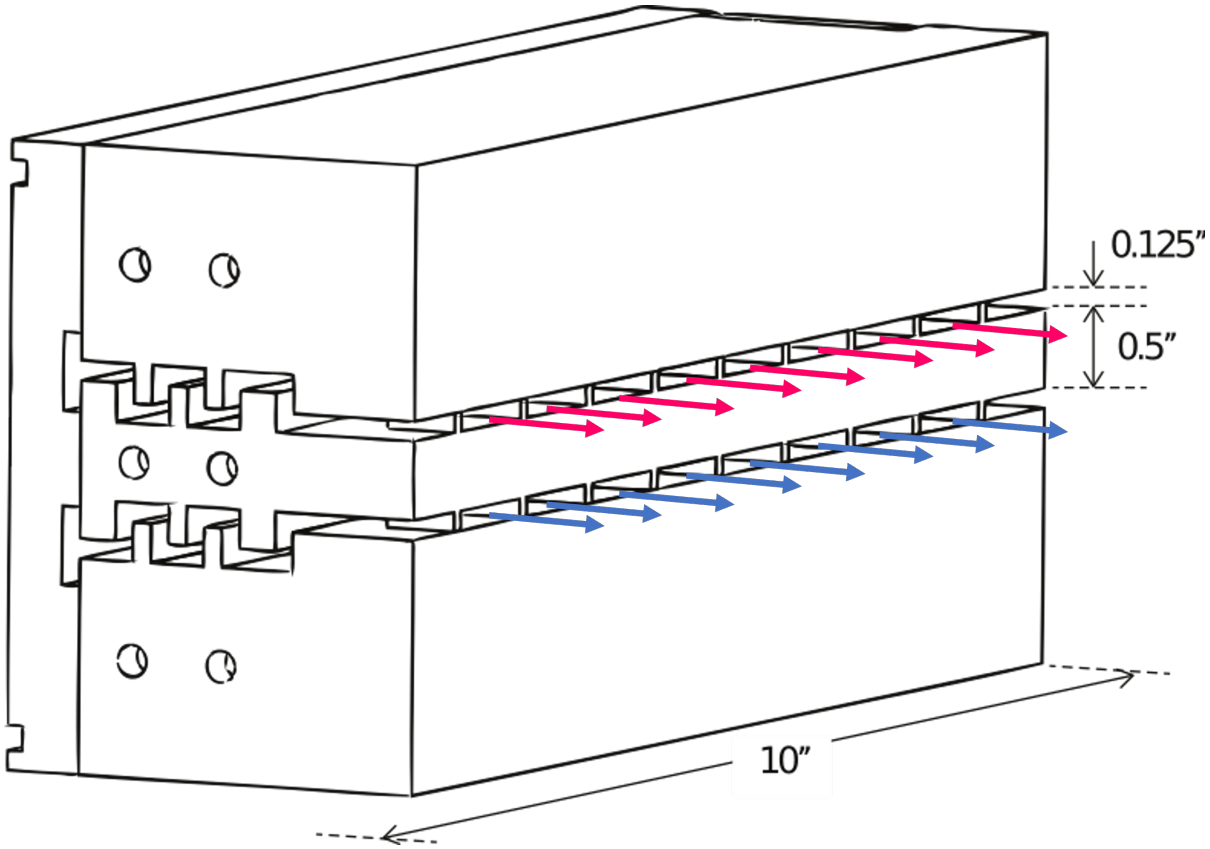

Figure 2: Schematic of the slots used to create the initial condition, taken from Ref [54].

structures that provide the diffuse multimode perturbations that constitute our initial condition. The pressure inside the tube is now at a steady state with excess gas being extracted at the interface by the vacuum system. This steady state is allowed to persist for 15 minutes to allow any air initially mixed in with the desired gases to be removed from the system.

3.1.1 Changing The Shock Tube Configuration

Previous experiments conducted in the Wisconsin shock tube by Weber [57] and Reese [36] were performed using configuration (a) in Fig. 3. This configuration was not viable for reshock studies since the interface did not enter into any of the viewing windows after reshock.

Two subsequent configurations were explored using a 1D gas dynamics code developed by Oakley [30]. Configuration (b) removed the bottom section of the tube such that a window was now available at the bottom of the shock tube. As can be seen from Fig. 3(b) this does not solve the issue as the interface now only enters a viewing window after reshock after it has interacted with multiple waves.

Configuration (c) in Fig. 3 was finally chosen where the main test section is now immediately above the end wall. This configuration provides an extended period after reshock when the interface is within the bottom window and remains stationary. This is useful to allow high-speed imaging in a single window.

3.1.2 Mach Number and Composition Estimation

Along the length of the tube are 12 piezoelectric pressure transducers (PTs) connected to a National Instruments data acquisition system. This set of PTs records the pressure wave pattern for a given experiment. One of the PTs is positioned (point C in Fig. 1) directly above the level of the initial condition. The signal generated by the passage of the incident shock past this PT

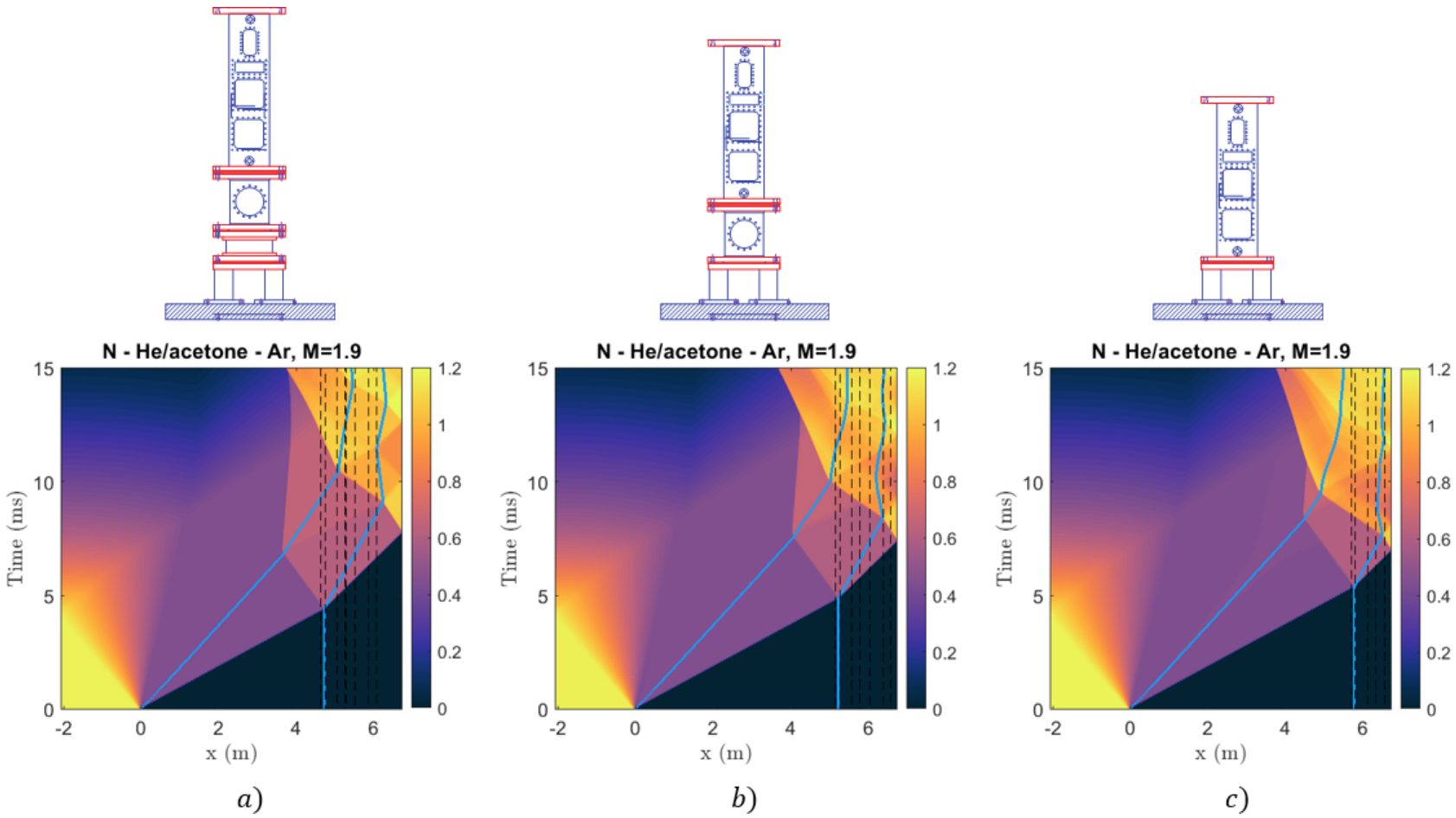

Figure 3: Contour plots of $\log_{10}(\frac{p}{p_0})$ for 3 configurations that were explored. Configuration c) was chosen for its extended period where the interface is approximately stationary in the bottom window. The blue lines represent material interfaces. The dashed black lines represent limits of the windows.

is used as the trigger for all subsequent experimental operations.

The recorded PT data is used to generate a $z - t$ diagram, such as in Fig. 4, that tracks the position of the incident shock, the transmitted shock and the reflected shock. This $z - t$ diagram allows the extraction of the speed of each wave. 1D gas dynamics (GD) can then be used, with these wave speeds as an input, to estimate the composition of the light gas (allowing for the presence of air and the run-to-run variation of acetone concentration), shock strength and relevant bulk gas temperatures, pressures and densities.

Using the predicted composition and initial shock strengths, these predictions can be further tested with a 1D shock tube simulation that generates a pressure, temperature and mole fraction field which can then be compared to the interface location determined from PLIF measurements.

The plot in Fig. 4 shows a composite of three $z-t$ diagrams. The teal line depicts the 1D GD estimate of interface location from PT data, the red line shows the interface location predicted by 1D GD finite volume simulation while the pink line is the measured interface location from HS PLIF. The discrepancy between the red and pink lines at later times is likely due to the mixing width growth of the interface being large in this particular experiment such that some of the interface is out of the field of view meaning that the estimate of the interface centroid may not be accurate. The black contour lines highlight wave interactions with the thick black lines showing shock trajectories. The results of the 1D simulation are overlaid on-top of the locations measured with the PTs showing agreement between measured and predicted shock and interface locations. This offers encouragement that the 1D GD predictions of composition are accurate.

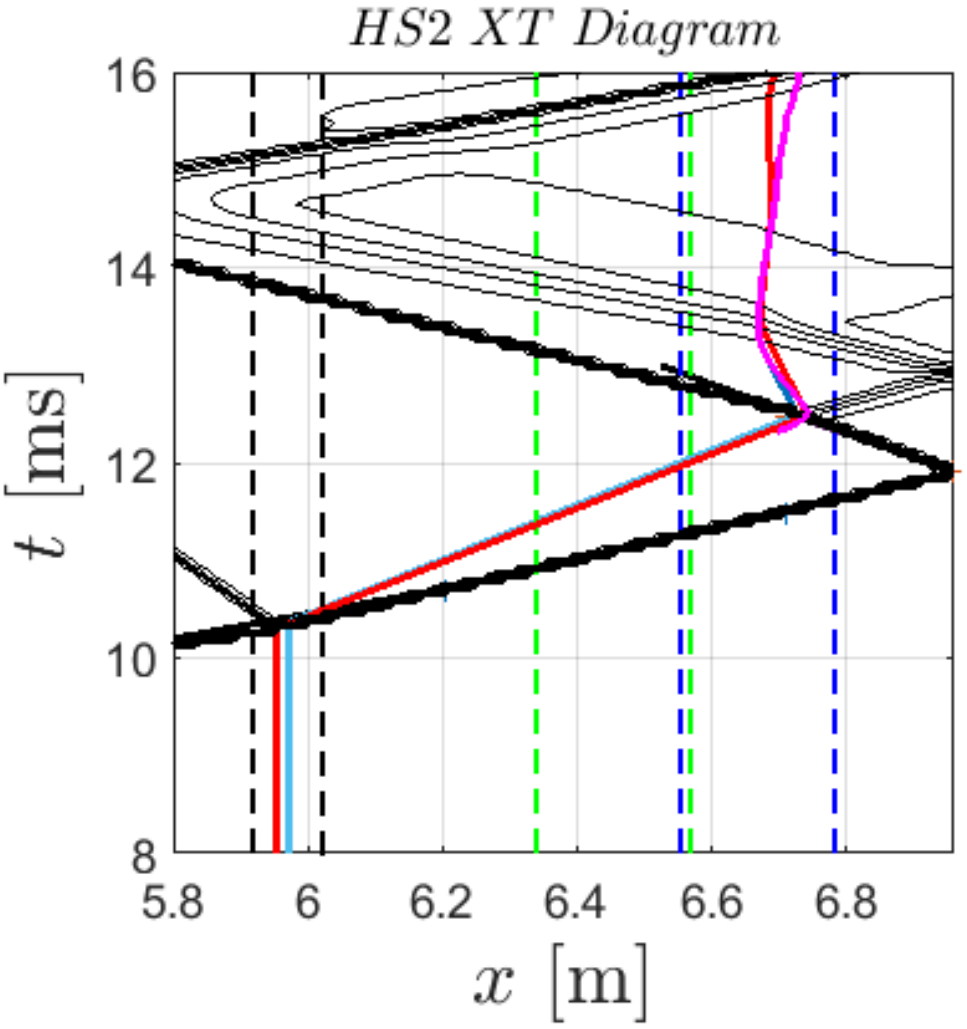

Figure 4: Example combined $z - t$ diagram. Blue solid line - interface location from 1D GD, red solid line - interface location from 1D finite-volume simulation, pink solid line - interface location from PLIF measurements, dashed lines - observation windows.

3.1.3 Choosing Gas Composition For High Mach Number Experiments

To attempt a change in Mach number with the current shock tube configuration required an exploration of the controllable parameter space, which was the acetone mole fraction and the argon mole fraction in the helium mixture. This determined the feasibility of the interface residing in the field of view for a reasonable duration, and residing close to the center of the window so a minimal amount of the interface would be cut off as the interface thickness grew. A design of experiment (DOE) study was performed using an in-house 1D gas dynamics finite volume code. This produced a measure of the residence time of the interface in the window of interest and a measure of the mean location of the interface within the window. Optimal interface evolution was provided by a 97% helium and 3% acetone mixture by mole fraction.

3.2 PIV

For SS experiments, single image pairs were acquired for each experiment. For these, particle image velocimetry (PIV) is performed using TSI Inc's Insight 4G program following the procedure described by Reese *et al*. [37].

For HSS experiments, 90-150 actionable frames of particle images are collected per experiment. To enable the batch processing of videos within MATLAB, the PIVLab plugin [45] was used.

As described by Scharnowski and Kähler[41] the optimal range of particle radii for PIV is between 1 px and 1.5 px. The lower bound avoids the effects of peak locking and the upper bound reduces the effect of random uncertainties on identifying a correlation peak. Figure 5 shows a representative distribution of particle sizes for SS (left) and HSS (right) experiments showing the mean of the distribution for both campaigns lies in the recommended range.

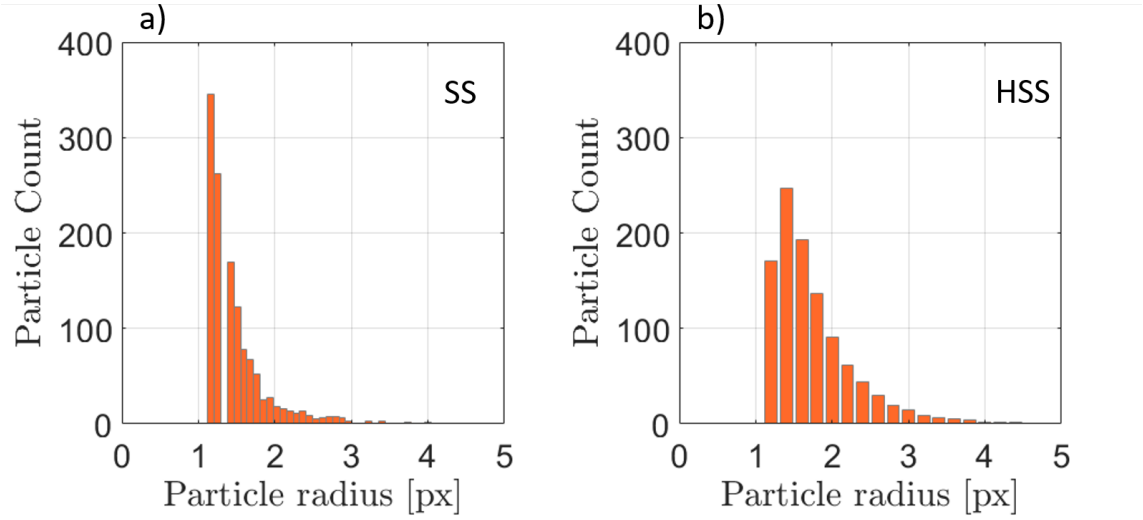

Figure 5: Particle radius distribution from SS and HSS experiments

These distributions were calculated using a distance transform watershed method on a subset of background-subtracted particle images from each campaign.

3.3 PLIF

3.3.1 Acetone Modelling

Moving to reshock conditions, which have higher temperatures and pressures, affects the photophysical and chemical properties of acetone. Estimates of the expected effect on signal to noise ratio (SNR) and on acetone decomposition needed to be made.

To estimate the amount of acetone decomposition, the MATLAB interface to the Cantera software package [12] was used along with the, detailed n-heptane mechanism developed at Lawrence Livermore National Laboratory (LLNL) [23] that contains acetone as one of its species. A steady approximation was made using a constant pressure reactor module as a model for the expected environment, and the initial properties of the reactor were set to the conditions

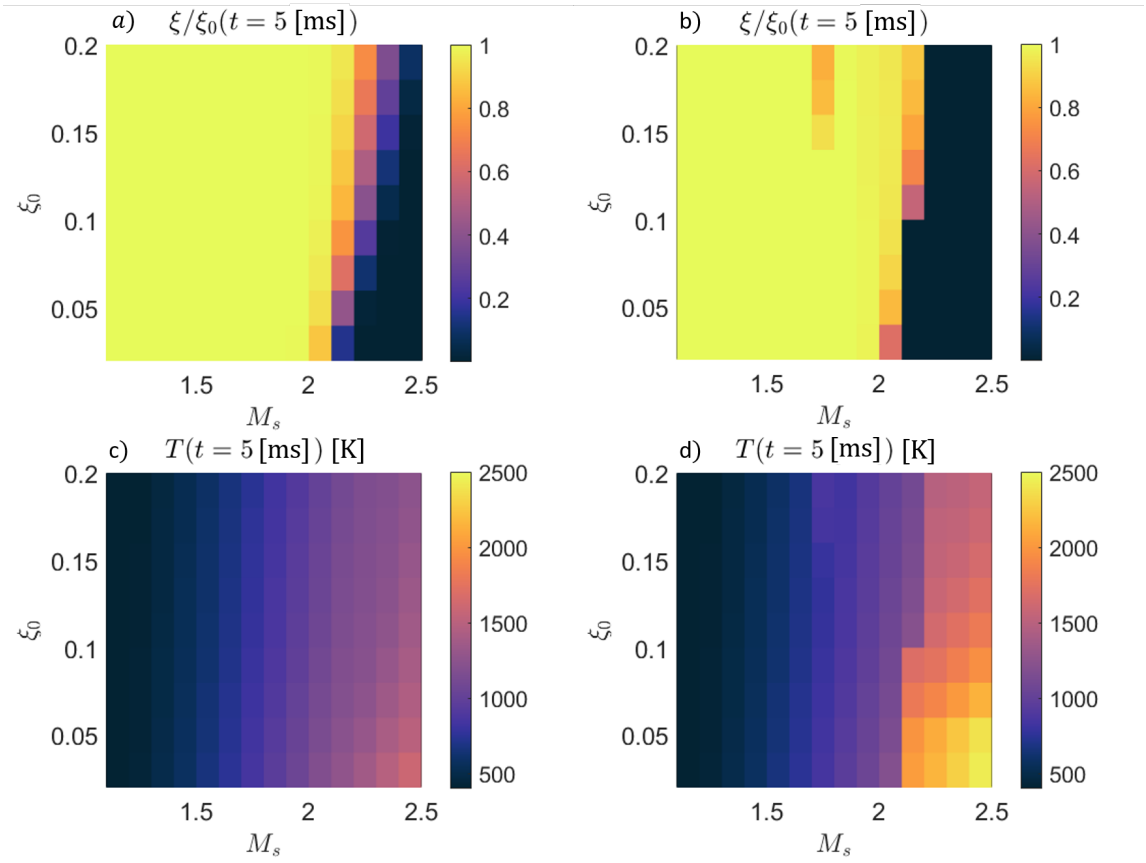

Figure 6: Acetone decomposition after 5 ms. a) and c) 5% acetone mole fraction and argon mix; b) and d) 5% Acetone mole fraction, argon and 5% air mix.

derived from 1D GD for a given Mach number and acetone concentration.

The results of these calculations for a range of initial shock strengths, M, can be seen in Fig. (6). The pre-shock acetone mole-fraction is taken to be 5%. The plot shows that for the Mach number ($M_s = 1.8$) used in the current experiments, even after reshock, only negligible amounts of decomposition are expected.

With confidence that the observed signal will be acetone fluorescence, now an attempt is made to estimate the expected signal to noise ratio (SNR). Figure 7 shows plots of SNR generated using the excitation model of Thurber *et al*. [47], assuming an acetone mole fraction

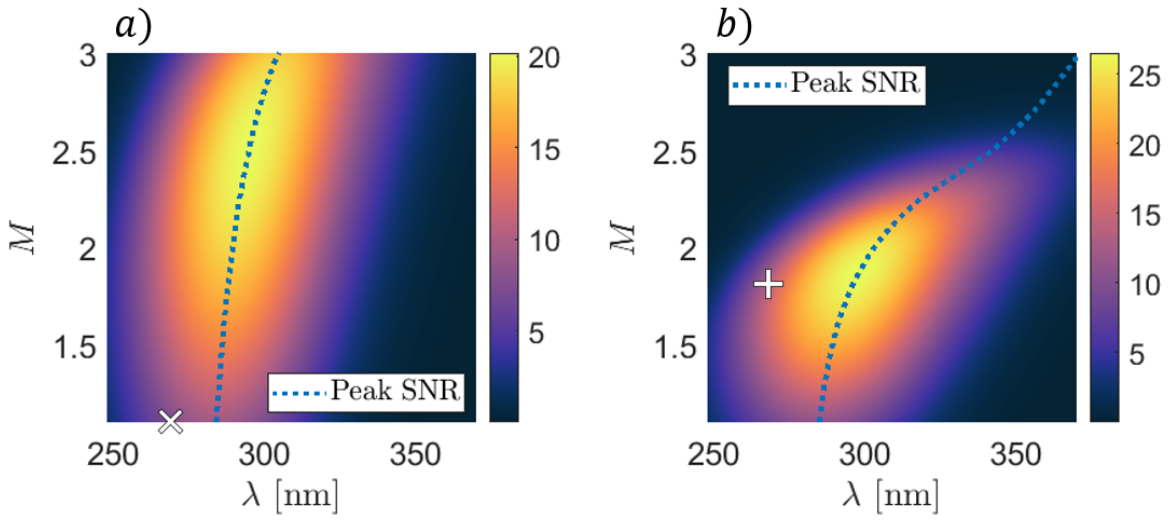

Figure 7: Predicted signal to noise ratio (SNR) for 3% acetone concentration, 30 mJ/pulse laser energy and using the Phantom V1210 camera. SNR is plotted as a function of Mach number M and laser wavelength λ for a) shock and b) reshock conditions. The white cross in a) denotes the conditions of the PLIF jet test experiments (Sec. 3.8.1), the white plus in b) denotes the experiment parameters for the HS and HSS experiments.

$\xi_{acetone} = 0.03$ and a laser energy of 30 mJ/pulse. The left plot in Fig. 7 is a contour plot of SNR in post-shock conditions for a given shock strength M and laser excitation wavelength λ. The right plot is a similar contour plot of SNR but for post-reshock conditions. The SNR plot on the right of Fig. 7 provides some confidence that reshock experiments at $M = 1.8$ using a wavelength of $\lambda = 266$nm with an acetone concentration of 3% will provide actionable PLIF data.

3.3.2 Iterative PLIF correction

Figure 8 shows a block diagram representation of the algorithm developed by Herzog [13] that is used to iteratively correct the raw signal PLIF images and extract mole fraction fields.

The inputs to the algorithm are the acquired PLIF signal and the pressure and temperature derived from 1D GD. Assuming constant photo-physical properties, then purely from the PLIF image, an initial estimate of the number density of acetone can be calculated:

$$\frac{N_{init}}{N_0} = \frac{S}{S_0}\left[1 + N_0\sigma_0 \int_{r_0}^{r} \frac{S}{S_0} \mathrm{d}r'\right]^{-1} \tag{64}$$

where N is the particle number, σ is the absorption cross-section, r is the distance along a ray and S is the signal. The product $N_0\sigma_0$ can be estimated directly from the PLIF image as long as a region of uniform acetone concentration can be identified, then, using Beers law, an exponential can be fitted to the signal decay in this region. This estimate of number density can then be used to estimate the temperature field:

$$T = \frac{\sum_{i=1}^{m} Y_i c_{pi} T_i}{\sum_{i=1}^{m} Y_i c_{pi}} \tag{65}$$

with Y_i being the mass fraction of species i, and c_{pi} being the mass-specific heat capacity

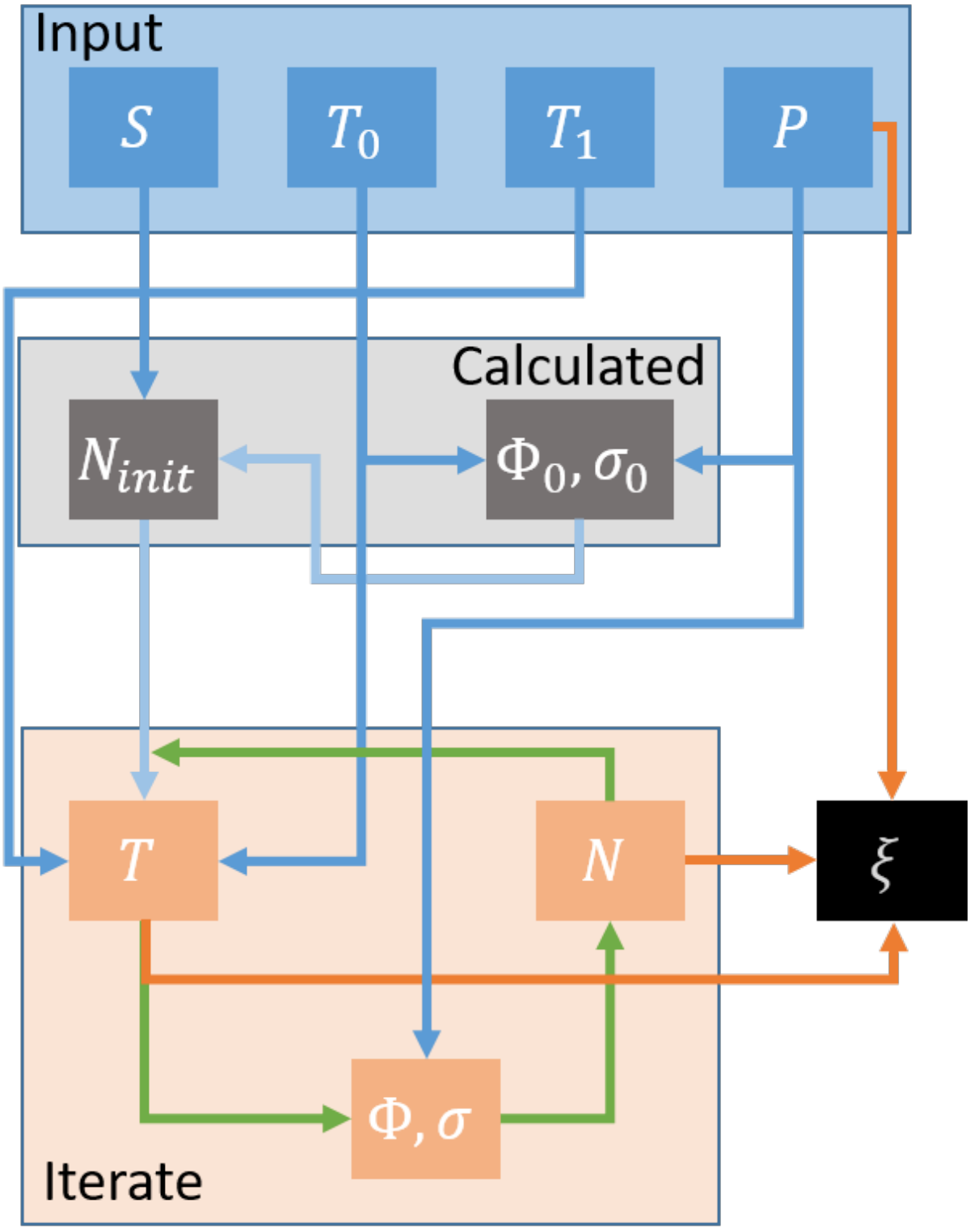

Figure 8: Diagrammatic representation of iterative PLIF correction algorithm.

of species i. This temperature field can then be used with a model by Thurber [47] to calculate fluorescence quantum yield Φ and with a curve fit by Koch [17] to calculate absorption cross section σ. The updated photo-physical parameters now allow the use of the full number density calculation:

$$\frac{N}{N_0} = \frac{\Phi_0 S}{\Phi S_0}\frac{\sigma_0}{\sigma}\left[1 + N_0\sigma_0\int_{r_0}^{r}\frac{\Phi_0 S}{\Phi S_0}\mathrm{d}r'\right]^{-1} \tag{66}$$

This procedure of calculating an updated temperature field to calculate Φ and σ to then calculate an updated N/N_0 is repeated until the change between iterations is below a given threshold. Typically 10 iterations provide good convergence. The acetone mole fraction ratio, and then the light gas mole fraction ξ, can then be found by:

$$\xi = \frac{\xi_{acetone}}{\xi_0} = \frac{N}{N_0}\frac{T}{T_0} \tag{67}$$

3.4 Image registration

Image registration to align coordinate systems of PLIF and PIV results is required to allow the analysis of terms that involve both density and velocity components. The process used is described by Reese *et al*. [37].

Figure 9 shows the initial step of manually choosing control points (CPs) (3 are shown for example, but 12 are used in practice) in the target image captured by both cameras in the HSS campaign. The procedure for SS data is the same. The CPs in the Phantom image is chosen as the moving points while the Photron CPs are the fixed points. These manually selected CPs are then tweaked with a correlation step that attempts to match structures in each image. These CPs are then used to estimate the required geometric transformation matrix that can be applied

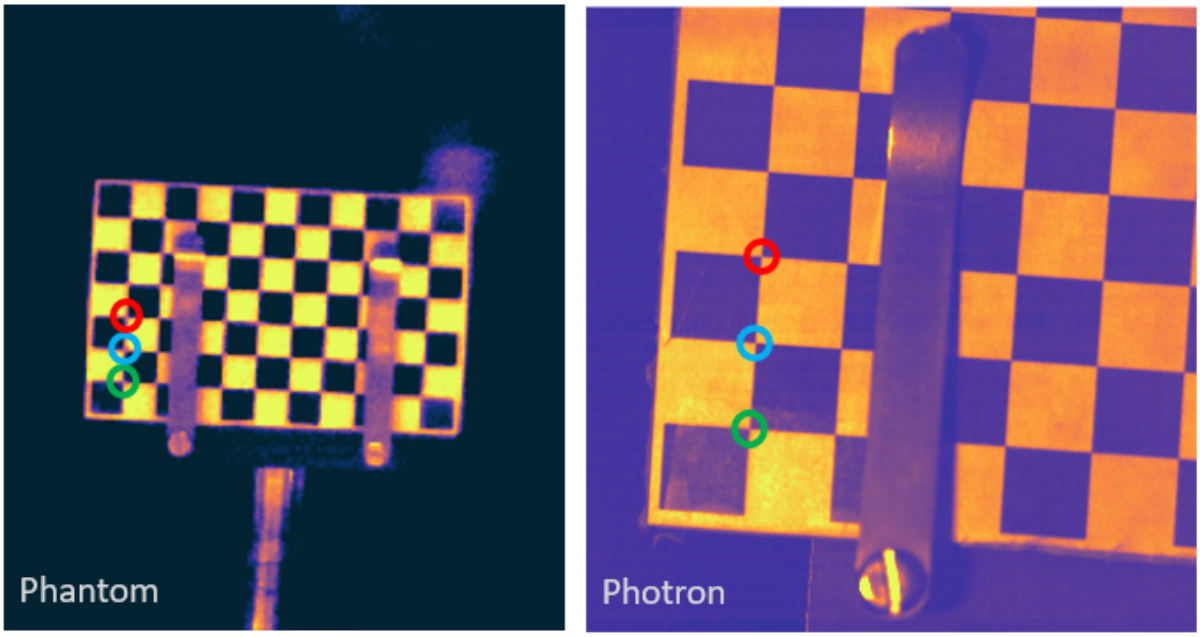

Figure 9: Left: Phantom camera target image. Right: Photron camera target. Coloured circles are example control points.

to translate, scale and rotate the moving frame into the fixed CPs' coordinate system.

3.5 Material transport calculations

For each experiment we are able to calculate bulk temperatures and pressures from 1D gas dynamics calculations using the pressure transducers located along the length of the shock tube.

To achieve an accurate estimate of the terms in Eq.(32a) the material transport properties ν (momentum diffusivity) and $\mathcal{D}$ (mass diffusivity) need to be calculated, not just as single values, but as fields. Here the methods and parameters given in Appendix A of [49] are used to calculate the required terms in Eq.(32a).

Figure 10 shows the resulting values of these fields taken at the $\xi = 0.5$ level as a function

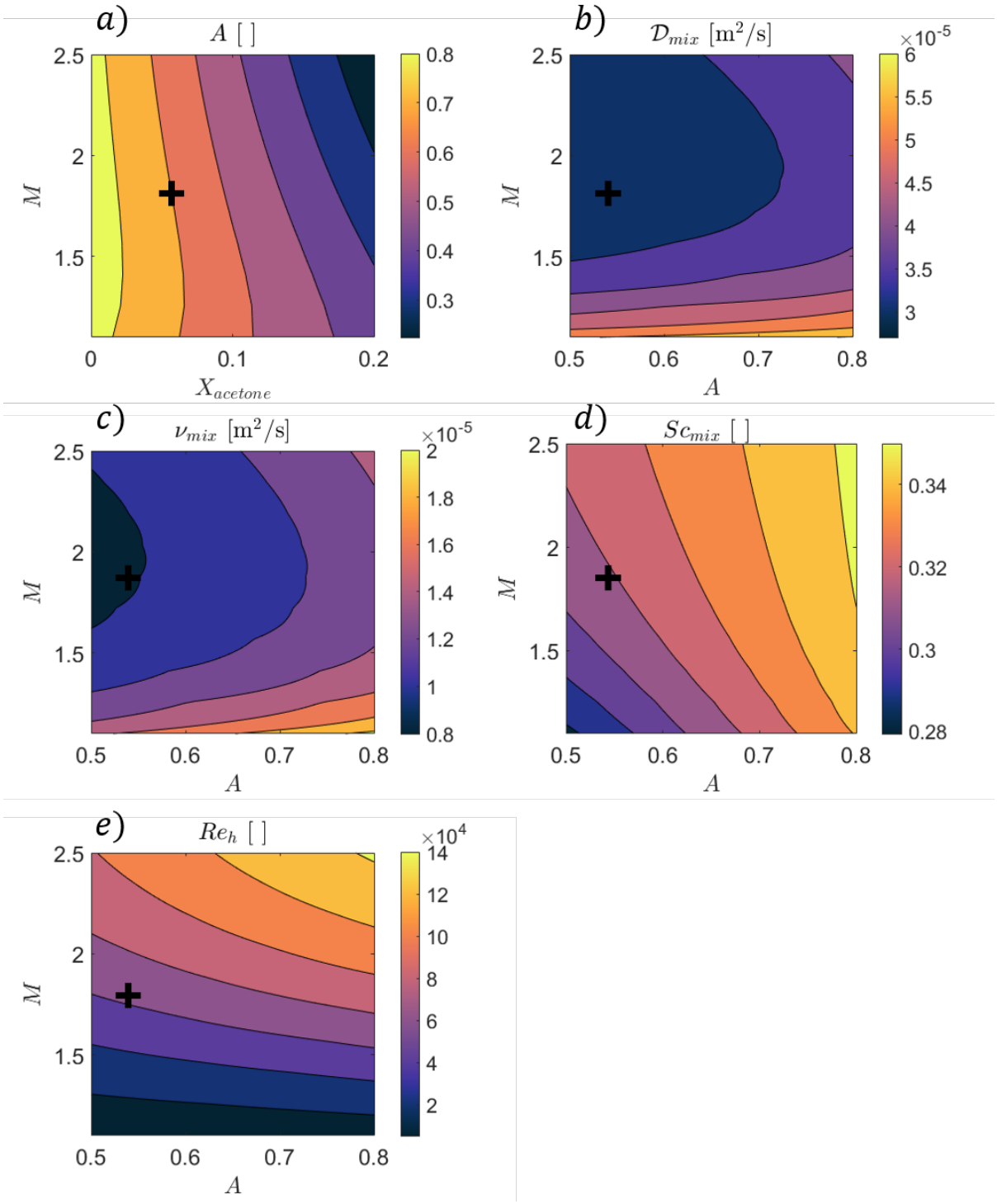

Figure 10: Material transport calculations. the '+' symbols indicate the experiment conditions.

of Mach number and Atwood number. These are shown to demonstrate the variation in the parameter space and to highlight the representative values seen in these experiments. Figure 10e) shows an estimate of the initial re-shock Reynolds number $Re_h = \frac{h_0 \dot{h}_0}{\nu}$. This is estimated using the calculated Atwood number and viscosity and the Mikaelian re-shock growth rate estimate $\frac{\dot{h}_0}{\Delta V_0} = C_m A$ with $C_m = 0.23$. The representative values, shown here, and specifically the value at the conditions explored in the present work (denoted by the bold cross), are above the Reynolds number proposed by Dimotakis [7] as the limit above which transition to turbulence can be expected.

3.6 Initial Condition

The IC utilized here was developed and analyzed by Weber [54]. Once the gas composition was set by design of the experiment to allow imaging at high speed for an extended time, the IC had two parameters to vary to control the IC seen by the initial shock wave.

These two parameters are the relative flow rates of the two gas streams. These can be manipulated into two dimensionless parameters, the Froude number $Fr = \frac{u_m}{\sqrt{gL}}$ describing the competition between the shear of the total jet of fluid and gravity, and the injection anisotropy $\beta = \frac{u_2 - u_1}{u_2 + u_1}$ encapsulating the difference between the two individual flow rates. Here u_1 is the flow velocity of the bottom helium/acetone mixture and u_2 is the velocity of the top argon jet. u_m then is the average of the two velocities.

A subset of this two parameter space was explored and the results are plotted in Fig. 11. Low Froude number and zero anisotropy lead to a diffuse interface but very long wavelength perturbations, a moderate increase in Fr and then a non-zero β however leads to interesting multimode diffuse perturbations. Increasing Fr too much with a negative β then lead to a more diffuse and long wavelength perturbations. A sweet-spot was chosen with a moderate Fr of 0.6

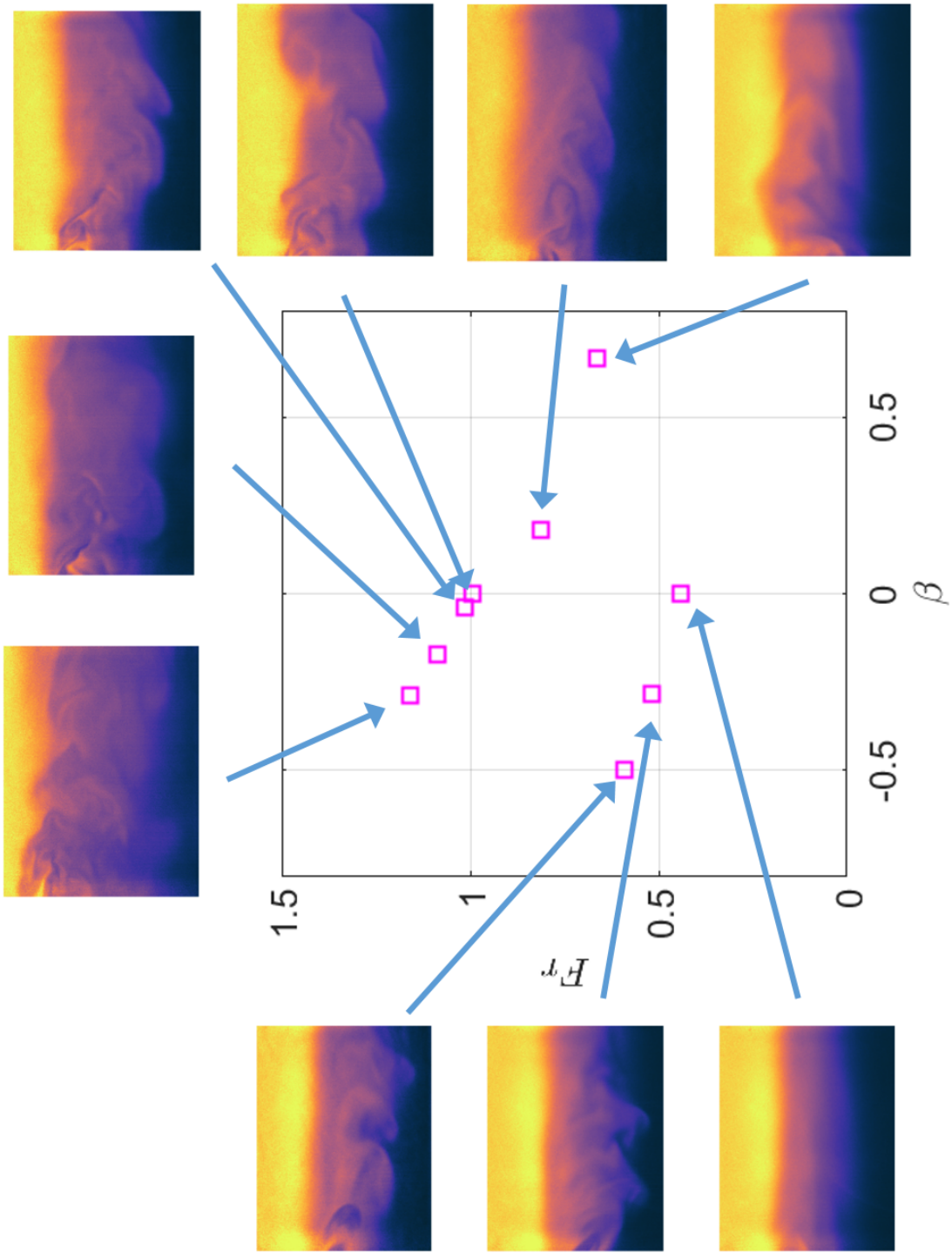

Figure 11: IC parameter space and corresponding representative concentration fields.

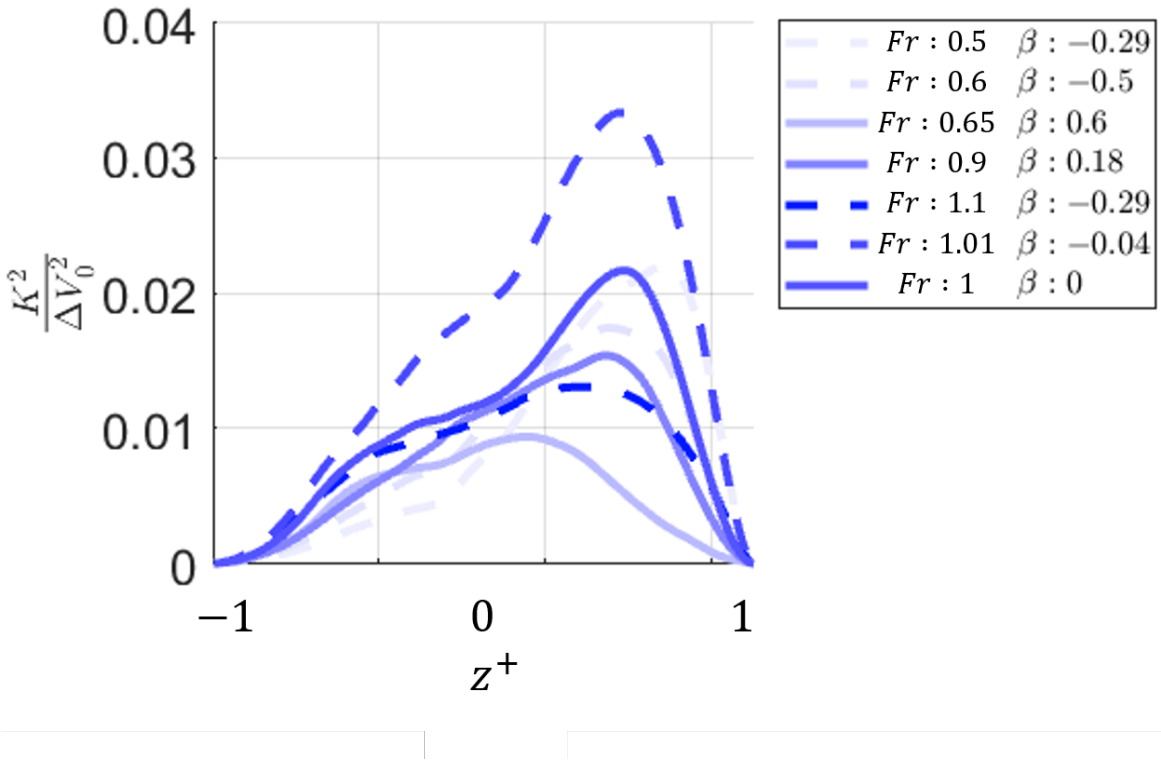

Figure 12: Measured normalized kinetic energy $K = \overline{\sqrt{\rho}w}^2$

and a negative β of -0.5.

One of the parameters of interest once the IC conditions are set is its potential effects on the development of the RM instability. Figure 12 plots the specific fluctuating kinetic energy, normalized by the bulk interface velocity jump due to the shock. For the parameters chosen, the peak energy is about 2% of the potential deposited kinetic energy.

3.7 Single Shot Experiments

A set of single-shot experiments were conducted in the WiSTL shock tube using PLIF and PIV to measure the 2D concentration and velocity fields in a vertical cross section of the flow,

M_s	1.9±0.04
M_{rs}	1.7±0.01

	t_s [ms]	t_{rs} [ms]	Sym
IC	0	-	
PS3	2.16	-	
RS1	2.3	0.26	
RS2	3.07	1.14	
RS3	3.87	1.92	
RS4	4.7	2.75	

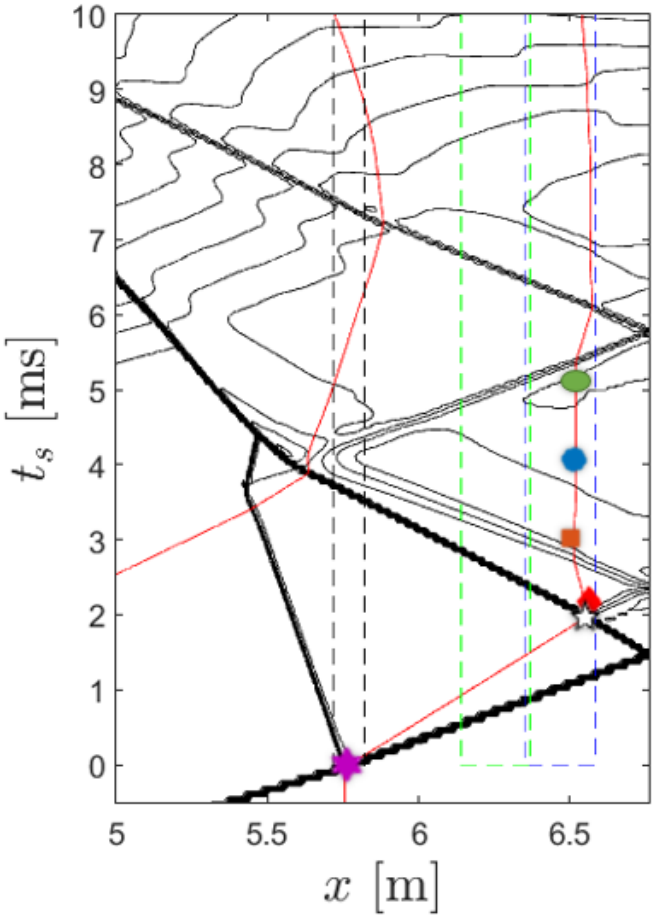

Figure 13: Parameters of single-shot experiments with space-time locations overlaid on a contour plot of $\log_{10}(\frac{P}{P_0})$. PS3 here refers to data collected by Reese *et al* [36]. The third time recorded by Reese acts as an initial condition to the present work after reshock.

respectively. An excimer laser produced a 308 nm beam that was used to excite acetone to fluoresce, while a dual head Nd:YAG system was used to generate 2 pulses of 532 nm separated by 20 μs. The beams were turned into diverging laser sheets, with a diverging angle of 30° and a waist of 0.7 mm. The PLIF image was timed such that the excimer laser was fired half way between the two Nd:YAG laser pulses. This provided three images per experiment run that consolidated into two measurements, one of concentration and one of two-component velocity. Twenty experiments were performed for each of the four post-reshock times shown in Fig. 13.

3.8 High-Speed PLIF Experiments

	M_s	A^+	A^{++}	Re_{h0}
HS1	1.88	0.320	0.323	$2.6\text{x}10^4$
HS2	1.89	0.320	0.326	$2.5\text{x}10^5$
HS3	1.93	0.268	0.266	$3.0\text{x}10^5$
HS4	1.94	0.253	0.247	$4.7\text{x}10^4$
HS5	1.96	0.230	0.221	$1.8\text{x}10^4$
HS6	1.90	0.306	0.312	$7.8\text{x}10^4$
HS7	1.99	0.191	0.170	$2.5\text{x}10^4$
HS8	1.95	0.244	0.236	$1.9\text{x}10^4$

Table 3: Parameters of high-speed experiments.

A series of eight high-speed experiments were performed using a pulse-burst laser system that delivered a pulse train of 10 ms duration at a repetition rate of 20 kHz. The system amplifies the output of an Nd:YVO_4 oscillator laser in two Nd:YAG amplification stages. The fourth harmonic at 266 nm is used in the experiments with an average total energy of 30 mJ per pulse. The resulting fluorescence signal was captured with a Phantom V1210 high-speed camera at 20,000 frames per second for a duration of 10 ms. An example of the resulting concentration fields can be seen in Fig. 14. The parameters of each of the 8 experiments are

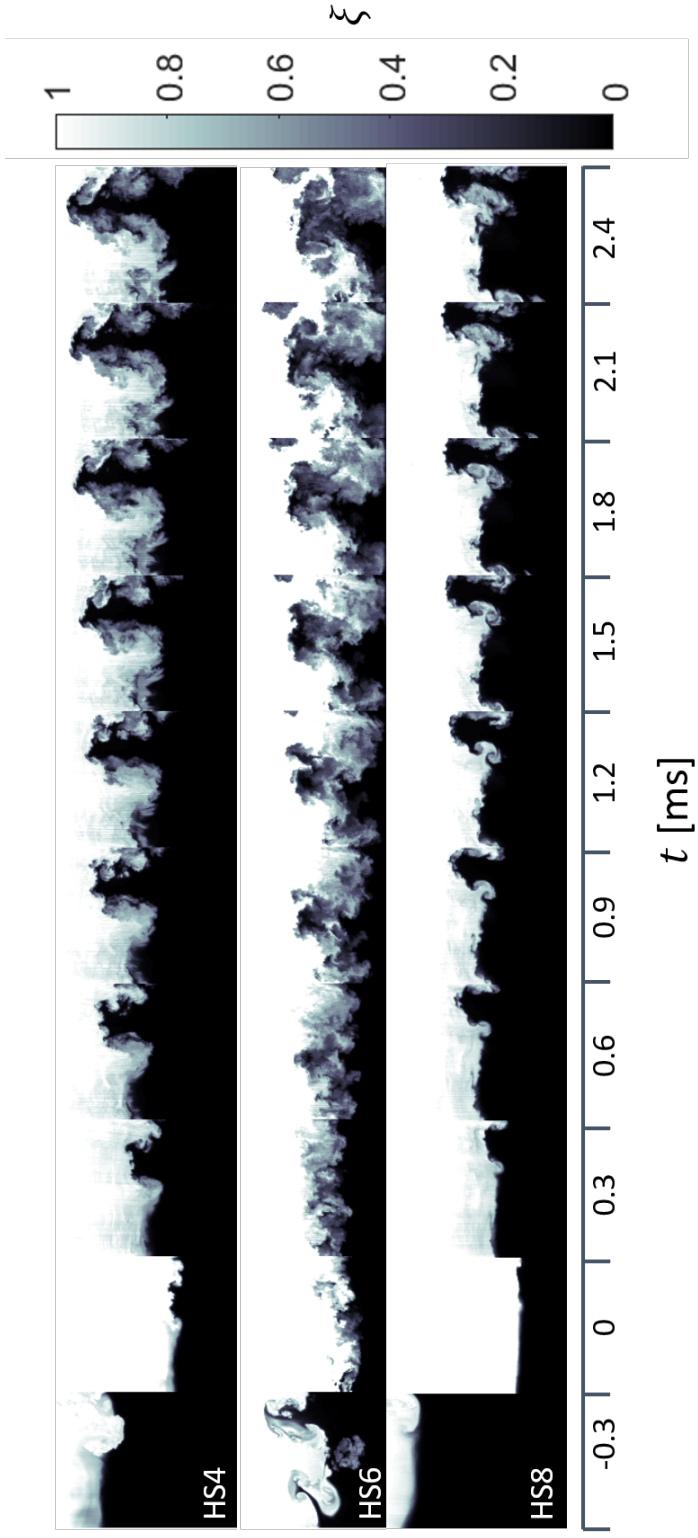

Figure 14: Example of interface evolution from HS data.

shown in Table 3.

3.8.1 The possibility of high-speed PLIF

With Professor Rothamer having engineered a high-speed laser system, it became a possibility to study the RMI in a time-resolved fashion. The system was designed to emit 266 and 532 nm wavelengths which, as Fig. 7 shows, is away from the peak SNR for the reshock conditions, but still delivers a useable SNR. To validate the SNR estimate, a set of experiments were conducted to prove the feasibility of performing high-speed PLIF at STP conditions. These consisted of PLIF imaging of a circular jet of a nitrogen-acetone mixture with 3% acetone.

Figure 15 shows the results of these experiments. The plot is of SNR taken in the exit region of the jet. The initial low SNR in the first 5 frames can be seen as an initial low energy per pulse. At frame 5 we see a strong signal but the beam profile is not uniform and as such the region measured has low signal. By frame 25 the beam profile becomes more uniform and reaches a peak energy and slowly decays. The average energy per pulse here was 24 mJ/pulse and the average SNR here matches well the value of the SNR at the point marked by a cross in Fig. 7. This result gave confidence that high-speed PLIF could be performed and it provided confidence that the model used to predict SNR provides accurate results.

3.8.2 Acetone seeding system

The run-to-run variation in Mach number and Atwood number in HS experiments was due to a hard to control acetone seeding system that relied on the pressure of the helium line feeding into the acetone bath to set the concentration of acetone. This pressure was liable to fluctuations if other valves and rotameters were not controlled precisely. A carefully controlled system was developed by Alex Ames (another graduate student) and deployed.

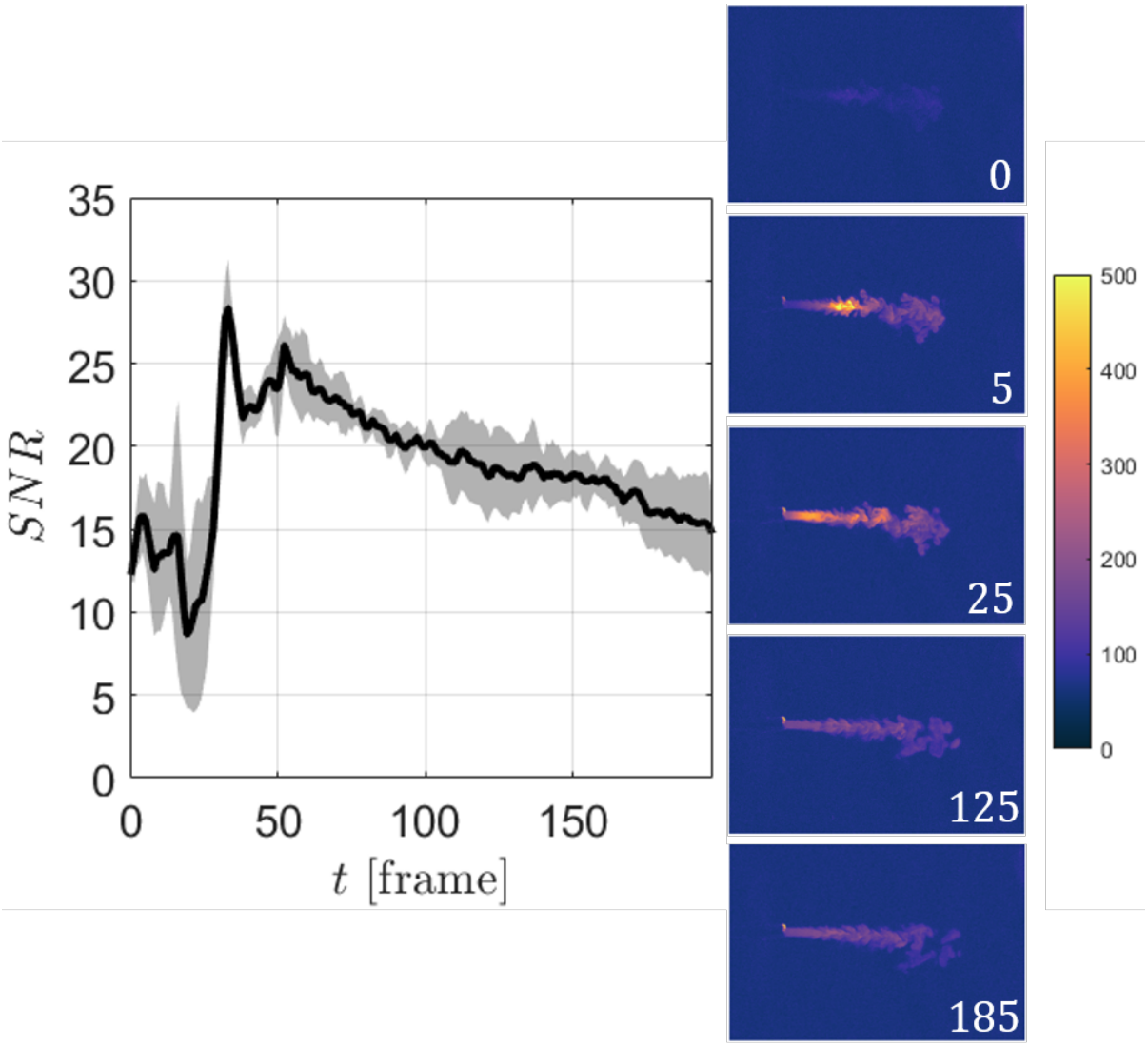

Figure 15: Signal-to-noise ratio as a function of frame number for a validation run using a nitrogen jet with 6% acetone. Images on the right show representative raw counts from the phantom V1211.

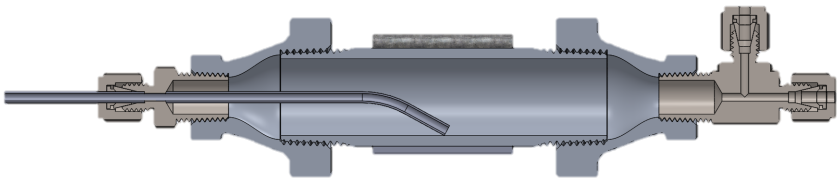

Figure 16: Updated acetone vaporizing seeding system

The new acetone injection system makes use of an Alicat mass flow controller and an Alicat liquid flow controller. These controllers allow a consistent and accurate setting of the flow rates of helium and acetone. The acetone is flowed through a vaporiser assembly, shown in Fig. 16, that is kept at a constant temperature. The acetone is then flowed into the helium line through a simple T-connection and allowed to mix.

Liquid acetone is pushed from a reservoir which is pressurized with helium, it passes through the Alicat liquid flow controller where the mass flow rate can be set. The liquid acetone comes into the vaporizer assembly from the left in Fig. 16. The liquid is deposited onto the interior surface of a sealed cylinder. This cylinder is wrapped with an electric heater and insulated and is kept above the boiling temperature of acetone such that the liquid acetone vaporizes as it flows onto the cylinder surface. The acetone vapor then exits the assembly to the right where it mixes with a stream of helium.

3.9 Simultaneous High-Speed PLIF and PIV Experiments

A set of 20 experiments were conducted in this campaign. The setup is similar to that described in Chapter 3.8. The same pulse-burst laser system was utilized, although in this campaign, instead of being blocked, excess 532 nm wavelength light from the frequency doubling process

is allowed to co-propagate so both 266 nm and 532 nm laser light is emitted. A set of four dual-coated turning prisms were used to direct the resulting beam path from the laser exit to the bottom window of the shock tube.

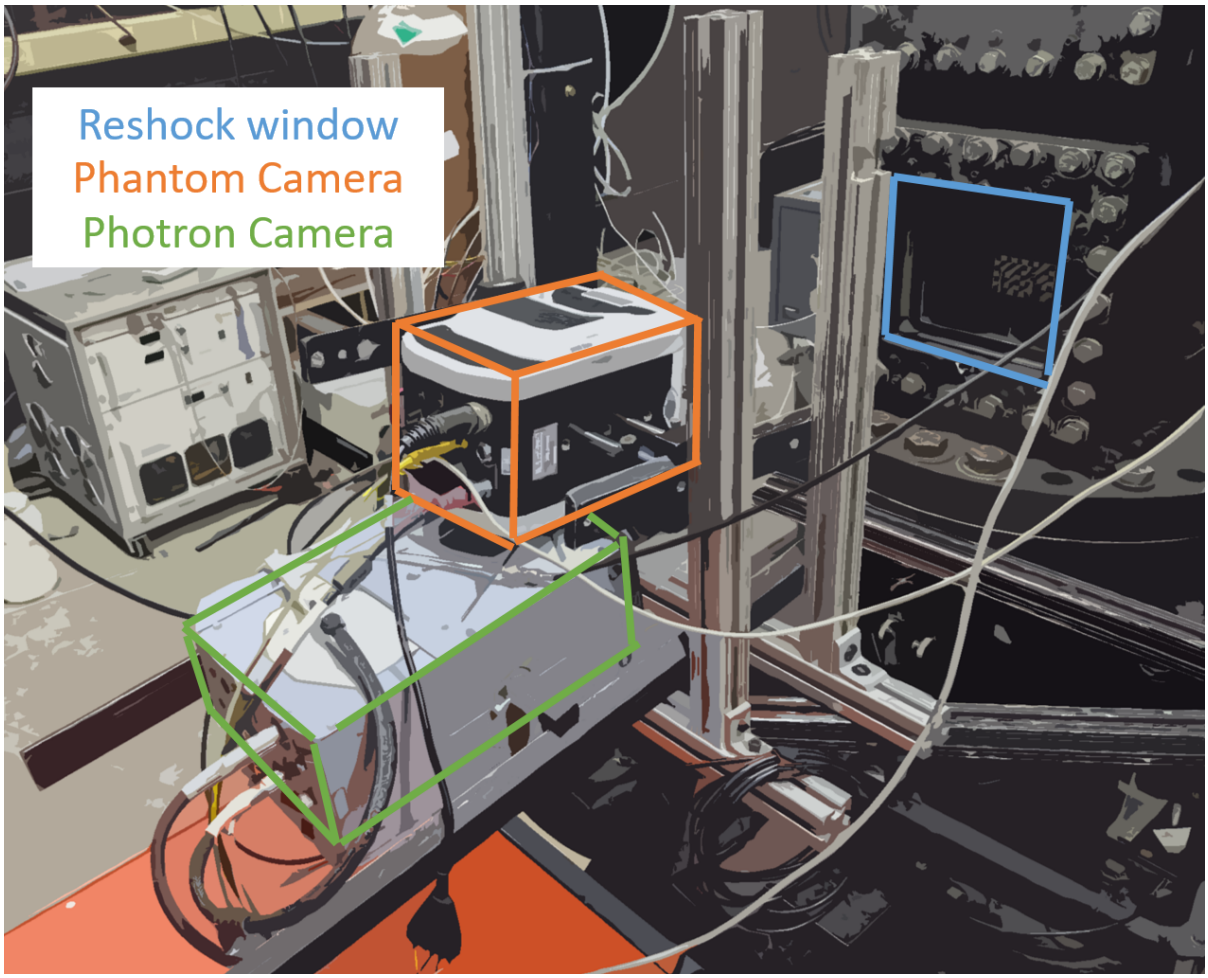

Figure 17: Camera setup for HSS experiments depicting the reshock window and the layout of the PIV (Photron) camera and the PLIF (Phantom) camera.

A Phantom V1210 was again used to capture the resulting fluorescence signal while a Photron Fastcam SA-Z high-speed camera was used to capture Mie-scattered light for PIV.

Figure 17 shows the physical layout of the two-camera rig in relation to the viewing window. Figure 18 shows the resulting FOVs for these two cameras where, similar to Petter *et al*.

[32], the PIV camera has sacrificed full-field imaging to capture well-resolved particle images.

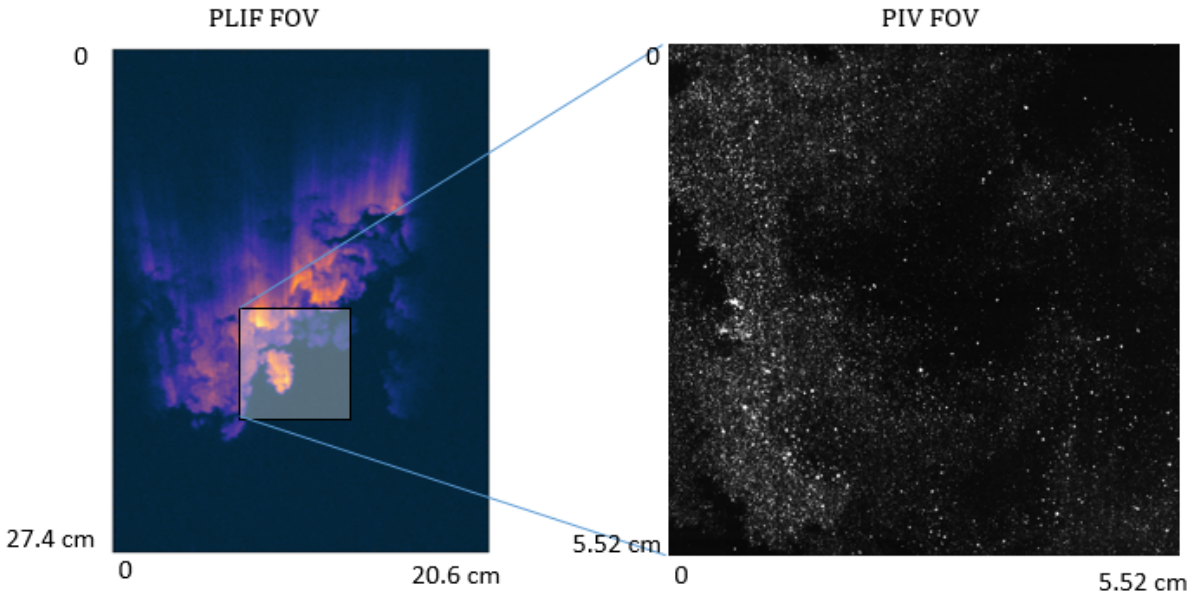

Figure 18: Field of view for the PLIF and PIV raw images for the HSS experiment campaign.

To summarize and compare the diagnostic details of all three experiment campaigns, Table 4 lays out important parameters for the SS, HS and HSS experiments.

	SS	HS	HSS
Spatial resolution Δx [mm]	0.22	0.245	0.43
Temporal resolution Δt [ms]	N/A	0.05	0.05
PLIF FOV [cm]	15 x 14	14 x 8	25 x 13
PIV FOV [cm]	15 x 14	N/A	5.5 x 5.5
PLIF laser wavelength [nm]/energy [mJ/pulse]	308/360	266/30	266/30
PIV laser wavelength [nm]/energy [mJ/pulse]	532/280	N/A	532/80
PLIF sensor size [px]	1024 x 1024	767 x 575	767 x 575
PIV sensor size [px]	6600 x 4400	N/A	1024 x 1024

Table 4: Details of diagnostics for SS, HS and HSS experiment campaigns.

Chapter 4

Experimental Results

The results from SS, HS and HSS experiments are presented here to complement one another and reconstruct the evolution of the reshocked mixing layer. SS experiments provide high SNR and concurrent measurements of concentration and velocity. HS data has a lower SNR and only provides measurements of the concentration field but allows the time evolution of a given experiment to be captured. HSS experiments still suffer from lower SNR, however they record the time evolution of both the concentration field and the velocity field to enable the exploration of transport and production terms in evolution equations. Figure 19 shows the normalised initial interface growth rate over the total parameter space explored over all experiments conducted in the three campaigns. Each point represents an individual experiment run. Figure 20 shows a set of representative fields from single shot experiments for each distinct time defined in the Table in Fig. 13. Figure 21 shows a set of ICs for three of the eight high-speed experiments that will be focused on, with HS 4 and 8 having qualitatively similar structure and HS6 visibly containing more scales. Figure 22 shows an example of the concentration, streamwise and spanwise velocity fields from HSS data.

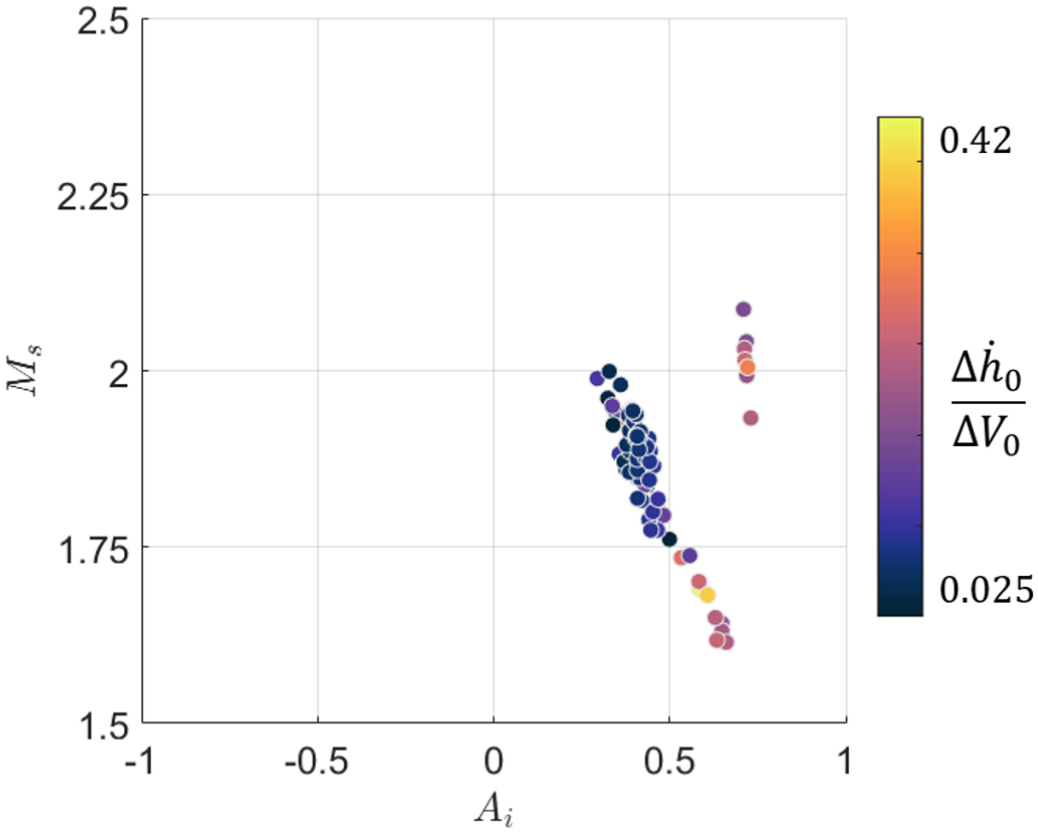

Figure 19: Experiment parameter space, coloured by initial normalised interface growth rate.

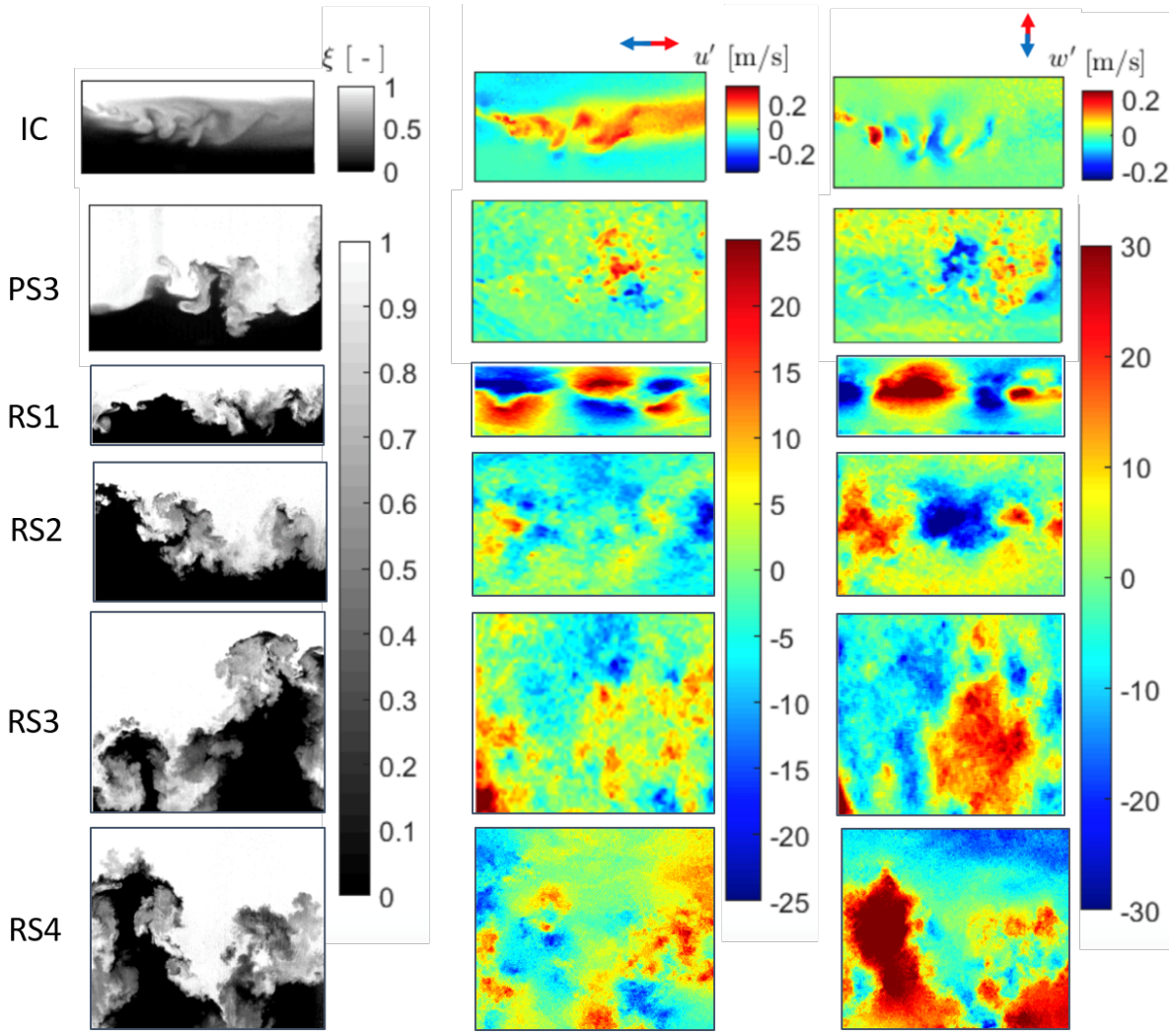

Figure 20: Example fields from single-shot experiments.

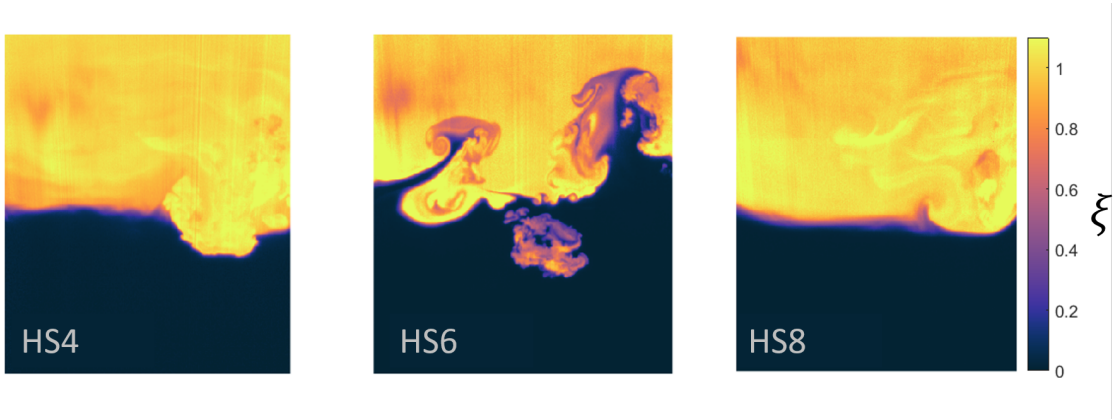

Figure 21: Initial conditions of a subset of 3 high-speed experiments.

4.0.1 Growth Rate

Figure 23 a) and b) show the result of applying both the Mikaelian model

$$\frac{\dot{h}_{0^+}}{\Delta V_0} = C_M A^{++} \tag{68}$$

and Eq. (31) to HS data and HSS data respectively, where ΔV_0 is the jump in interface bulk translational velocity, A^{++} is the post-re-shock Atwood number, and C_M is an empirically fitted value. C_M has been shown to have a range from 0.28 to 0.9 by Ukai *et al*. [50]. Here $C_M = 0.28$ and $C_M = 0.9$ are used with $C_M = 0.28$ corresponding to the original value ascertained from RTI experiments and $C_M = 0.9$ being the value found by Ukai *et al*. to fit well for sharp 3D ICs in RMI simulations. Here the ICs are diffuse, so a C_M of 0.9 providing the best fit for current data disagrees with previous results. Eq.(31) does not require any fitting constants.

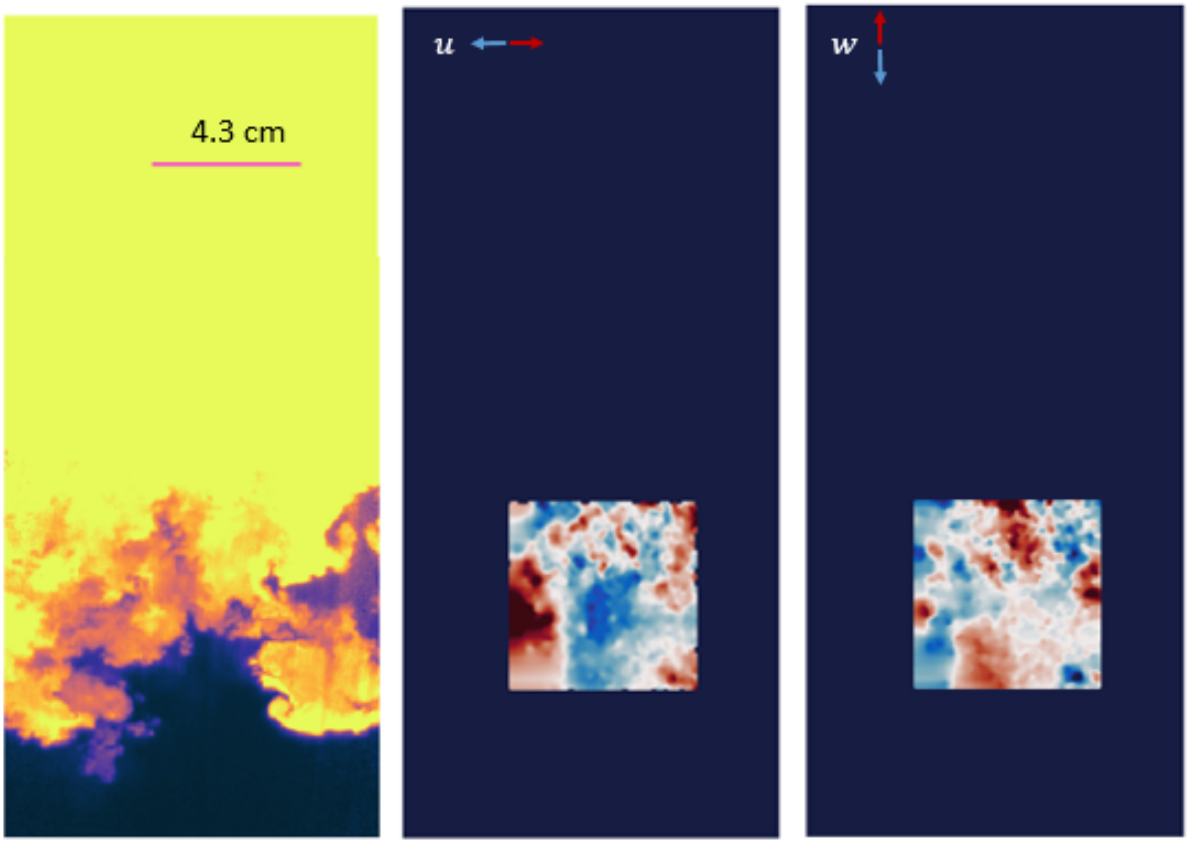

Figure 22: Example of corrected and registered concentration and velocity fields from HSS experiments.

4.1 Spanwise Averaged Moments

Following the definitions given in secs. (2.1-2.2.1) the first, second and higher order moments of each field are calculated and then ensemble-averaged for the SS, HS and HSS experiments. The spanwise averaged light-gas mole fraction profile, $\overline{\xi}$, from SS, HS and HSS data, shown in Fig. 24, all show strong collapse using the scaled streamwise coordinate, z^*. This provides confidence that this normalisation might be a useful tool. There is much less agreement between the single-shot and the high-speed results for the spanwise variance of the mole fraction field, $\overline{\xi'^2}$. This points toward IC variation being an important factor. For the high-speed data, only

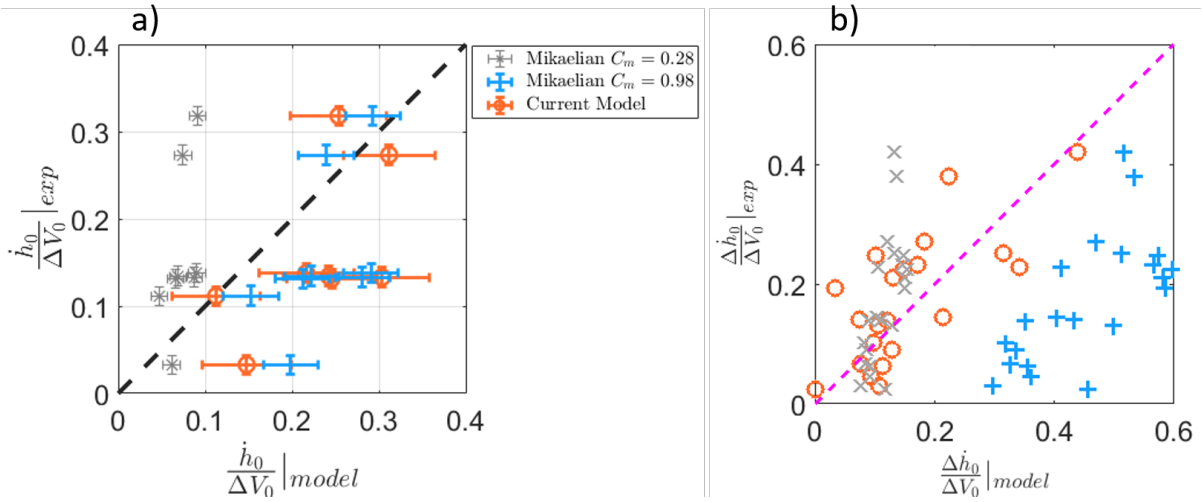

Figure 23: Comparison of Mikaelian reshock model with proposed vorticity deposition model (Eq. (31)), from a) HS experiments and b) HSS experiments.

eight experiments are available to average over, which is not enough to produce statistically meaningful results. However the trends seen in the single-shot data can still be corroborated. The mixing layer progresses toward a more mixed state shown by the decrease in the peak value of the variance. Also the peak shifts toward the light gas, which points to more mixing occurring around bubble-like structures below the center of the mixing layer.

The mean of the spanwise velocity $\overline{u^+}$ remains close to zero over time, which is reasonable from a mass conservation perspective in a wall-bounded flow: after the shock passes, the mixing layer behaves in an incompressible manner such that in a finite domain in the spanwise direction there shouldn't be a bulk spanwise velocity. The spanwise velocity variance $\overline{u^{+\prime 2}}$ shows an initial deposition of fluctuating velocity above and below the center of mixing layer, which then decays and is transported toward the center of the mixing layer.

The mean of the streamwise velocity $\overline{w^{+\prime}}$ similarly shows a value close to zero for RS1 to RS3 until RS4 where a linear velocity profile is present which describes a compression of the

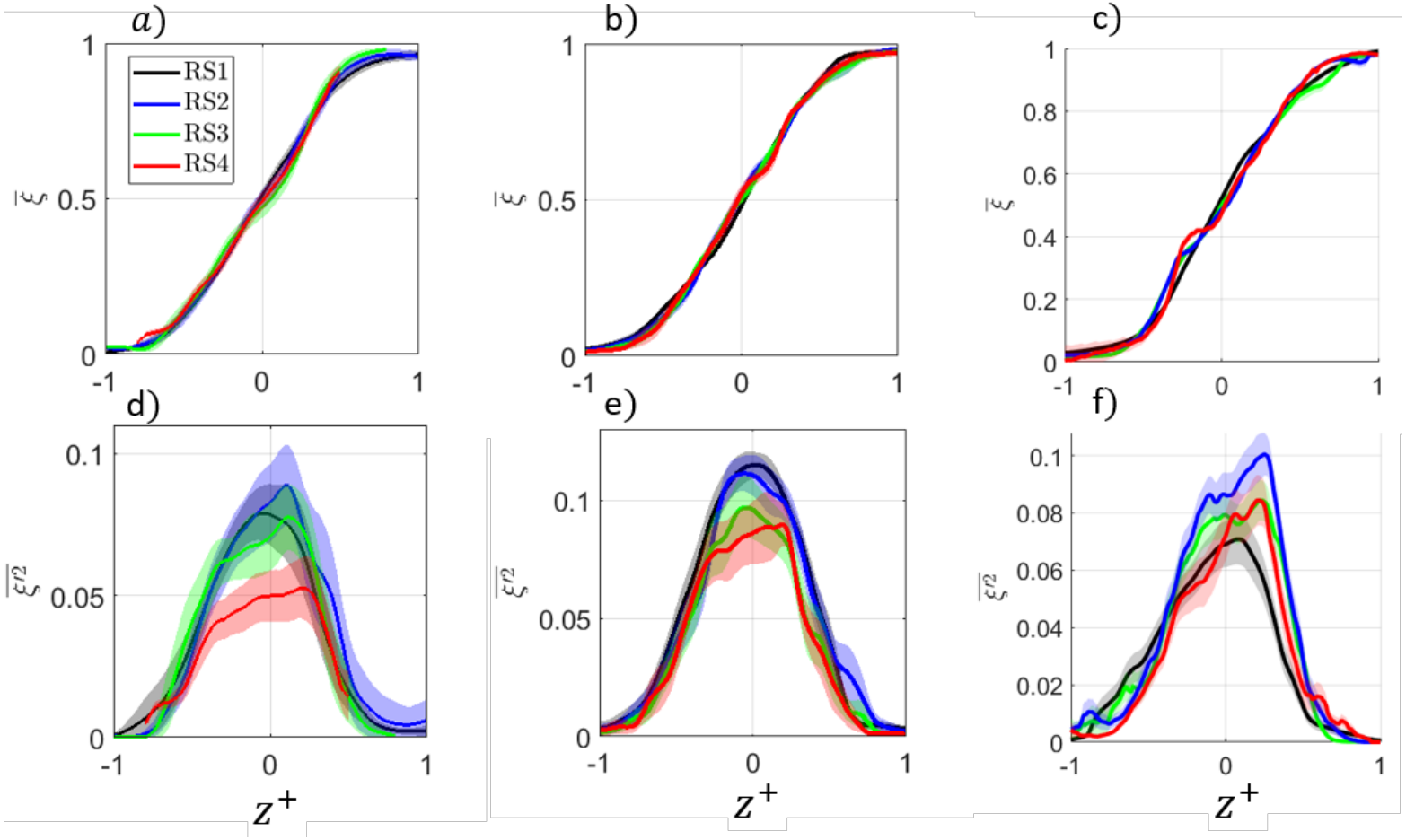

Figure 24: Spanwise averaged 1^{st} and 2^{nd} moments of the concentration field from all three experiment campaigns. For each post-reshock time, curves represent ensemble averages over 20 runs, while the shaded regions represent two times the ensemble variance. a) and d) SS, b) and e) HS and c) and f) HSS.

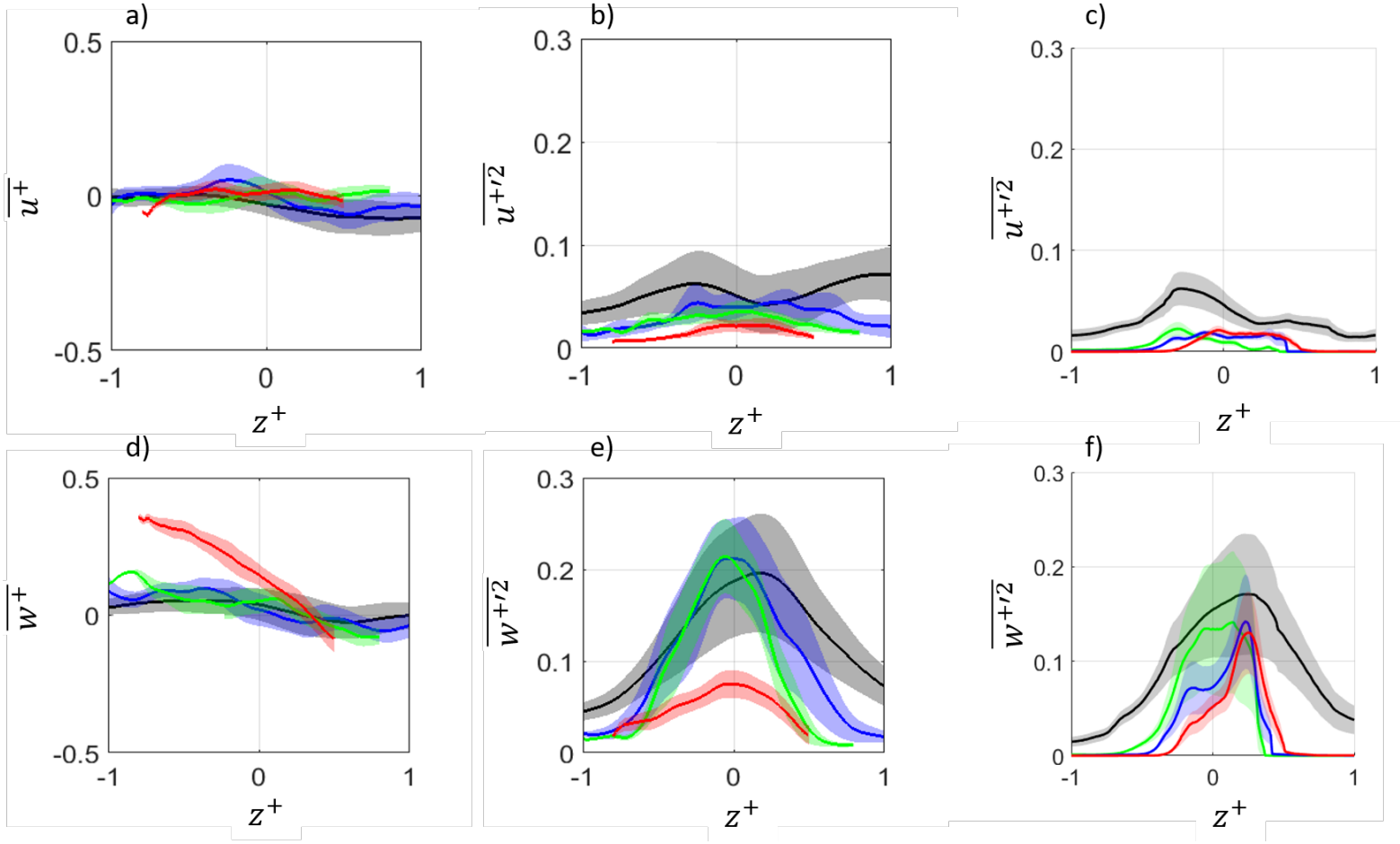

Figure 25: Spanwise averaged 1^{st} and 2^{nd} moments of the velocity fields from SS (a, b, d and e) and HSS (c and f) experiments. For each post-reshock time, curves represent ensemble averages over 20 runs, while the shaded regions represent two times the ensemble variance. Colorbars are the same as Fig. 24

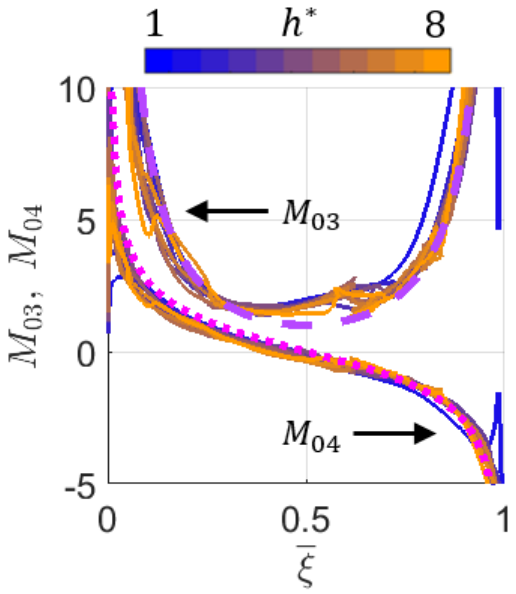

Figure 26: Skewness and kurtosis of the spanwise averaged light gas mole fraction from HS data. Note that h^* plays the role of a dimensionless time.

mixing layer whose cause can be seen in Fig. 13, in the compression wave being reflected from the contact surface.

4.1.1 Higher Order Normalised Moments

The concentration and velocity fields are analysed following the definitions given in section 2.2.1 to study skewness, kurtosis and higher order moments. The dotted and dashed lines in Fig. 26 show Eqs. (20) and (21) with $a_i = 1$ for all i, which corresponds to the simple PDF model not allowing any fitting parameters derived by Schopflocher and Sullivan [44].

This idea may be extended to mixed moments M_{ij}, of the velocity and concentration fields. Figure 27 shows plots of M_{ij} against the spanwise-averaged light gas mole fraction $\overline{\xi}$ from simulation results (obtained by Alex Ames using the *Miranda* code of LLNL) after shock and after reshock, and for single-shot experimental data after reshock. The similarity in profiles

suggests the possibility of a universal relationship such that $M_{ij} = M_{ij}(\bar{\xi})$ which was not further explored in the present work.

4.2 Probability Density Functions

Probability density functions (PDFs) are calculated in the mixing region defined by $|z^*| \leq 1$ for SS, HS and HSS campaigns. For all three sets of data, shown in Fig. 28, the PDFs of light gas mole fraction show a very similar temporal progression with a trend toward a more mixed state demonstrated by an increase in the PDF at values in the center of the range. In both sets of data the trend in mixing also shows an asymmetry with a local peak skewed toward the light gas. The RS1 time shown corresponds well with the PS4 time measured by Reese [35], and shows the continued mixing after reshock.

The PDFs of both spanwise and streamwise velocity from SS and HSS data show a decay of velocity kurtosis with an increase of the PDF peak at zero from RS1 to RS3 then a spread of the tails at RS4 corroborating the deposition of velocity fluctuations arising from the interaction of a compression wave with the mixing layer. The streamwise velocity PDF in Fig. 28 shows a dual peak near-Gaussian distribution at RS4, showing the mean velocity divergence which is seen in the spanwise averaged streamwise velocity profile in Fig. 25. This may be due to the passage of the compression wave shown in Fig. 13. The velocity component PDFs for both SS and HSS data seem to match pretty well with the evolution seen by Reese [35] for their high Mach number case, here a similar decay in distribution tail widths is observed over time.

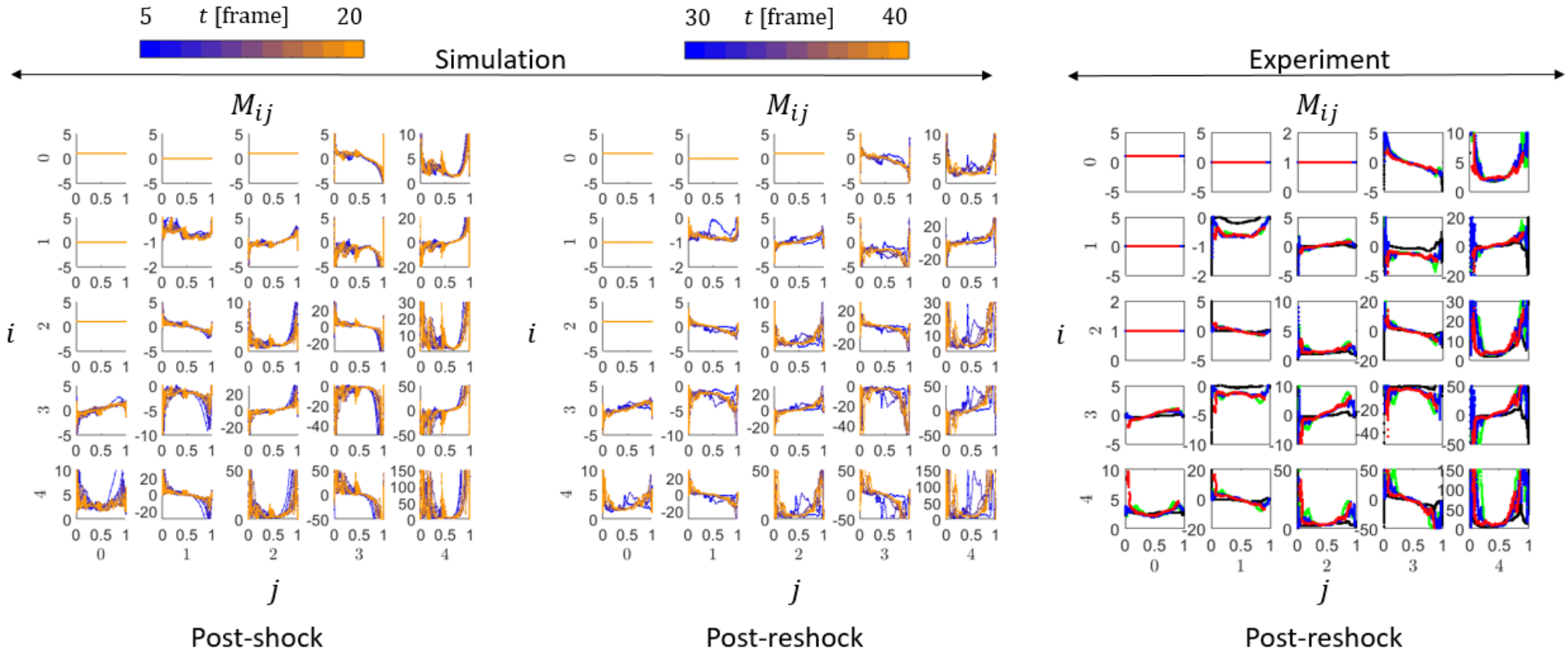

Figure 27: Plots of $M_{i,j}$, the spanwise averaged moments of the concentration and streamwise velocity fields from simulation data after shock and reshock, and single-shot experiment data after reshock. In each plot, horizontal axis is $\overline{\xi}$ and the vertical axis is M_{ij}. The color scheme for the right plot is the same as Fig. 24

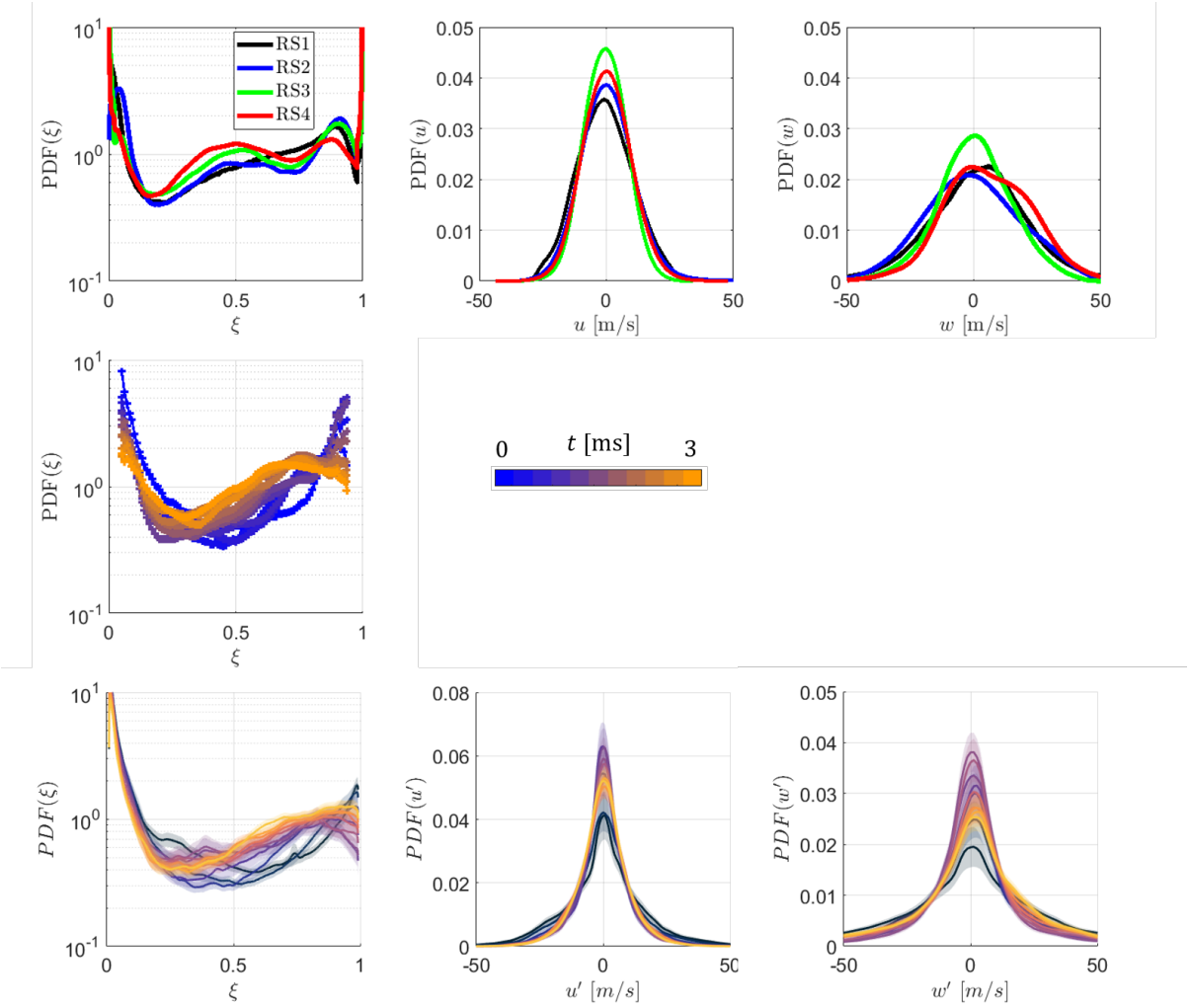

Figure 28: Probability distribution functions of the light gas mole fraction and the spanwise and streamwise velocities. Top: SS data. Middle: HS6 data. Bottom: HSS data

4.3 Spectral Analysis

4.3.1 Power Spectrum Evolution

Focusing on the HS data set, and a subset of 3 experiments, Fig. 29 shows Λ_ξ (Eq.(35)) from HS data for HS4, 6 and 8 as specified in Table 3. Λ_ξ is a measure of the magnitude of fluctuations at a given wavenumber with a smaller magnitude meaning weaker fluctuations from the mean and a more fully mixed state. The IC of HS6 in Fig. 21 visibly shows a broader range of scales and larger x-gradients which leads to a period of strong mixing immediately after the passage of the reflected shock. HS4 and HS8 show qualitative similarities in Fig. 29. HS4 and HS8 begin with smaller values of Λ_ξ at higher wavenumbers compared to HS6 which starts at higher values that subsequently dissipate. In the current data the scaling at higher wavenumbers does not appear to be IC dependent. All three experiments arguably show regions of KOC $-\frac{5}{3}$ scaling, which would identify an inertial-convective regime, however a region closer to $-\frac{11}{3}$ covers a much larger range for all three experiments.

Three representative wavenumbers are highlighted in Fig. 29 corresponding to the integral scale $L = \dfrac{\int_{-\infty}^{\infty} k^{-1} E_\xi dk}{\int_{-\infty}^{\infty} E_\xi dk}$, the scalar Taylor scale $\lambda^2 = \dfrac{\overline{\xi'^2}}{\left(\overline{\dfrac{\partial \xi'}{\partial x_i}}\right)^2}$, and an estimate of the scalar Kolmogorov scale, η, which is the Obukhov-Corrsin (OC) scale, using the isotropic homogeneous relation $\lambda = \sqrt{10}\eta^{2/3}L^{1/3}$. For all three experiments, the Taylor scale seems to be a demarcation point between the two scaling regions, an inertial range and an inertial diffusive range, with the OC scale estimated as being below the measurement spatial resolution ($\Delta = 0.245$ mm).

Moving to the HSS campaign, Figure 30 explores the coarse measures of the spectra introduced in Sec. 2.6. Figures 30a) and 30c) show joint probability density functions (JPDF)

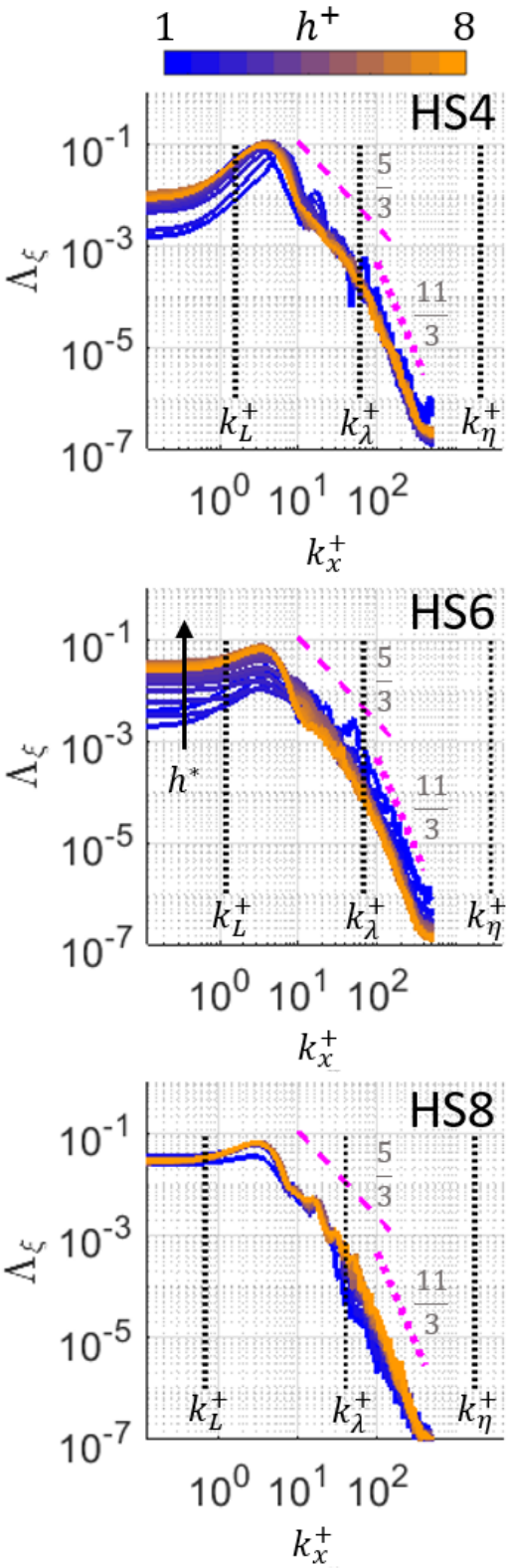

Figure 29: Evolution of the integrated scalar power spectrum (Eq.(35)) from high-speed data.

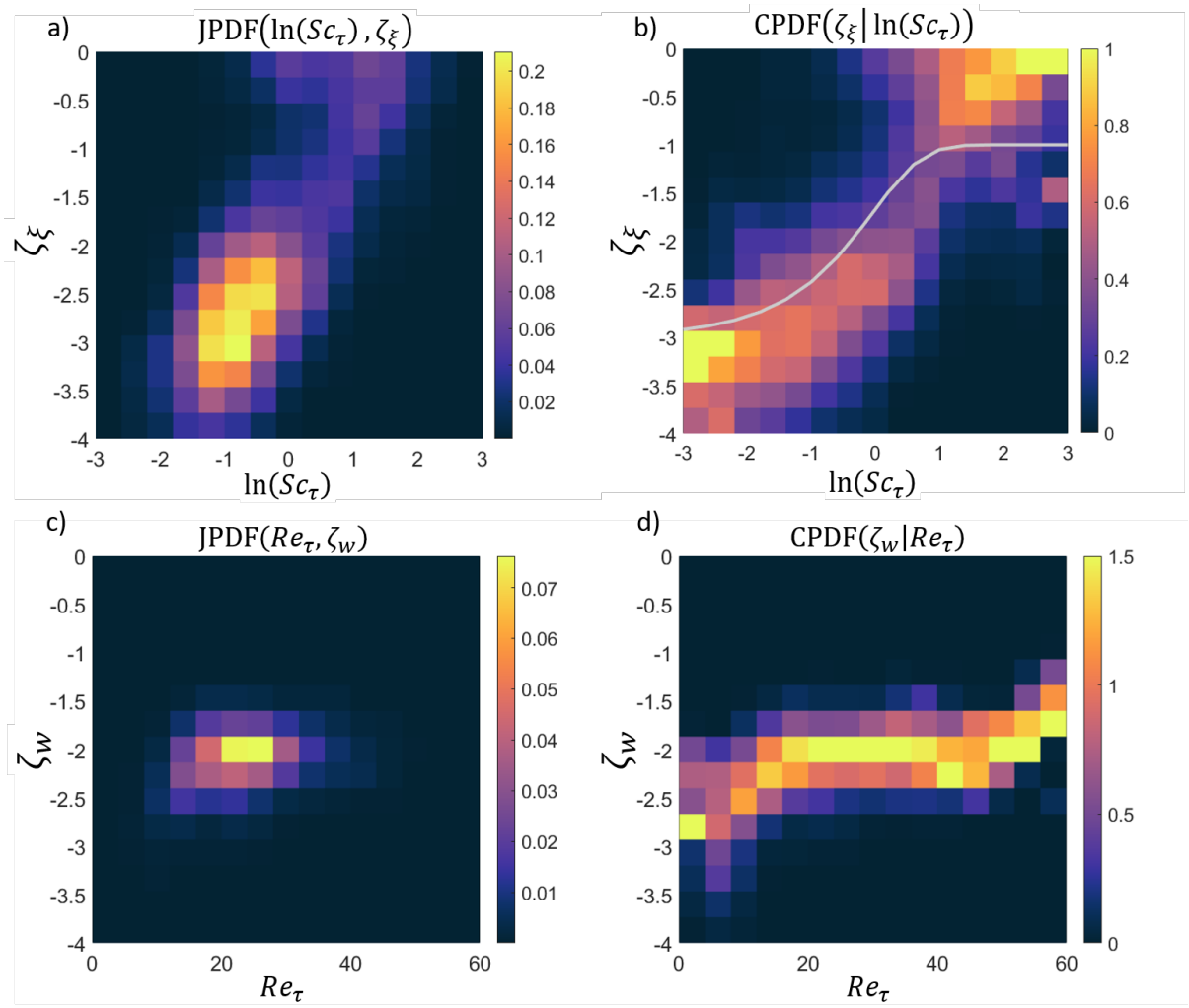

Figure 30: HSS data: a) joint PDF of spectral Schmidt number and scalar spectral slope. b) conditional PDF of scalar spectral slope given a spectral Schmidt number. (White line:[11, Eqn.(46)]). c) joint PDF of the spectral Reynolds number and the kinetic spectral slope. d) conditional PDF of the spectral Reynolds number and the kinetic spectral slope.

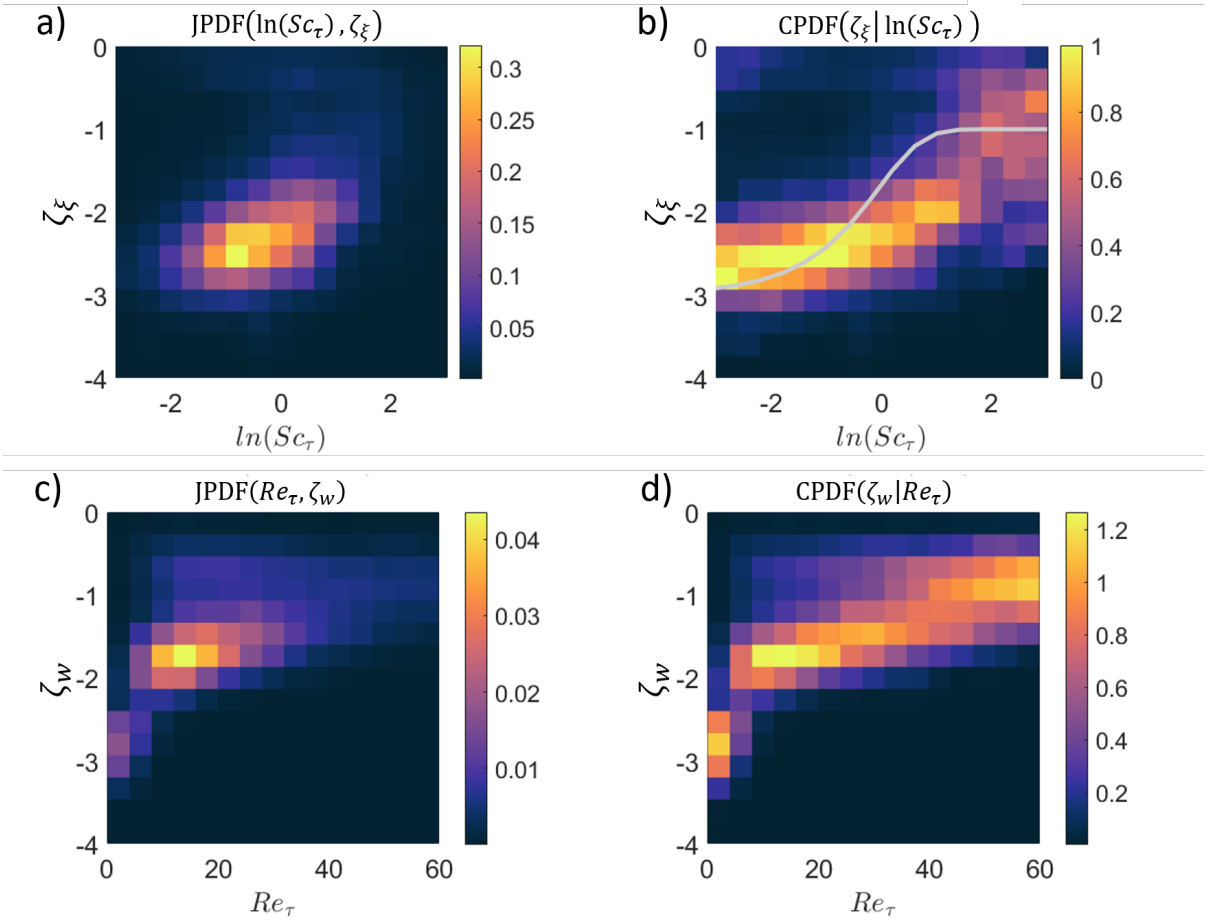

Figure 31: SS data: a) joint-PDF of spectral Schmidt number and scalar spectral slope. b) conditional-PDF of scalar spectral slope given a spectral Schmidt number. (White line:[11, Eqn.(46)]). c) joint-PDF of the spectral Reynolds number and the kinetic spectral slope. d) conditional-PDF of the spectral Reynolds number and the kinetic spectral slope.

and figures 30b) and 30d) show conditional probability density functions (CPDF). In particular, Figure 30a) shows the JPDF of the turbulent Schmidt number and the scalar spectral slope. A peak in the JPDF can be seen where the scalar slope is approximately between $-8/3$ and $-10/3$ and the turbulent Schmidt number is between 0.3 and 0.4 which aligns with the estimate of the material Schmidt number. Figure 30b) shows the CPDF which represents what the expected spectral slope is for a given turbulent Schmidt number. The result here is close to the interpolation formula by [11] (Eqn.(46) in that paper), providing some encouragement to the proposition made in Sec. 2.6, that with the flow being far from HIT, the turbulent Schmidt number is appropriate to use in place of the material Schmidt number to determine expected behaviour.

Batchelor *et al*. [2] propose a scalar spectral slope of $-\frac{17}{3}$ for a Schmidt number $Sc << 1$ which corresponds to the inertial-diffusive regime, whereas here $Sc = 0.3$. They propose that small scale mixing is independent of large scale straining. Gibson [11] argues that Batchelor's assumption that low wavenumbers of the scalar spectrum are not affected by larger scale straining is not necessarily a good approximation and instead of a $-\frac{17}{3}$ slope finds a -3 slope for the inertial-diffusive range. Frisch and Wisth [9] however find that for a white-in-time velocity field with an inertial range scaling of $-\frac{5}{3}$, the inertial-diffusive range should have a $-\frac{11}{3}$ scaling. Although this scaling appears in previous observations [29], its base assumption of a white-in-time velocity field doesn't match observed velocity field correlations that have non-zero integral time scales.

These attempts at developing scaling relations are for passive scalar quantities whose structure does not affect the dynamics of the velocity field. In RMI flows, the light gas mole-fraction is an active scalar. To the authors knowledge, there isn't an accepted universal model for active scalar scaling except for the well studied Bolgiano-Obukhov scaling which is expected in

buoyancy dominated flows.

Figure 30c) shows the JPDF of turbulent Reynolds number and kinetic spectral slope. A peak can be seen at a slope between $-5/3$ and -2 at an Re_τ between 20 and 25. The CPDF in Fig 30d) points to a weak dependence of the kinetic spectral slope on the turbulent Reynolds number, though it is difficult to draw conclusions at the lowest and highest Re_τ due to the lower number of observations available to generate the distribution there due to the turbulent Reynolds number over all measurements being close to the peak.

Figure 31 shows the same measures as figure 30 but for the SS data set. Very similar structures and values and trends are visible in the Schmidt number-based plots, 30a) and 30b). The Reynolds number based plots do show a peak at a slightly lower value than the HS results in plot 30c). Figure 30d) shows a similar trend for the small Re_τ range, however a similar problem occurs with fewer instances to produce statistics for the higher Re_τ values.

Figure 32 then shows the joint-PDF of Re_τ and $S\,c_\tau$. Overlaid on this contour plot is the time evolution of the average values. The effective Schmidt number begins around unity, such that the bandwidths of the kinetic and scalar spectra are the same. This follows from the structure of the deposition of velocity due to the passage of the shock described in Sec. 2.3.1 where at first order the spectrum of the deposited velocity deposition is proportional to the scalar spectrum.

There is a trend of the effective Schmidt number toward the material Schmidt number, while the effective Reynolds number increases quickly and then gradually decreases.

Figures 34 and 33 show the terms in Eqs.(32a - 32b) that can be extracted from SS data, so a pressure correlation term is not included. Each row corresponds to a time defined in Fig. 13.

The peaks of the scalar power spectra and the kinetic energy spectra (left columns in Figs. 33-34) demonstrate the same physics as the spanwise variances. However the spectra and the transport terms provide significantly more details about the processes occurring within the

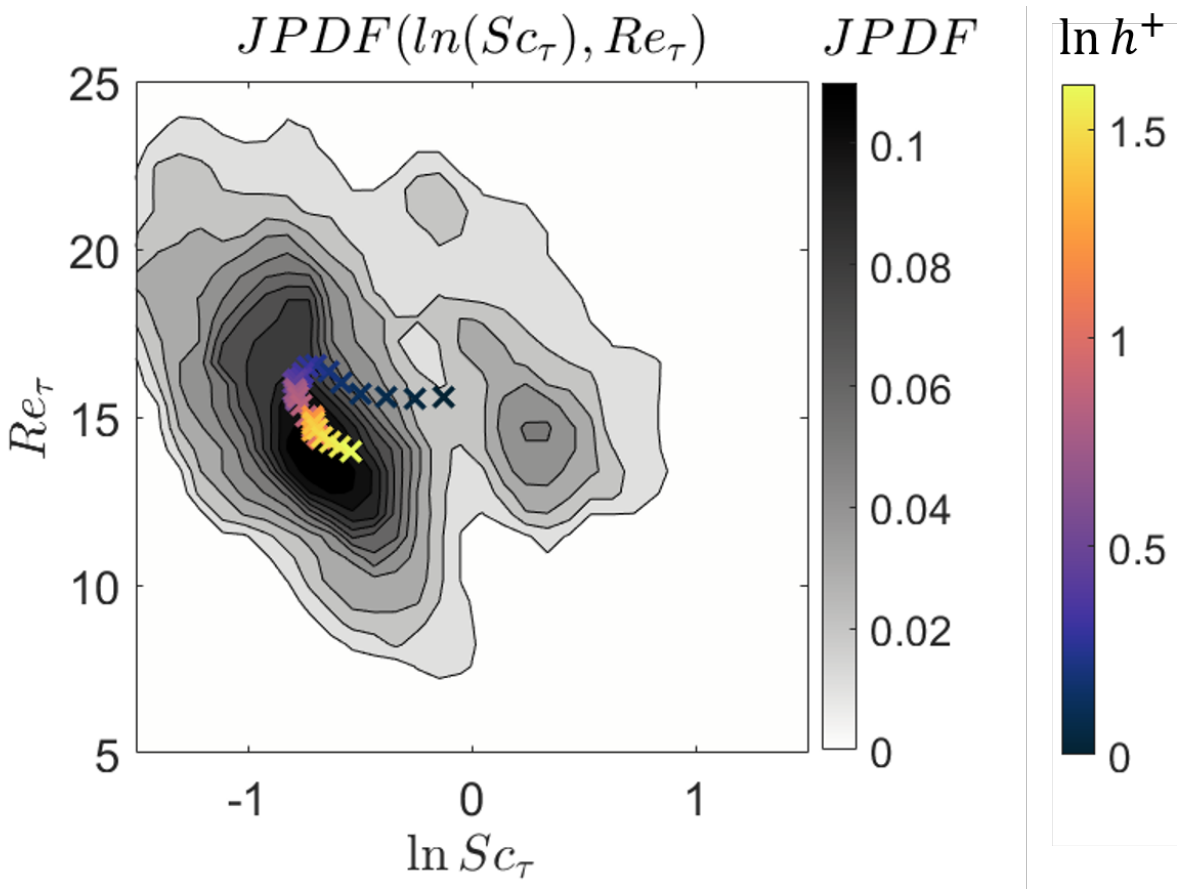

Figure 32: HSS data: Contour plot of the joint-PDF of the effective "turbulent" Reynolds number and effective "turbulent" Schmidt number. Overlaid × markers are the time evolution of the mean values of Re_τ and Sc_τ.

mixing layer.

In Fig. 34 the first column is the inhomogenous kinetic energy spectrum and the second column is the production term. For the kinetic production, for RS 1-3 there is no discernible pattern until RS4 where there is a strong production due to a compression wave interacting with the mixing layer. In contrast, for the scalar production in Fig. 33, there is always a mean scalar gradient and as such there is a production term at each time. This reaches its peak at RS3 where the kinetic energy spectrum also reaches its peak.

The fluctuating transport flux is shown in the third column of Figs.33,34. This describes how energy is transported from a given location and wavenumber. In the unforced regime, a consistent structure is observed in both the scalar and kinetic energy flux, with a negative flux in the center of the mixing layer, with positive flux above and below the interface.

Figure 35 is a sketch of the processes occurring in quasi-steady state between RS2 and RS3 for the scalar field. All terms (Table 1) are normalised by the peak of the power spectrum. This cartoon was constructed by making a separable assumption for all terms, such that $\Delta E_{\xi}(z^+, k_x^+) = E_0(z^+)\phi(k_x^+)$, then a Gaussian distribution in z^+ for all of the energy terms was assumed. The phases were then prescribed to maximise each term, and then the form of each term was readily available directly from these assumptions.

i) Scalar energy (Fig. 35a) - Energy is concentrated at larger wavelengths with an approximately Gaussian profile in the in-homogeneous direction.

ii) Production (Fig. 35e) - The production of scalar energy occurs at the largest scales on the same order as the peak of the power spectrum.

iii) Fictitious transport (Fig. 35b) - This transport, due to the choice of coordinate system, is concentrated in the same wavenumber range as the power spectrum and peaks above and below the center of the mixing layer.

iv) Homogeneous transport (Fig. 35c) - The flux of energy in wavenumber space is shown here. Above and below the center of the mixing layer, the flux is positive, with energy being transported from larger wavelength structures to smaller scales. In the center of the mixing layer the flux takes a negative value implying a backward cascade of energy from smaller scales to larger scales.

v) In-homogeneous transport (Fig. 35d) - The flux in the vertical direction shows that energy is transported away from the center of the mixing layer. There is an asymmetry here with a larger flux on the spike side of the mixing layer.

vi) In-homogeneous diffusion (Fig. 35f) - Energy diffuses due to mass diffusivity from the center of the mixing layer to above and below the center.

vii) Homogeneous diffusion (Fig. 35g) - Energy is transported to higher wavenumbers by molecular diffusion.

viii) Dissipation (Fig. 35h) - Energy is taken out of the system at shorter wavelengths due to self-interaction of gradients.

4.3.2 Partition of Energy

Equation(42) describes the partition of scalar energy over a given change in time for the case when velocity cannot be directly measured. The individual terms are plotted in Fig. 36 for HS data for the subset of experiments (HS 4, 6 and 8). The time period represented here begins after the reflected shock has fully traversed the mixing layer, it includes the passage of an expansion wave and ends at the latest dimensionless time available before the arrival of a compression wave.

The total change in energy, ΔE_{ξ}, is concentrated at larger wavelengths on the order of the

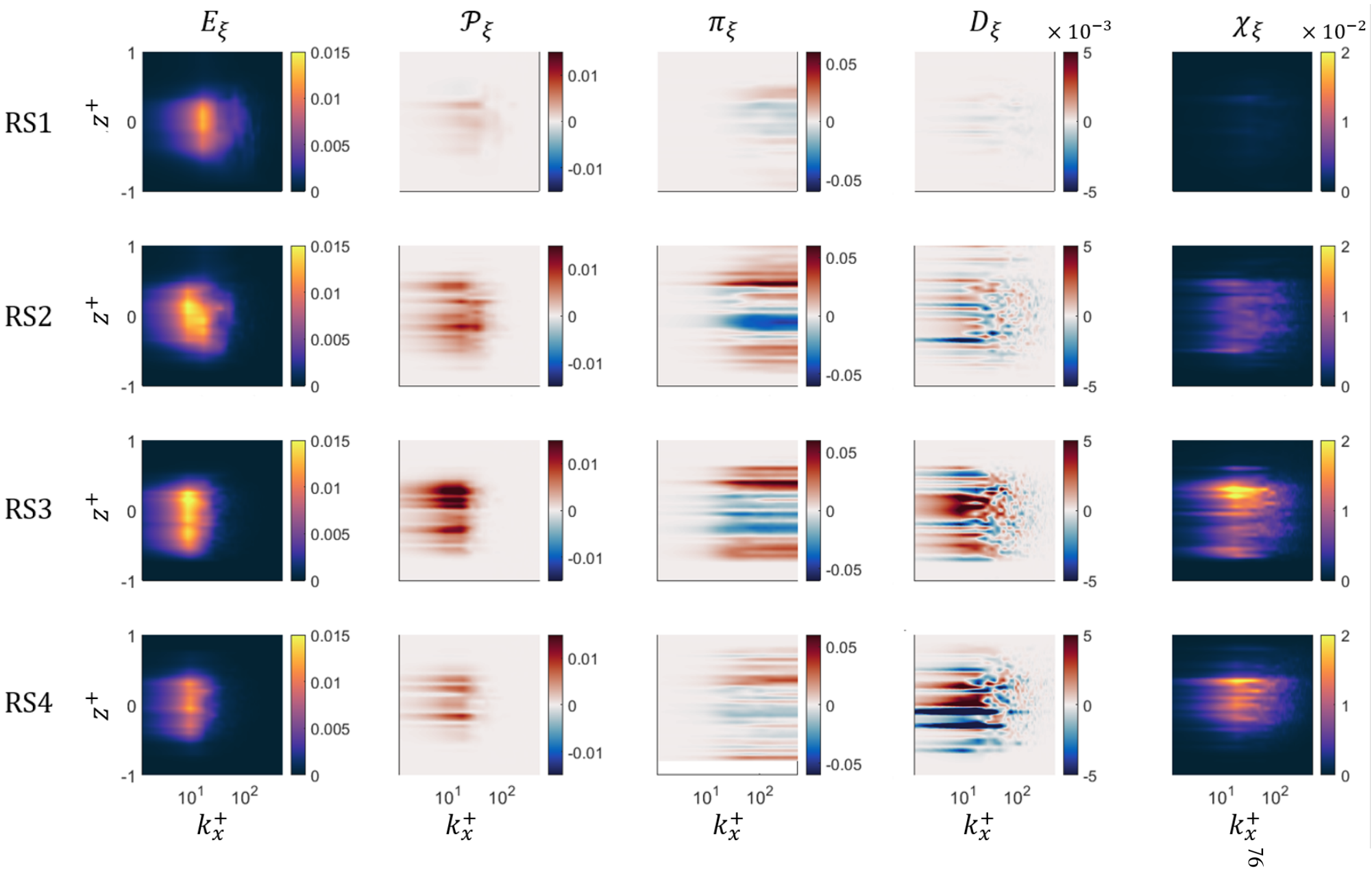

Figure 33: Contour plots of terms in the scalar power spectrum transport (Eq. (32a)) from single-shot data.

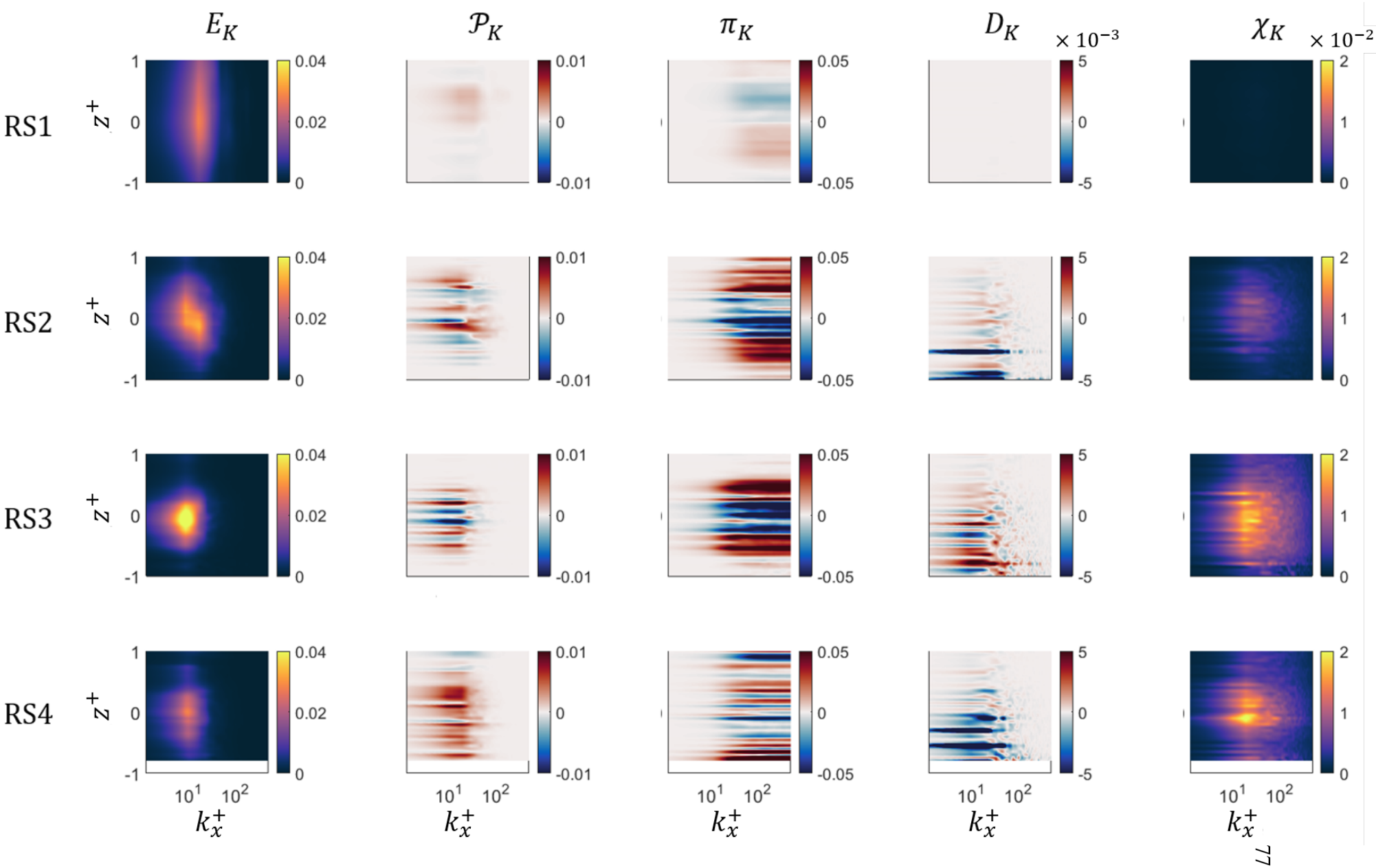

Figure 34: Contour plots of terms in the kinetic energy spectrum transport (Eq. (32b)) from single-shot data.

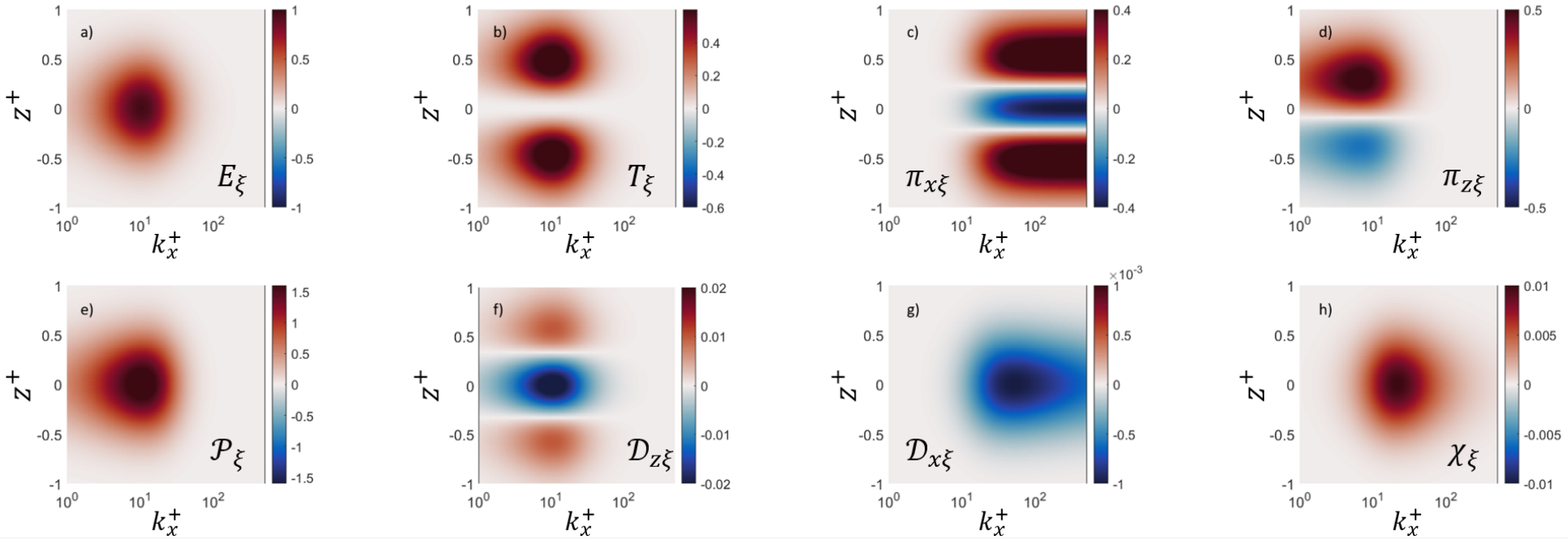

Figure 35: Cartoon of scalar spectral energy transfer.

shocktube width which correspond to the growth and transport of bulk structures. This is codified in the plots of bulk transport, T_ξ. The diffusion, D_ξ doesn't create or destroy energy, only transporting it within the mixing layer. χ_ξ is the dissipation term and represents the removal of scalar energy which appears to occur at shorter wavelengths.

The previous terms can be directly estimated from the measurements of the light gas mole fraction. The remaining term, the fluctuating flux Π_ξ, must be inferred from the time evolution of the the power spectrum. Unfortunately the fluctuating transport and the production term cannot be separated here as velocity isn't measured directly.

Cook and Zhou [6] calculate the time varying dissipation, production and transport in non-scaling coordinates for a shocked interface and find similar trends, with dissipation occurring at smaller wavelengths and production and transport reaching peaks at longer wavelengths.

The terms described in Eqs.(50a and 50b) are plotted in Figs. 37 and 38 respectively. For HSS data, we now have access to both the concentration and the velocity field so we no longer have to infer a combined production and transport term, instead the production and homogeneous and in-homogeneous fluxes can be directly calculated.

For the evolution of the scalar field we see the structures identified in the cartoon in Fig. 35 which gives some confidence that the underlying assumptions made to create the sketch are not too aggressive. In this case though the assumption of a symmetric Gaussian variance in the inhomogeneous coordinate doesn't hold. An asymmetry about the center of the mixing layer is present due to non-zero Atwood number effects such that the peak in the change in energy ΔE_ξ and the production of energy P_ξ are weighted to the bubble side of the mixing layer, and the structure of the homogeneous transport $T_{x\xi}$ is also skewed.

The Production term has an expected structure, where its peak is around the peaks of the scalar and kinetic power spectra, and most of the production happens at large scales with the

fluctuations feeding off of the mean gradient of the scalar field.

The homogeneous transport term has a structure similar to the time evolution of SS data in Fig. 33. This shows a transport of energy above and below the interface from large scales to small scales, while around the center of the interface a "backscatter" of energy is observed, such that smaller structures seem to be absorbed and merge into larger structures.

The in-homogeneous flux $\Pi_{z\xi}$ shows transport away from the center of the mixing layer, with the bubble structures receiving more transported fluctuations.

The diffusion terms, $D_{x\xi}$ and $D_{z\xi}$ fit strongly with the structure of the scalar energy having a weighted Gaussian structure in the streamwise coordinate.

The dissipation X_ξ shows a broad structure in the inhomogeneous direction while its effect is more localised than diffusion but is located at larger length scales around the integral scale.

Figure 38 shows the linear growth regime time integrated kinetic power spectrum evolution terms. The effect of diffusivity gradients on the flow can be seen in the γ_w term where energy is taken out of the flow due to interaction between the gradients of the diffusivity (with dependency on the temperature and scalar fields) and the gradients of the velocity field.

The transport in the homogeneous direction again says that energy below the mixing layer is transported to small scales, in the center of the mixing layer a "backscatter" is observed, and above the mixing layer no forward transfer is seen with the current parameters. Comparing with the time evolution in Fig. 34, this behaviour is seen at the earliest times, and may be dominant over more of the linear growth regime than could be seen at discrete times.

The homogeneous diffusion term D_{wx} is a little harder to disentangle. At lowest order, it is a pure homogeneous diffusion of specific kinetic energy, that is to say the power spectrum of w^+. A first term in an expansion of the viscosity and density terms has the expression $-\widehat{\overline{\mu^+}k^{+2}w^+}\widehat{w^+}^*$ and that is what can be seen in the center of the mixing layer and at large wavelengths. The next

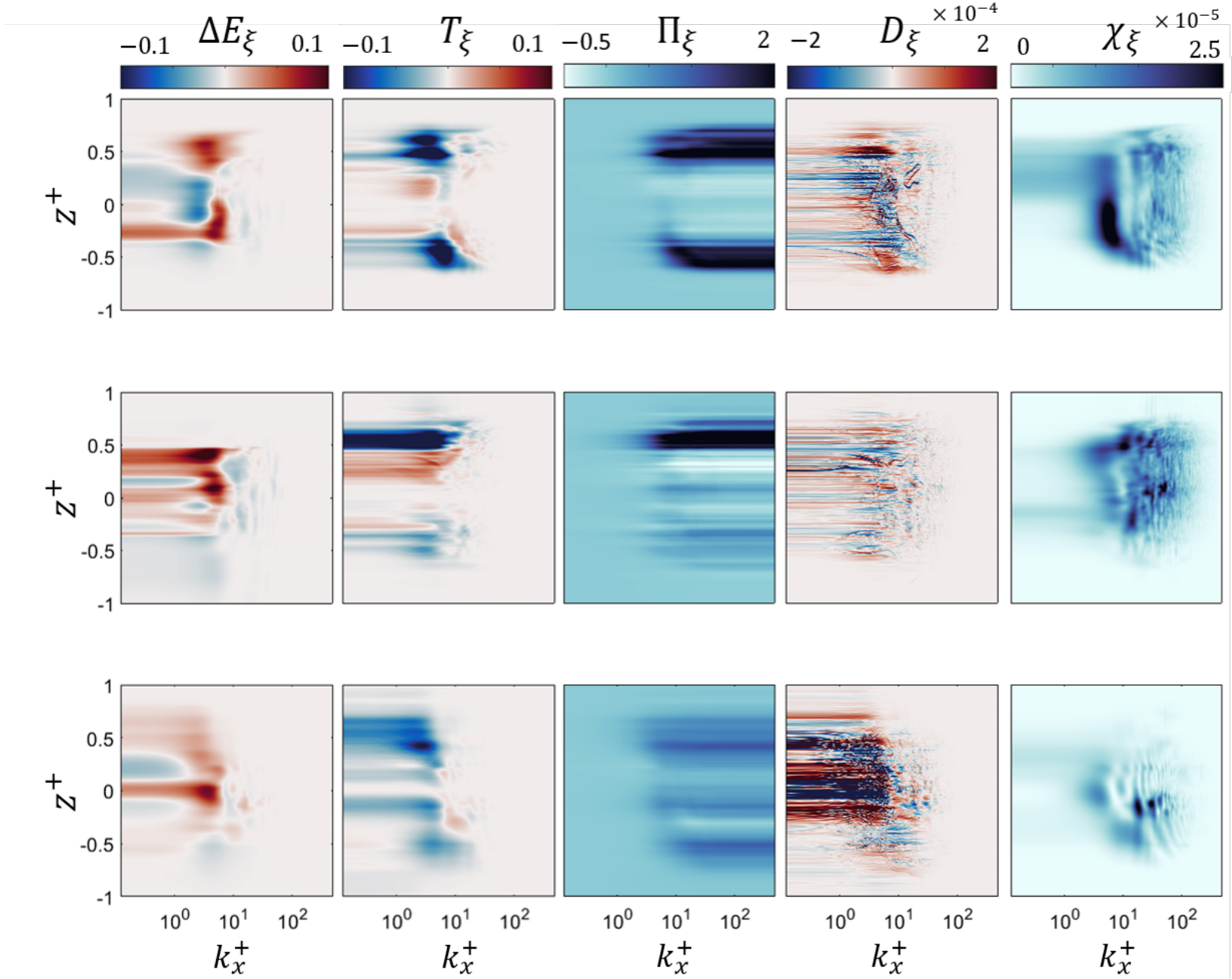

Figure 36: Plots of the partition of energy described by Eq.(42) for HS 4 (top), 6 (middle) and 8 (bottom).

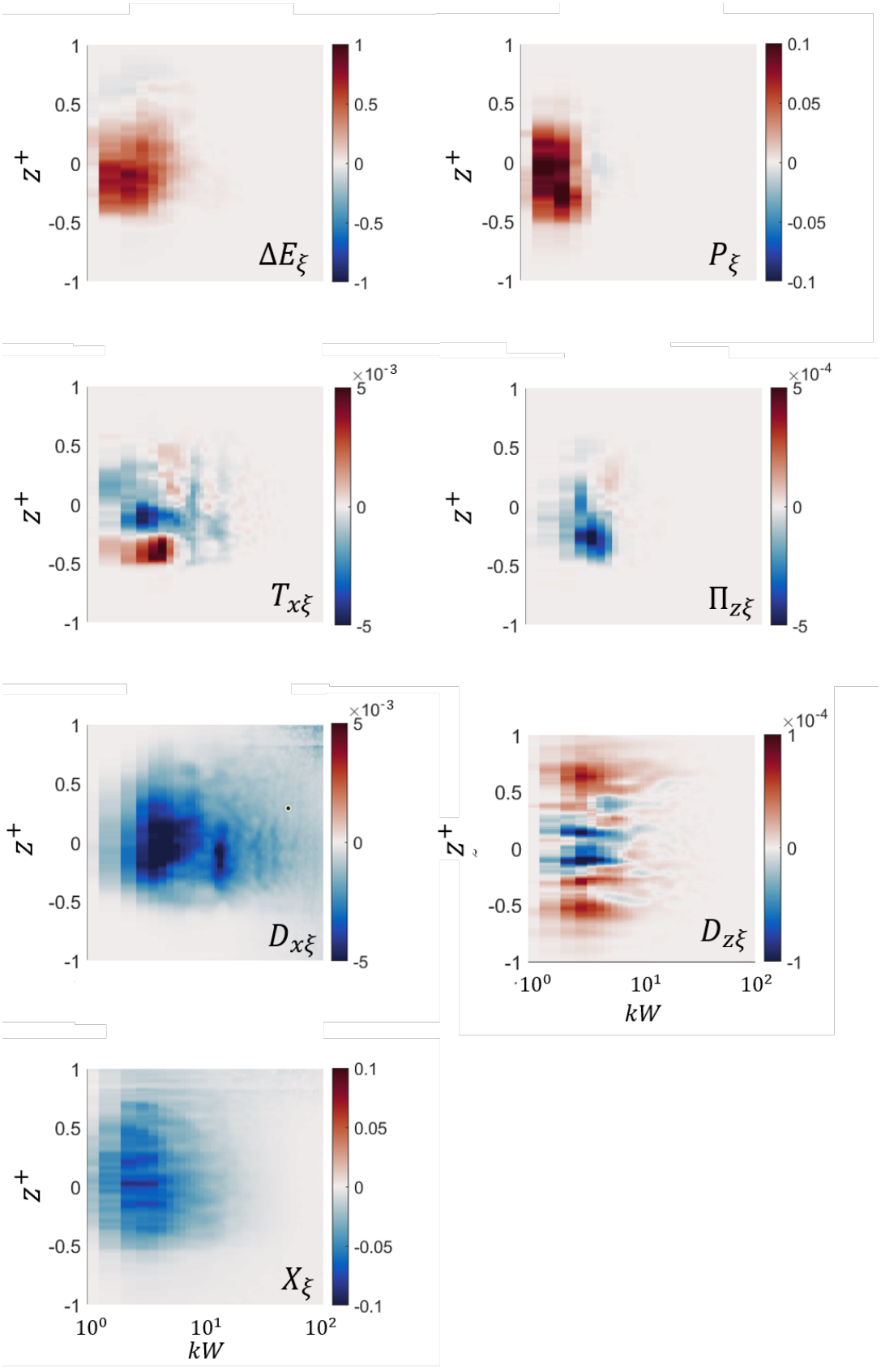

Figure 37: Partition of scalar energy from HSS experiments.

terms in this expansion become positive and thus at higher wavenumbers these contributions from the density and viscosity variation become apparent.

D_{wz} is the inhomogeneous diffusion term that describes how energy is transported by molecular diffusion above and below the interface centroid. Energy is taken from the peak of the kinetic energy and diffused away from the peak.

Figure 39 shows a comparison of the time evolution of the scalar production and homogeneous flux for both SS data and HSS data. The identifiable structures are very similar between the two data sets and the absolute normalized values are comparable. The difference in the strength of the production term, which is the dominant dissimilarity, is potentially a function of IC dependence.

4.4 Structure Functions and Exponents

Figure 40 shows the integrated 2$^{\text{nd}}$-order structure function $Z_{\xi,2} = \int_{-\infty}^{\infty} S_{\xi,2} dz^*$ from HS data. This is closely related to the energy spectrum and is another method of describing the energy contained at a given scale. The plots of $Z_{\xi,2}$ support the same analysis as the plots of Λ_ξ (Fig. 29) where HS6 begins with more energy at the smaller scales which subsequently dissipate while HS4 and HS8 begin with less energy at small scales and energy subsequently transfers down from larger scales.

The reference lines shown in Fig 40 are the KOC scaling of $\frac{2}{3}$ and a scaling of unity that very closely matches the observed slope.

KOC scaling proposes that the exact result of Kolmogorov's $\frac{4}{5}$ law can be extended beyond the 3rd order for which it was derived such that the exponent, ζ_p, of the integrated structure function, $Z_{\xi,p} \propto r^{*\zeta_p}$, is equal to $\frac{p}{3}$.

Figure 42 shows the evolution of the p^{th}-order exponent for the scalar and spanwise and

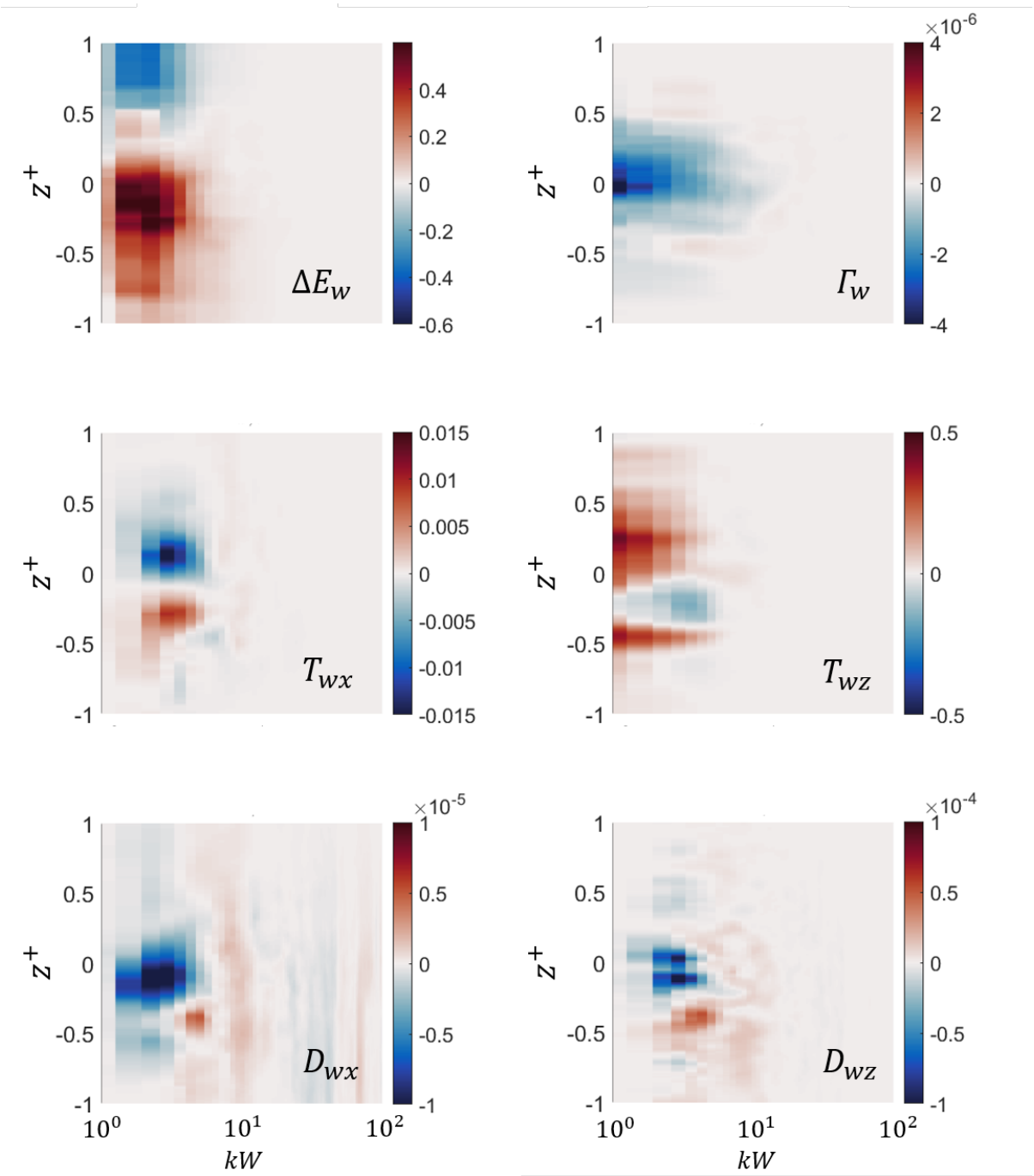

Figure 38: Partition of kinetic energy from HSS experiments.

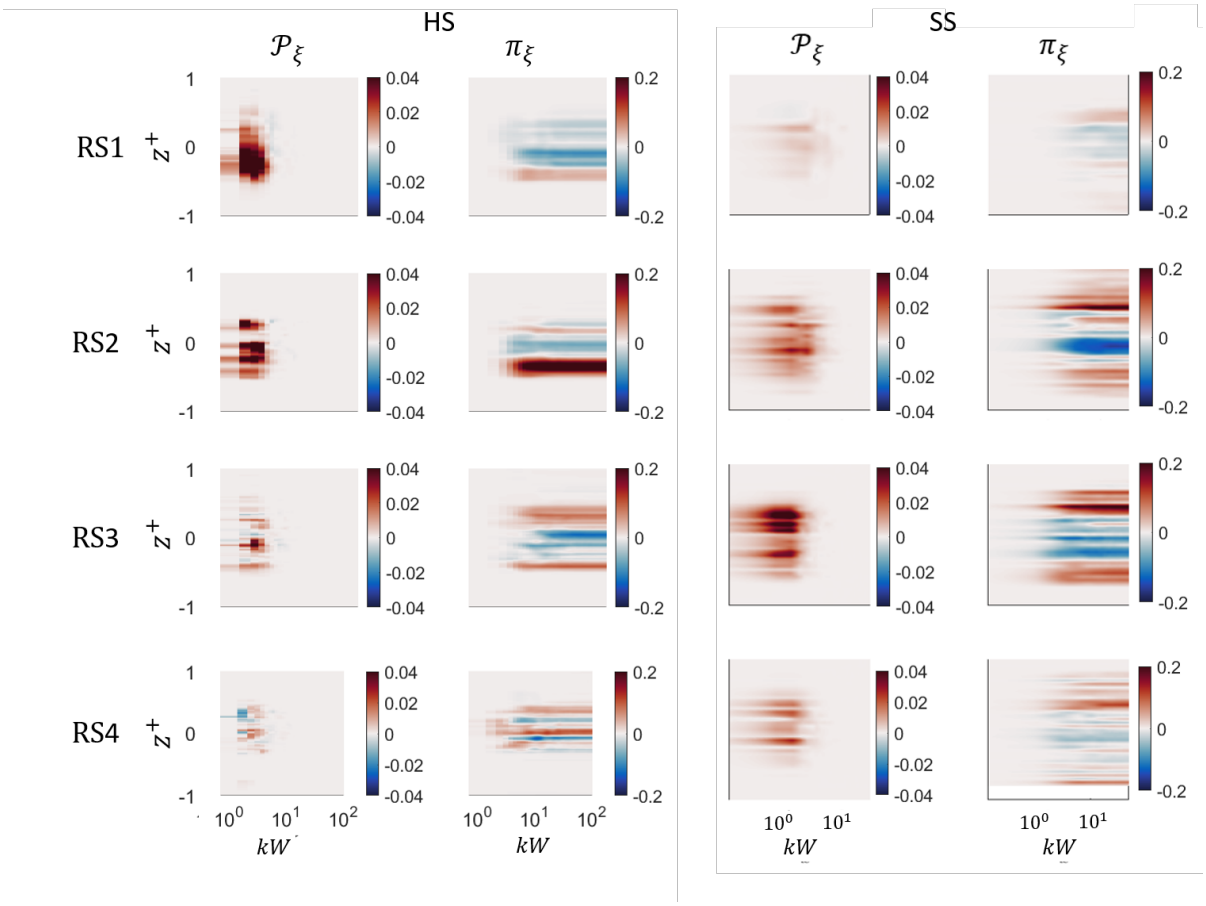

Figure 39: Comparison between SS and HSS experiments.

streamwise velocity fields for SS data. The plot of the spanwise velocity exponent shows no time evolution, with it following KOC scaling very well. On the other hand the streamwise velocity exponent does have a time evolution that seems to tend toward the KOC scaling while the exponent of the scalar structure functions looks to tend toward the K scaling similar to the HS results.

In Figs. 40, 41, 42 and 43 ζ_p, the exponent of the p^{th}-order integrated scalar structure function is also plotted. Kraichnan [18] proposes a scaling of $\zeta_p = \frac{1}{2}[\sqrt{6p+4} - 2]$ using a model for the diffusion of the passive scalar. The Kraichnan (K) prediction of $\sqrt{p}$ at large p works well for HS6 where the higher initial Reynolds number (Re_{h_0}) allows the flow to become more fully mixed. HS4 and HS8 both have ICs far from KOC or K scaling but seem to be trending toward these scalings. The single-shot data show large variation at higher values of p, which points to potential IC dependence borne out by high-speed data which shows similar evolution for HS4 and HS8 with similar structures in their IC and a distinct evolution for HS6 which has a wildly different IC.

Figure 44 shows the partition of scalar energy for the 2^{nd} order structure function $S_{\xi n}$. The second order production tells a similar story to the energy production term in Fig. 37. There is a production at large scales that is asymmetric about the mixing layer. The second order homogeneous transport term $\Pi_{x\xi 2}$ shows a dominance of transport from large scales to small scales while the inhomogeneous transport shows a similar trend to its Fourier counterpart in that energy is transported away from the peak of the second order structure function.

The first dissipation $X_{\xi 2}$ is comparable to its Fourier counterpart, energy is taken out of the system across a wide range of scales but this destruction is concentrated at larger scales. The second dissipation $X_{X\xi 2}$ does not have a Fourier comparison. This term is subdominant to the first dissipation, and acts in the same sense, taking energy away from the system, but its

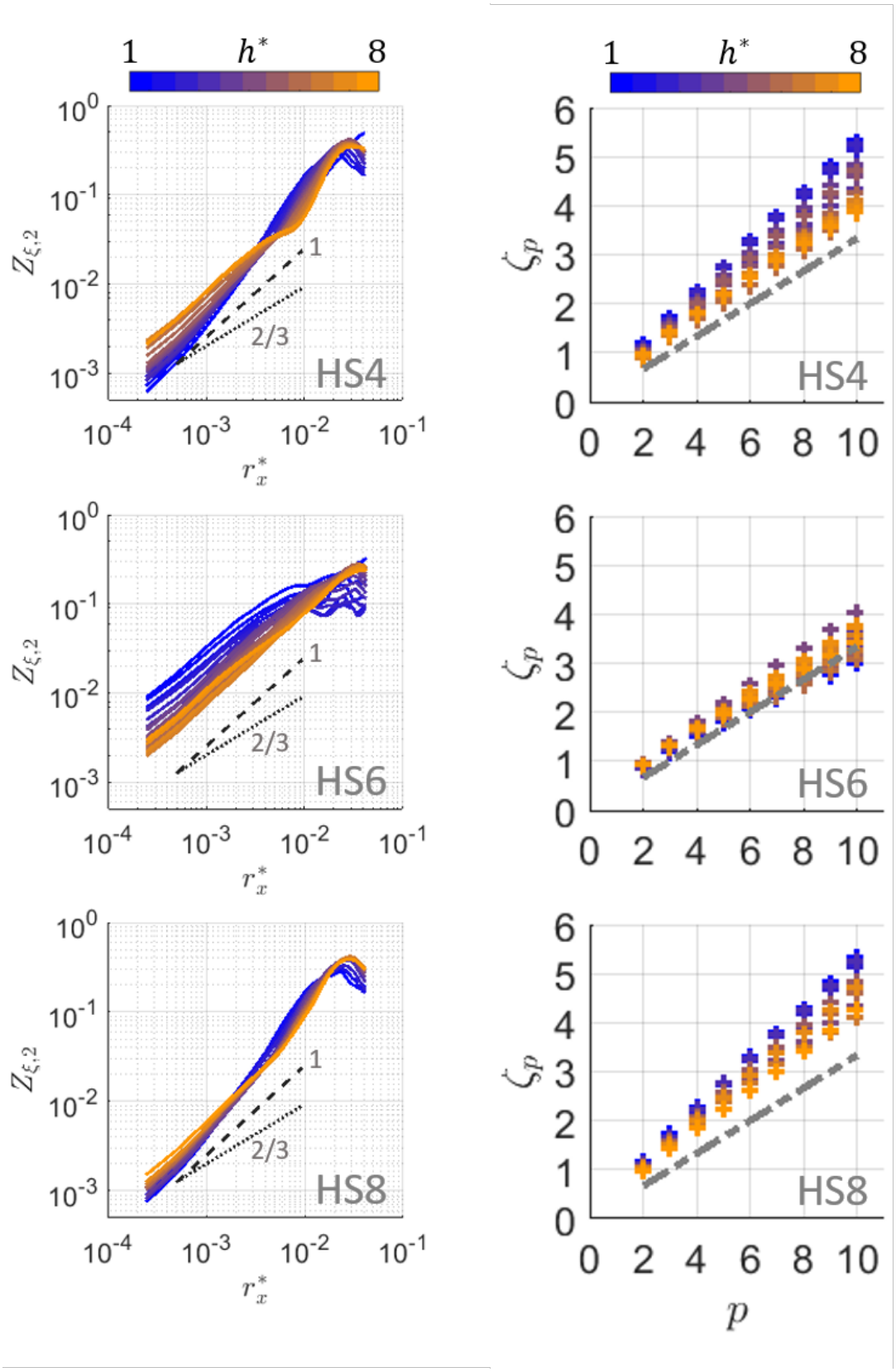

Figure 40: Scalar structure functions. Left: temporal evolution of 2nd order integrated structure functions. Right: temporal evolution of the p-th order structure function exponents. The dashed line marks KOC $p/3$ scaling.

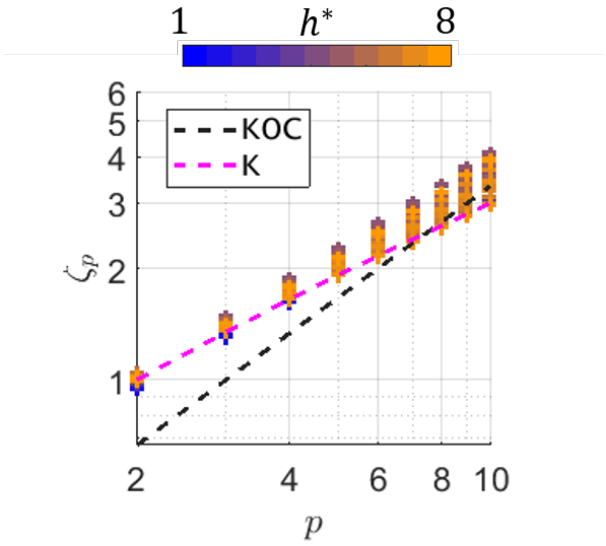

Figure 41: Scalar structure function exponent for HS6 (Gray dashed lines - KOC scaling, pink dashed line Kraichnan scaling.)

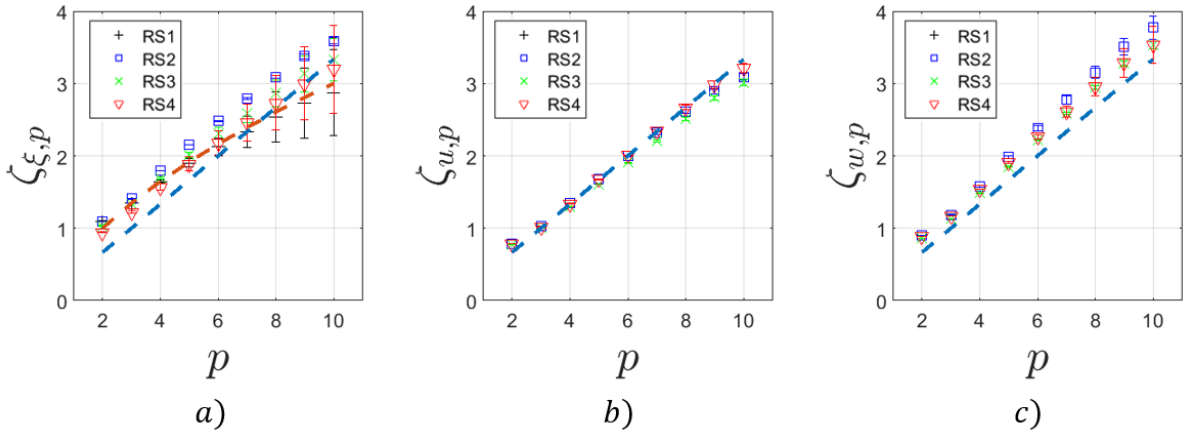

Figure 42: Structure function exponents from SS data. a) scalar SF exponent, b) spanwise SF exponent and c) streamwise SF exponent (red dashed reference line - K scaling, blue dashed reference line - KOC scaling)

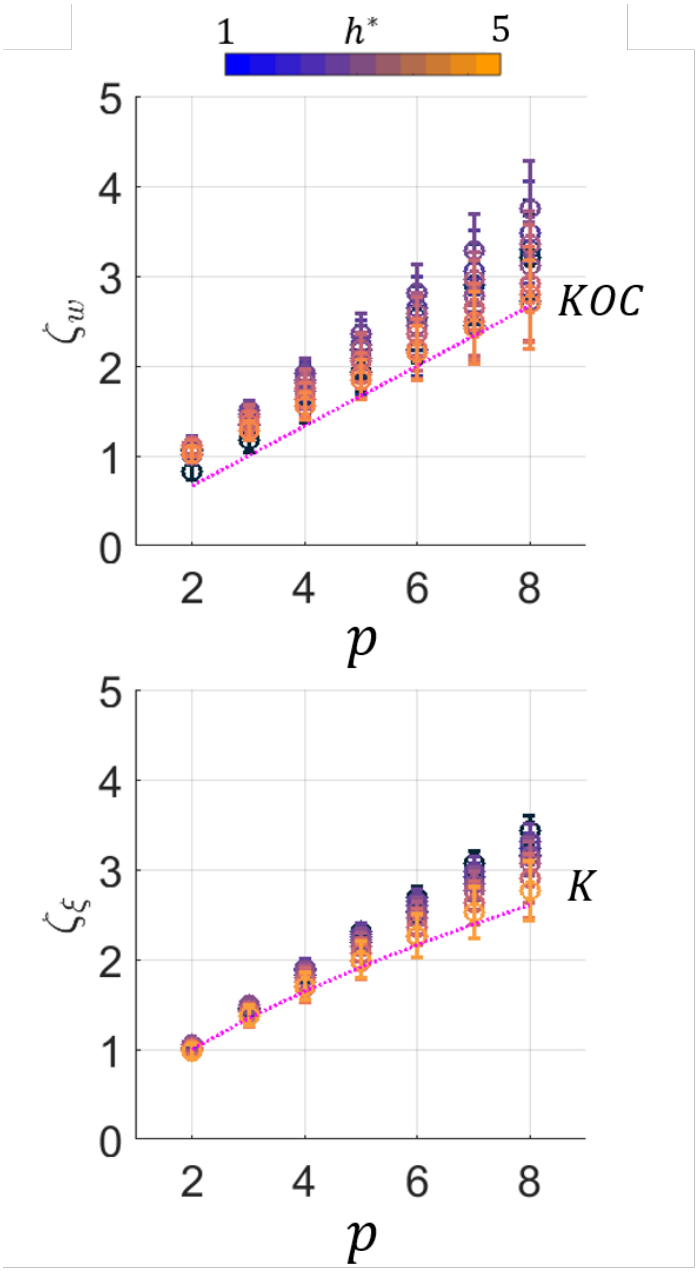

Figure 43: Structure function exponents from HSS data (red dashed reference line - K scaling, blue dashed reference line - KOC scaling).

mechanism is that it feeds off of gradients in the averaged coordinates instead of just gradients in separation space.

Lastly Fig. 45 allows the interrogation of how the transport terms behave as a function of order p. The terms in Eq. (52) are integrated over z^+ to attain transport terms for $Z_{\xi p}$.

The odd order terms in the dissipation terms are the point of interest here. In the dissipations Fourier equivalent, this term is always positive definite. Here the odd order terms point to the dissipation term injecting energy into the system while the even orders perform as expected removing energy from the system.

4.5 Filter-Based Scale-To-Scale Energy Analysis

Lastly, the use of a filter-based approach to exploring energy and energy transport at a given scale is considered. The analysis described in Sec. 2.5.1 is performed on HSS data.

Figure 46 shows the relative contribution of the three mechanisms defined in Eqs. (60a), (60b) and (60c).

The top row here describes the time evolution and the dependence on filter scale, while the bottom row has integrated the terms over dimensionless time so the structure as a function of location within the interface can be explored. The dominant term at all times and length scales investigated is the local strain term (a) and (d) that, similar to the second order structure function homogeneous transport, says that the transfer of energy from local scales to subfilter scales dominates.

The non-local strain term is the secondary term, then followed by the non-local vortex term. over the whole linear growth regime considered, the ratio of strengths of each term is approximately steady such that $\Pi_{LS} : \Pi_{nLS} : \Pi_{nL\Omega}$ is $0.75 : 0.2 : 0.05$. The ability to decompose the contributions of different mechanisms and investigate their relative contributions allows the

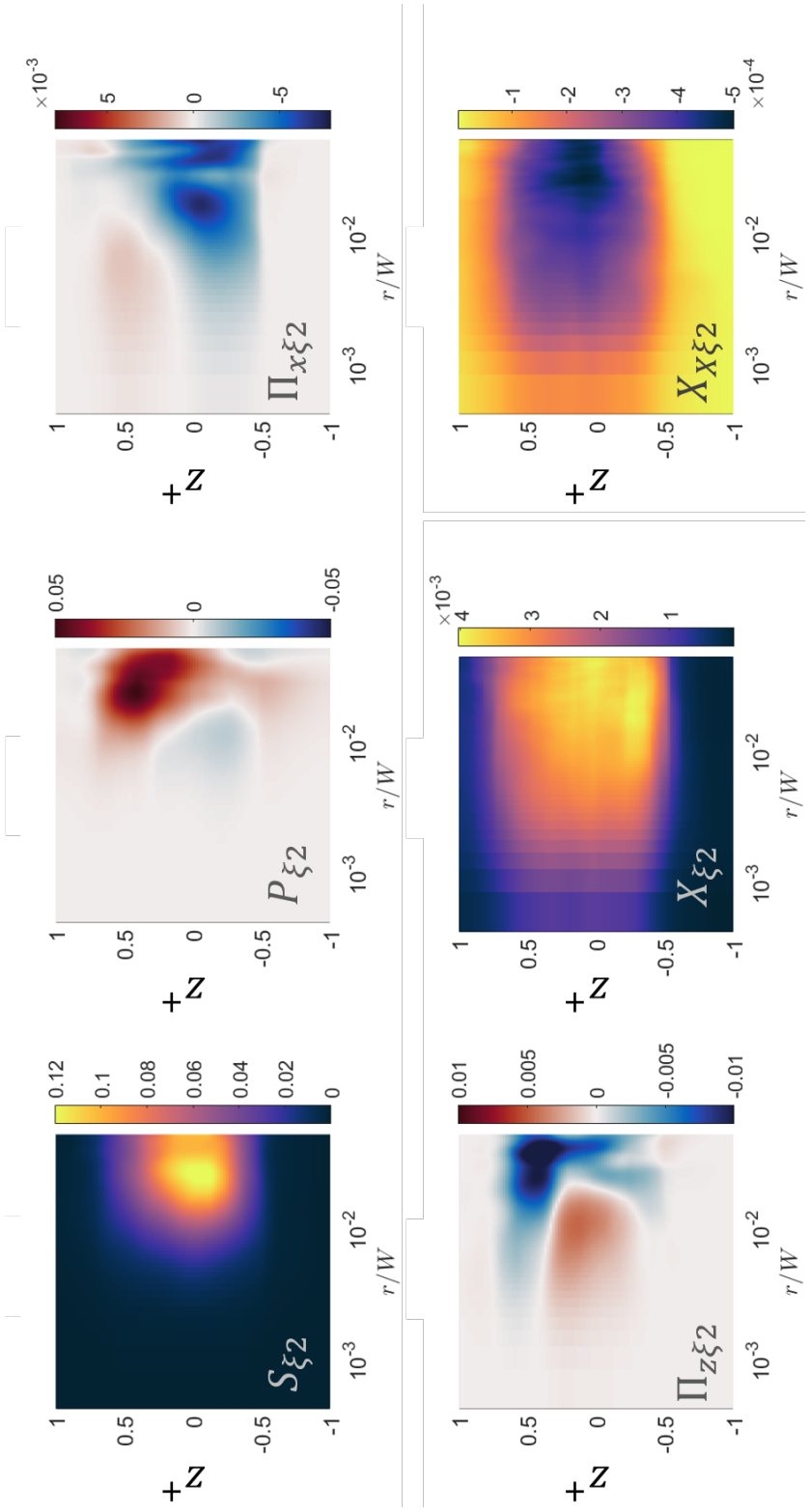

Figure 44: Transport terms for $S_{\xi 2}$ from HSS data

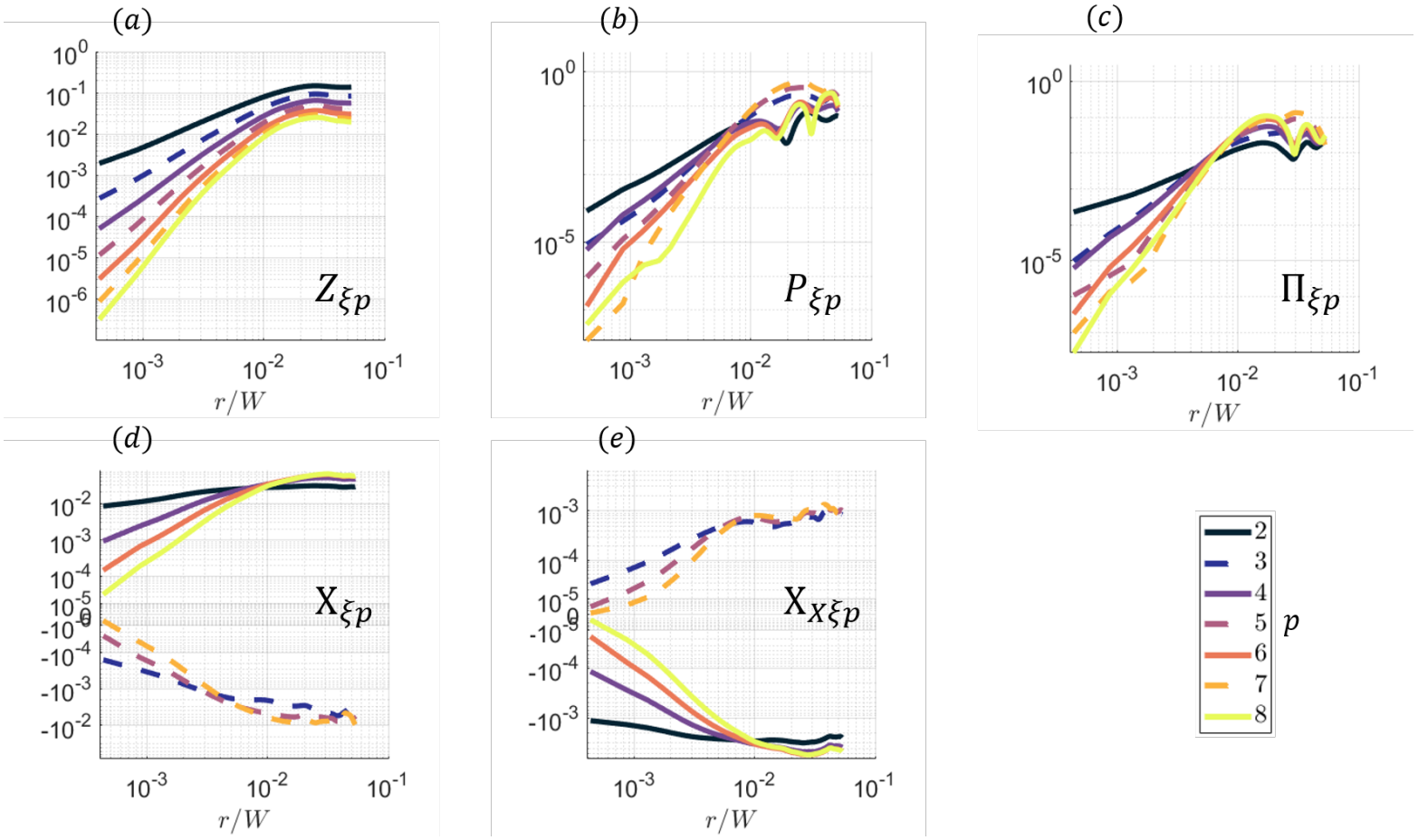

Figure 45: Transport terms for $Z_{\xi n}$ from HSS data

potential of modelling these separate terms and discussion of relative importance to decide if some contributions may be needed in certain ranges or can be discarded.

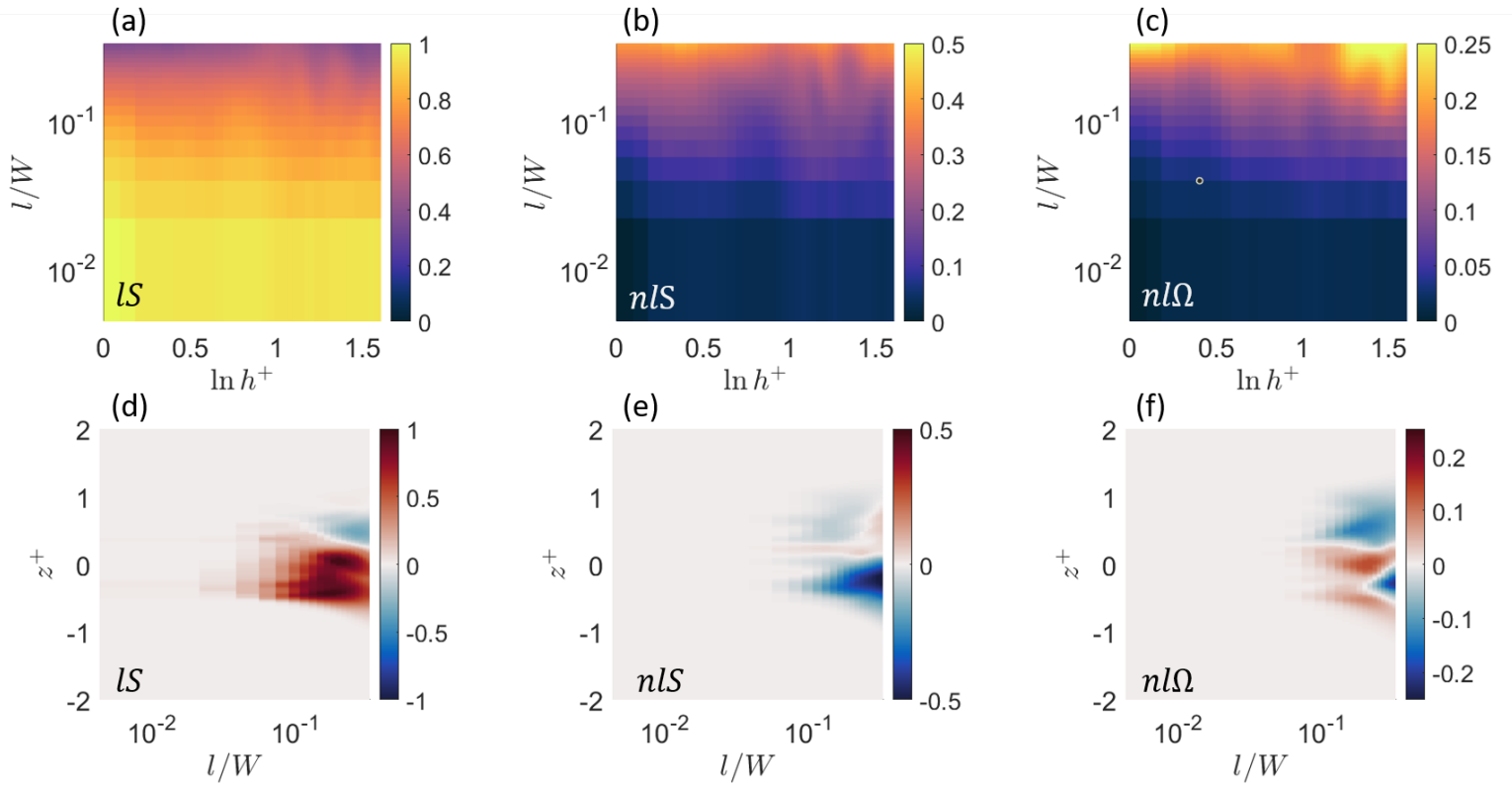

Figure 46: Filter based scale-to-scale transport mechanisms from HSS data

Chapter 5

Conclusions

The present work consists of three experimental campaigns, one set of single-shot simultaneous PLIF and PIV measurements, one set of high-speed PLIF measurements and a set of high-speed simultaneous PLIF-PIV experiments.

The single-shot experiments required a large set of runs to reach statistical convergence of results, so 20 individual experiments were used for each of the post-reshock times considered.

The high-speed experiments allowed the time evolution from a given initial condition to be traced, so the effect of the initial condition could potentially be explored.

High-speed simultaneous PLIF-PIV experiments provided time resolved measurements of the concentration and velocity fields that enabled the direct calculation of terms that were previously unable to be assessed.

To allow for the higher temperatures and pressures seen at reshock conditions an iterative PLIF correction algorithm, developed by Herzog *et al*. [13], was implemented.

The high-speed experiment campaigns were enabled by the engineering of a pulse-burst laser system by Professor Rothamer. Its capabilities enabled the time evolution of the mixing layer to be analysed as opposed to needing to acquire large numbers of individual experiments to determine a statistical depiction of the evolution.

This access to the time evolution of the system lead to an impulse to ask what coordinate system can be constructed to give the most natural comparison between experiments. Others had used $\ln h^+$, the number of generations, as a measure of time, though had not seemingly

derived why it was reasonable to do so, only that it offered collapse of data. Here, the number of generations has been shown to appear as a natural measure of time from the transport equations if time dependent normalization values are used.

Introduced next were the transport equations for three different methods of analyzing scale-to-scale energy transport, with a focus on the "homogeneous" direction transport terms, and on the terms now available due to measurement of both velocity and concentration fields.

Some of the main results found were:

- The vorticity deposition model, developed by Weber[54] and further developed here, shows a stronger predictive ability than the simple reshock model of Mikaelian.

- Mixed normalised spanwise moments of the streamwise velocity and scalar fields were shown to have time-invariant functional forms that were matched by post-shock and post-reshock *Miranda* simulation results.

- Scalar power spectra show small regions close to inertial range scaling and larger regions of $-\frac{11}{3}$ scaling that may be indicative of an inertial-diffusive range.

- The slope of the scalar power spectra ζ_ξ seems to follow the functional form as given by Gibson [11] as a function of Schmidt number. The Schmidt number here though is the effective rather than material Schmidt number, emphasising that the flow is not in the homogeneous isotropic state.

- Concurrent scalar and velocity data allowed direct measurement of terms (all except pressure related terms) in the spectral transport equation for the kinetic energy power spectrum, as well as all the terms in the scalar power spectrum transport equation. RS2 and RS3 showed similar structure for the terms in the scalar spectrum transport terms

leading to the identification of a cartoon of the terms in the quasi-stationary regime in self-similar coordinates.

- Initial condition effects on the evolution of structure functions and their exponents suggest that their is a trend toward Kraichnan, and therefore turbulent scaling, and that ICs that begin with larger bandwidths and access to more scales will access this state faster. There isn't a guarantee that ICs with smaller bandwidths will reach these scalings though they do appear to tend toward them.

- The second order structure function transport terms represent a similar story to their corresponding Fourier analysis terms, except for the homogeneous transport term, which is dominated by forward transport over a much larger range of vertical location. This however matches with the structure observed in the filter based scale-to-scale transport term.

Bibliography

[1] M. H. Anderson, B. P. Puranik, J. G. Oakley, P. W. Brooks, and R. Bonazza. Shock tube investigation of hydrodynamic issues related to inertial confinement fusion. *Shock Waves*, 10(5):377–387, 2000.

[2] G. K. Batchelor, I. D. Howells, and A. A. Townsend. Small-scale variation of convected quantities like temperature in turbulent fluid part 2. the case of large conductivity. *Journal of Fluid Mechanics*, 5(1):134–139, 1959.

[3] John Carter, Gokul Pathikonda, Naibo Jiang, Josef J. Felver, Sukesh Roy, and Devesh Ranjan. Time-resolved measurements of turbulent mixing in shock-driven variable-density flows. *Scientific Reports*, 9(1):20315, 2019.

[4] KWING-SO CHOI and JOHN L. LUMLEY. The return to isotropy of homogeneous turbulence. *Journal of Fluid Mechanics*, 436:59–84, 2001.

[5] B. D. Collins and J. W. Jacobs. PLIF flow visualization and measurements of the Richtmyer-Meshkov instability of an air/SF6 interface. *Journal of Fluid Mechanics*, 464, 2002.

[6] Andrew W. Cook and Ye Zhou. Energy transfer in Rayleigh-Taylor instability. *Physical Review E*, 66(2), 2002.

[7] Paul E. Dimotakis. The mixing transition in turbulent flows. *Journal of Fluid Mechanics*, 409:69–98, 2000.

[8] G. S. Elliott and M. Samimy. Compressibility effects in free shear layers. *Physics of Fluids A: Fluid Dynamics*, 2(7):1231–1240, 1990.

[9] U Frisch and A Wirth. Inertial-diffusive range for a passive scalar advected by a white-in-time velocity field. *Europhysics Letters (EPL)*, 35(9):683–688, sep 1996.

[10] Michael Gauding, Achim Wick, Heinz Pitsch, and Norbert Peters. Generalised scale-by-scale energy-budget equations and large-eddy simulations of anisotropic scalar turbulence at various schmidt numbers. *Journal of Turbulence*, 15(12):857–882, 2014.

[11] Carl H. Gibson. Fine structure of scalar fields mixed by turbulence. II. spectral theory. *The Physics of Fluids*, 11(11):2316–2327, 1968.

[12] David G. Goodwin, Harry K. Moffat, Ingmar Schoegl, Raymond L. Speth, and Bryan W. Weber. Cantera: An object-oriented software toolkit for chemical kinetics, thermodynamics, and transport processes. `https://www.cantera.org`, 2022. Version 2.6.0.

[13] J. M. Herzog, A. Ames, C. Noble, J. Oakley, R. Bonazza, and D. A. Rothamer. Iterative correction of shocked acetone high-speed PLIF measurements in the Richtmyer-Meshkov instability. *Proceedings of the 32nd International Symposium on Shock Waves*, 32:In Press, 2019.

[14] Reginald J. Hill. Exact second-order structure-function relationships. *Journal of Fluid Mechanics*, 468:317–326, 2002.

[15] Perry L. Johnson. Energy transfer from large to small scales in turbulence by multiscale nonlinear strain and vorticity interactions. *Physical Review Letters*, 124(10):104501, 2020.

[16] M. A. Jones and J. W. Jacobs. A membraneless experiment for the study of Richtmyer-Meshkov instability of a shock-accelerated gas interface. *Physics of Fluids*, 9(10):3078–3085, 1997.

[17] Jon D. Koch, Joachim Gronki, and Ronald K. Hanson. Measurements of near-UV absorption spectra of acetone and 3-pentanone at high temperatures. *Journal of Quantitative Spectroscopy and Radiative Transfer*, 109(11):2037–2044, 2008.

[18] Robert H. Kraichnan. Anomalous scaling of a randomly advected passive scalar. *Phys. Rev. Lett.*, 72:1016–1019, 1994.

[19] V V Krivets, K J Ferguson, and J W Jacobs. Turbulent mixing induced by Richtmyer-Meshkov instability. *AIP Conference Proceedings*, 1793, 2017.

[20] John D. Lindl, Peter Amendt, Richard L. Berger, S. Gail Glendinning, Siegfried H. Glenzer, Steven W. Haan, Robert L. Kauffman, Otto L. Landen, and Laurence J. Suter. The physics basis for ignition using indirect-drive targets on the National Ignition Facility. *Physics of Plasmas*, 11(2):339–491, 2004.

[21] Frank E Marble, Gavin J Hendricks, and Edward E Zukoski. Progress Toward Shock Enhancement of Supersonic Combustion Processes. *Turbulent Reactive Flows*, 40:26, 1989.

[22] Jacob A. McFarland, Jeffrey A. Greenough, and Devesh Ranjan. Computational parametric study of a Richtmyer-Meshkov instability for an inclined interface. *Physical Review E*, 84(2):026303, 2011.

[23] Marco Mehl, William J. Pitz, Charles K. Westbrook, and Henry J. Curran. Kinetic modeling of gasoline surrogate components and mixtures under engine conditions. *Proceedings of the Combustion Institute*, 33(1):193 – 200, 2011.

[24] E. E. Meshkov. Instability of the interface of two gases accelerated by a shock wave. *Fluid Dynamics*, 4(5):101–104, 1972.

[25] Mohammad Mohaghar, John Carter, Benjamin Musci, David Reilly, Jacob McFarland, and Devesh Ranjan. Evaluation of turbulent mixing transition in a shock-driven variable-density flow. *Journal of Fluid Mechanics*, 831:779–825, 2017.

[26] Mohammad Mohaghar, John Carter, Gokul Pathikonda, and Devesh Ranjan. The transition to turbulence in shock-driven mixing: effects of Mach number and initial conditions. *Journal of Fluid Mechanics*, 871:595–635, 2019.

[27] B. E. Morgan, B. J. Olson, J. E. White, and J. A. McFarland. Self-similarity of a Rayleigh-Taylor mixing layer at low Atwood number with a multimode initial perturbation. *Journal of Turbulence*, 18(10):973–999, 2017.

[28] Christopher D. Noble, Josh M. Herzog, Alex M. Ames, Jason Oakley, David A. Rothamer, and Riccardo Bonazza. High speed PLIF study of the Richtmyer-Meshkov instability upon re-shock. *Physica D: Nonlinear Systems*, 2020.

[29] Christopher D. Noble, Josh M. Herzog, Alex M. Ames, Jason Oakley, David A. Rothamer, and Riccardo Bonazza. Scalar power spectra and scalar structure function evolution in the Richtmyer-Meshkov instability upon re-shock. *ASME Journal of Fluid Engineering*, 2020.

[30] J. G. Oakley, B.P. Puranik, M.H. Anderson, R.R. Peterson, R. Bonazza, R.P.Weaver, and M.L.Gittings. An investigation of shock-cylinder interaction. *The 22nd International Symposium on Shock Waves*, London UK 1999.

[31] G. C. Orlicz, B. J. Balakumar, C. D. Tomkins, and K. P. Prestridge. A Mach number study of the Richtmyer-Meshkov instability in a varicose, heavy-gas curtain. *Physics of Fluids*, 21(6):064102, 2009.

[32] Samuel Petter, Benjamin Musci, Gokul Pathikonda, and Devesh Ranjan. Simultaneous Measurements of velocity and density in the Blast-Driven Instability. In *APS Division of Fluid Dynamics Meeting Abstracts*, APS Meeting Abstracts, page E05.009, January 2020.

[33] K. Prestridge, P. M. Rightley, P. Vorobieff, R. F. Benjamin, and N. A. Kurnit. Simultaneous density-field visualization and PIV of a shock-accelerated gas curtain. *Experiments in Fluids*, 29(4):339–346, 2000.

[34] Rayleigh. Investigation of the Character of the Equilibrium of an Incompressible Heavy Fluid of Variable Density*. *Proceedings of the London Mathematical Society*, s1-14(1):170–177, 11 1882.

[35] Daniel Reese. *Direct Measurements of Concentration and Velocity in the Richtmyer-Meshkov Instability*. PhD thesis, University of Wisconsin - Madison, Madison, WI, 2017.

[36] Daniel Reese, Jason Oakley, Alonso Navarro-Nunez, David Rothamer, Chris Weber, and Riccardo Bonazza. Simultaneous concentration and velocity field measurements in a shock-accelerated mixing layer. *Experiments in Fluids*, 55(10):1823, 2014.

[37] Daniel T. Reese, Alex M. Ames, Chris D. Noble, Jason G. Oakley, David A. Rothamer, and Riccardo Bonazza. Simultaneous direct measurements of concentration and velocity in the Richtmyer–Meshkov instability. *Journal of Fluid Mechanics*, 849:541–575, 2018.

[38] R. D. Richtmyer. Taylor instability in shock acceleration of compressible fluids. *Comm. on Pure and App. Math.*, 13:297–319, 1960.

[39] Robert D. Richtmyer. Taylor instability in shock acceleration of compressible fluids. *Communications on Pure and Applied Mathematics*, 13(2):297–319, May 1960.

[40] J. R. Ristorcelli and T. T. Clark. Rayleigh-Taylor turbulence: self-similar analysis and direct numerical simulations. *Journal of Fluid Mechanics*, 507:213–253, 2004.

[41] Sven Scharnowski and Christian J. Kähler. Particle image velocimetry - classical operating rules from today's perspective. *Optics and Lasers in Engineering*, 135:106185, 2020.

[42] Oleg Schilling and Marco Latini. High-order WENO simulations of three-dimensional reshocked Richtmyer-Meshkov instability to late times: dynamics, dependence on initial conditions, and comparisons to experimental data. *Acta Mathematica Scientia*, 30(2):595–620, 2010.

[43] Oleg Schilling, Marco Latini, and Wai Sun Don. Physics of reshock and mixing in single-mode Richtmyer-Meshkov instability. *Physical Review E*, 76(2), 2007.

[44] T. P. Schopflocher and P. J. Sullivan. The Relationship between Skewness and Kurtosis of A Diffusing Scalar. *Boundary-Layer Meteorology*, 115(3):341–358, 2005.

[45] William Thielicke and René Sonntag. Particle image velocimetry for MATLAB: Accuracy and enhanced algorithms in PIVlab. *Journal of Open Research Software*, 9(1):12, 2021. Number: 1 Publisher: Ubiquity Press.

[46] Ben Thornber and Ye Zhou. Energy transfer in the Richtmyer-Meshkov instability. *Physical Review E*, 86(5), November 2012.

[47] Mark C. Thurber, Frédéric Grisch, Brian J. Kirby, Martin Votsmeier, and Ronald K. Hanson. Measurements and modeling of acetone laser-induced fluorescence with implications for temperature-imaging diagnostics. *Appl. Opt.*, 37(21):4963–4978, 1998.

[48] C. D. Tomkins, B. J. Balakumar, G. Orlicz, K. P. Prestridge, and J. R. Ristorcelli. Evolution of the density self-correlation in developing Richtmyer-Meshkov turbulence. *Journal of Fluid Mechanics*, 735:288–306, 2013.

[49] V. K. Tritschler, B. J. Olson, S. K. Lele, S. Hickel, X. Y. Hu, and N. A. Adams. On the Richtmyer-Meshkov instability evolving from a deterministic multimode planar interface. *Journal of Fluid Mechanics*, 755:429–462, 2014.

[50] S. Ukai, K. Balakrishnan, and S. Menon. Growth rate predictions of single- and multi-mode Richtmyer-Meshkov instability with reshock. *Shock Waves*, 21(6):533–546, 2011.

[51] M. Vetter and B. Sturtevant. Experiments on the Richtmyer-Meshkov instability of an air/SF6 interface. *Shock Waves*, 4(5):247–252, March 1995.

[52] P. Vorobieff, N.-G. Mohamed, C. Tomkins, C. Goodenough, M. Marr-Lyon, and R. F. Benjamin. Scaling evolution in shock-induced transition to turbulence. *Phys. Rev. E*, 68:065301, 2003.

[53] Peter Vorobieff, Paul M. Rightley, and Robert F. Benjamin. Power-law spectra of incipient gas-curtain turbulence. *Phys. Rev. Lett.*, 81:2240–2243, 1998.

[54] Christopher R. Weber. *Experimental investigation of the turbulent mixing transition in the Richtmyer-Meshkov instability*. PhD thesis, University of Wisconsin - Madison, Madison, WI, 2012.

[55] Christopher R. Weber, Andrew W. Cook, and Riccardo Bonazza. Growth rate of a shocked mixing layer with known initial perturbations. *Journal of Fluid Mechanics*, 725:372–401, 2013.

[56] Christopher R. Weber, Nicholas Haehn, Jason Oakley, David Rothamer, and Riccardo Bonazza. Turbulent mixing measurements in the Richtmyer-Meshkov instability. *Physics of Fluids*, 24(7):074105, 2012.

[57] Christopher R. Weber, Nicholas S. Haehn, Jason G. Oakley, David A. Rothamer, and Riccardo Bonazza. An experimental investigation of the turbulent mixing transition in the Richtmyer-Meshkov instability. *Journal of Fluid Mechanics*, 748:457–487, 2014.

[58] Christopher R. Weber, Bradley Motl, Jason Oakley, Mark Anderson, and Riccardo Bonazza. Richtmyer-Meshkov Parameter Study. *Fusion Science and Technology*, 56(1):460–464, 2009.

[59] Man Long Wong, Jon R. Baltzer, Daniel Livescu, and Sanjiva K. Lele. Analysis of second moments and their budgets for richtmyer-meshkov instability and variable-density turbulence induced by reshock. *Phys. Rev. Fluids*, 7:044602, Apr 2022.

[60] Ye Zhou. Rayleigh-Taylor and Richtmyer-Meshkov instability induced flow, turbulence, and mixing. I. *Physics Reports*, 720-722:1–136, 2017.

[61] Ye Zhou. Rayleigh-Taylor and Richtmyer-Meshkov instability induced flow, turbulence, and mixing. II. *Physics Reports*, 723-725:1–160, 2017.